Department of Geomatics Engineering

Augmentation of GPS with a Barometer and a Heading Rate Gyroscope for Urban Vehicular Navigation

(URL: http://www.geomatics.ucalgary.ca/links/GradTheses.html)

by

Nobuyuki Hayashi

December 1996

UNIVERSITY OF
CALGARY

THE UNIVERSITY OF CALGARY

Augmentation of GPS with a Barometer and a Heading Rate Gyroscope

for Urban Vehicular Navigation

by

Nobuyuki Hayashi

A THESIS

SUBMITTED TO THE FACULTY OF GRADUATE STUDIES

IN PARTIAL FULFILMENT OF THE REQUIREMENTS FOR THE

DEGREE OF MASTER OF SCIENCE

DEPARTMENT OF GEOMATICS ENGINEERING

CALGARY, ALBERTA

DECEMBER, 1996

PREFACE

This is an unaltered version of the author's Master of Science in Engineering Thesis of the same title. This thesis was accepted by the Faculty of Graduate Studies in December 1996.

The faculty supervisor for this work was Dr. Gérard Lachapelle and the other members of the examining committee were Dr. M. E. Cannon, Dr. M. J. Collins, Dr. M. Fattouche and Dr. G. Rogers.

ABSTRACT

A new integrated DGPS / sensors land navigation system is introduced and examined. It incorporates barometric height and gyro heading which act as vertical and horizontal vehicle trajectory constraints to enhance position accuracy and availability in urban and forested environments where satellite signals are frequently blocked by obstructions. The concept of sensor constraint GPS navigation is briefly discussed. Decentralized two-state Kalman filters are implemented to obtain smooth sensor information and to estimate corrections. Error models for sensor input are developed to evaluate the effect of corresponding constraints. Augmented least squares and Kalman position estimators are chosen for constrained position determination. Field tests were carried out and height and heading constraint DGPS solutions are compared with unaided DGPS and barometric height aided DGPS solutions. For the cases tested, it improves the positioning availability by 24 to 35% while mostly maintaining the positioning accuracy within 10 metres DRMS. Conclusions are presented and advantages and disadvantages of this concept are discussed.

ACKNOWLEDGEMENTS

DEDICATION

I dedicate this thesis to my parents, Yoshinori and Keiko

and

whatever brought me here.

TABLE OF CONTENTS

LIST OF TABLES

LIST OF FIGURES

NOTATION

Symbols:

A	amplitude of signal (chapter one)
$\mathbf{A}$	design matrix (chapter four)
c	speed of light in a vacuum
$\mathbf{C}_l$	covariance matrix of measurements
$c\delta t$	receiver clock offset error
$c\delta \dot{t}$	receiver clock drift error
d_{CT}	cross-track distance to virtual wall
d_i^L	distance measured at time t_i by left wheel odometer
d_i^R	distance measured at time t_i by right wheel odometer
d_{ion}	ionospheric delay
d_{trop}	tropospheric delay
$d\rho$	orbital error
dt	satellite clock error
dT	receiver clock error
$d\phi$	distance between two epochs in latitude
$d\lambda$	distance between two epochs in longitude
h	height
h_b	barometric height measurement
$\mathbf{H}_k$	design matrix which gives noiseless connection between the measurement and state vector at t_k
k	adaptation gain constant
$\mathbf{K}_k$	Kalman filter gain at t_k
$\mathbf{l}$	observation vector
p	range measurement
$p(t)$	PRN code (either +1 or -1)

$\hat{P}_k$	smoothed range measurement at t_k
$\mathbf{P}_k$	error covariance matrix associated with optimal estimate at t_k
$\mathbf{P}_k^-$	error covariance matrix associated with projected estimate at t_k
q	spectral density
q_{cdt}	spectral density of receiver clock offset error
q_{cdt}	spectral density of receiver clock drift error
q_h	spectral density of height position error
$q_{\dot{h}}$	spectral density of height rate error
q_λ	spectral density of longitude position error
$q_{\dot{\lambda}}$	spectral density of longitude rate error
q_ϕ	spectral density of latitude position error
$q_{\dot{\phi}}$	spectral density of latitude rate error
Q	process noise covariance
$\hat{Q}$	adapted process noise covariance
$\mathbf{Q}_k$	variance of process noise
$\mathbf{r}$	position vector of a satellite
$\mathbf{R}$	position vector of a land vehicle
R_L	radius of the left wheel's curvilinear path
R_R	radius of the right wheel's curvilinear path
$\mathbf{R}_k$	variance of measurement error at t_k
v	velocity
$\mathbf{v}_k$	measurement error assumed to be white with a known covariance structure
W	weight
$\mathbf{w}^0$	misclosure vector
$\mathbf{w}_k$	white noise with known covariance structure

$\mathbf{w}(t)$	random forcing function
$w_{cdt}(t)$	white noise input of receiver clock offset error
$w_{cdt}(t)$	white noise input of receiver clock drift error
$w_h(t)$	white noise input of height position error
$w_{\dot{h}}(t)$	white noise input of height rate error
$w_\lambda(t)$	white noise input of longitude position error
$w_{\dot{\lambda}}(t)$	white noise input of longitude rate error
$w_\phi(t)$	white noise input of latitude position error
$w_{\dot{\phi}}(t)$	white noise input of latitude rate error
$\hat{\mathbf{x}}$	solution vector
$\mathbf{x}^0$	a priori position estimate vector
$\mathbf{x}_{k+1}$	process state vector at time t_{k+1}
$\hat{\mathbf{x}}_k$	updated estimate at t_k
$\hat{\mathbf{x}}_k^-$	projected estimate at t_k
$\mathbf{x}(t)$	system state vector
$\mathbf{z}_k$	measurement vector at t_k
α_{CT}	cross-track cutoff angle
α_i	azimuth heading of vehicle's forward direction at epoch t_i
α_k	cutoff angle of a satellite
β	time constant for the process
β_{cdt}	time correlation constant of receiver clock offset estimate
β_h	time correlation constant of height estimate
β_k	azimuth of a satellite (chapter seven)
β_λ	time correlation constant of longitude estimate
β_ϕ	time correlation constant of latitude estimate
γ_k	relative azimuth of a satellite with respect to the vehicle's heading

δ	least squares adjustments to parameters
$\delta(t)$	Dirac delta function
δh	height position error
$\delta \dot{h}$	height rate error
$\delta \lambda$	longitude position error
$\delta \dot{\lambda}$	longitude rate error
$\delta \phi$	latitude position error
$\delta \dot{\phi}$	latitude rate error
Δd	mean distance traveled over a data interval
ΔL	path length difference
$\Delta \phi$	phase difference
$\varepsilon_b(t_{k+1})$	barometric height error at time t_{k+1}
ε_b	barometric height offset (residual) error
$\dot{\varepsilon}_b$	linear barometric height drift rate
$\varepsilon_{CT}(t_{k+1})$	cross-track position error at t_{k+1}
$\varepsilon_g(t_{k+1})$	gyro error at t_{k+1}
ε_g	gyro heading rate offset (residual) error
$\dot{\varepsilon}_g$	gyro drift error
ε_{GPS}	GPS cross-track position estimate error
ε_p	receiver noise
$\varepsilon_\Theta(t_{k+1})$	heading error at t_{k+1}
ε_Θ	initial heading error
θ_m	relative multipath phase
Θ	vehicle heading
λ	wavelength
λ_k	longitude position at t_k

π	ratio of circumference of circle to its diameter
ρ	geometric range
ϕ_k	latitude position at t_k (chapter six)
ϕ_k	matrix relating $\mathbf{x}_k$ and $\mathbf{x}_{k+1}$ in absence of a forcing function (chapter five)
Φ	rotation
Φ_k	carrier phase measurement
σ^2	variance
σ_b^2	barometric height error variance
σ_g^2	gyro heading rate error variance
σ_p^2	GPS range error variance
σ_Θ^2	gyro heading error variance
$\sigma_{\delta dt}^2$	satellite clock error variance
$\sigma_{\delta iono}^2$	ionospheric delay variance
$\sigma_{\delta trop}^2$	tropospheric delay variance
$\sigma_{\delta \rho}^2$	orbital error variance
σ_ε^2	measurement noise variance
ω	gyroscope heading change
ω_0	carrier frequency plus Doppler shift
Ω	angular velocity

Operators:

$\mathbf{A}^\mathrm{T}$	matrix transpose
$\mathbf{A}^{-1}$	matrix inverse
$|\mathbf{a}|$	length of the vector $\mathbf{a}$
$|\mathbf{a} \bullet \mathbf{b}|$	dot product of vectors $\mathbf{a}$ and $\mathbf{b}$

$\lvert \mathbf{a} \times \mathbf{b} \rvert$	cross product of vectors **a** and **b**
$\dfrac{df}{dx}$	partial derivative of the function f with respect to x

Acronyms:

2D	two dimensional space
3D	three dimensional space
AS	Anti-Spoofing
AVL	Automatic Vehicle Location
C/A code	Coarse/Acquisition code (1.023 MHz)
DOD	US Department of Defense
DGPS	Differential GPS
DR	Dead Reckoning
DRMS	Distance Root Mean Square
ECEF	Earth-Centre Earth-Fixed
EDOP	East Dilution of Precision
FOG	Fiber Optic Gyro
FM	Frequency Modulation
GDOP	Geometric Dilution Of Precision
GPS	Global Positioning System
HDOP	Horizontal Dilution Of Precision
IVHS	Intelligent Vehicle Highway System
L1	L1 carrier (1575.42 MHz)
L2	L2 carrier (1227.6 MHz)
MS-DOS	Microsoft Disk Operating System
MSPE	Mean Square Positional Error
NAVSTAR	Navigation Satellite Timing and Ranging
NDOP	North Dilution of Precision
OEM	Original Equipment Manufacturer

P code	Precision code (10.23 MHz)
PC	Personal Computer
PCMCIA	Personal Computer Memory Card International Association
PDOP	Positional Dilution Of Precision
PRN	Pseudo Random Noise
RAM	Random Access Memory
RLG	Ring Laser Gyro
RMS	Root Mean Square
RTK	Real-Time Kinematic
SA	Selective Availability
SV	Space Vehicle
TDOP	Time Dilution Of Precision
UHF	Ultra High Frequency
VDOP	Vertical Dilution Of Precision
WGS 84	World Geodetic System of 1984
Y code	Encrypted P code

CHAPTER ONE

INTRODUCTION

The field of land vehicle navigation is growing rapidly with the maturation of the Global Positioning System (GPS) and the advancement of positioning-related technologies in recent years. GPS is a satellite based radionavigation system developed by the U.S. Department of Defense (Spilker 1980). It includes a constellation of 24 satellites in six orbital planes, which are strategically arranged so that a minimum of six satellites are visible to users anywhere in the world at all times. The satellite altitude is approximately 19,652 km (Spilker 1980). One requirement of GPS positioning is that one must be able to observe these multiple satellite signals simultaneously without mutual interference. The GPS receiver uses a set of at least four satellite range measurements to calculate a receiver position with respect to a earth-centre earth-fixed (ECEF) coordinate system. The 1.6GHz GPS signals are essentially line-of-sight.

Vehicle navigation and tracking is a topic of great interest today due to the large potential market for both consumer and business vehicles. All of the major automobile manufacturers have been developing in-vehicle navigation systems. They guide travelers and motorists to desired destinations, help them find correct roads and highways and give them various data such as current location, distance to the destination and estimated arrival time. Recent Japanese car navigation units are capable of receiving traffic information via FM wave or beacons and they can suggest the "least clogged" route in the real-time. Some have bi-directional communication functions to send back the location of

a vehicle to a control station for advanced traffic controls (Sakata 1996). Another extensive market is the tracking of commercial vehicles. In the United States alone, the total number of commercial vehicles exceeds 17 million (Brown 1992). Low cost electronics are already permitting the introduction of navigation systems into emergency vehicles (fire engines, polices cars, ambulances) and into truck fleets. Other vehicle tracking applications include delivery and courier services, armored car services, utility companies, private security companies, stolen cars, high value goods delivery, automobile towing service, dispatching taxi cabs, shuttle vans and so on (Brown 1992).

1.1 Statement of Problem

The major problem of GPS land navigation is insufficient satellite signal observations in heavily populated and forested areas due to shadowing (signal blockage). Shadowing occurs when tall buildings, bridges, overpasses, highways, tunnels and trees cover the sky partially or entirely. Since the minimum signal strength of L1 C/A code is defined as -160 dBW, GPS signals are not strong enough to penetrate these structures (Spilker 1980). Because GPS positioning requires at least four satellite signals to compute a 3D position estimate and a receiver clock offset relative to GPS time, these obstructions severely reduce the position availability in such areas. Lachapelle et al. (1994) also suggest limited performance of GPS under tree branches and leaves where GPS UHF signals are largely attenuated. In such environments, GPS coverage is no longer optimal and one may frequently encounter a GPS position outage period. Studies have shown that in inner city downtown locations with buildings greater than ten stories, four satellites will be visible

less than 50% of the time, which is far from acceptable coverage for land navigation applications (Sushko 1993).

Another outstanding problem in urban and forested areas is the presence of an unpredictable error called multipath. Multipath is defined as the error caused by the reflection, refraction, or bouncing of the signal on its way to the receiver, resulting in the same signal arriving at the receiver by more than one path (Navtech Seminars Inc. 1996). Multipath provides a false position estimate to the user. Braasch (1996) gives the mathematical model of a multipath-contaminated GPS signal (direct signal plus multipath rays) as

$$
\begin{aligned}
s(t) &= -Ap(t)\sin(\omega_0 t) - \alpha_1 Ap(t+\delta_1)\sin(\omega_0 t+\theta_{m1}) - \cdots - \alpha_n Ap(t+\delta_n)\sin(\omega_0 t+\theta_{mn}) \\
&= -Ap(t)\sin(\omega_0 t) - \sum_{i=1}^{n}\alpha_i Ap(t+\delta_i)\sin(\omega_0 t+\theta_{mi})
\end{aligned}
$$

(1.1)

where

A	amplitude of direct signal [W],
$p(t)$	PRN code (either +1 or -1),
ω_0	carrier frequency plus Doppler shift [Hz],
α_i	amplitude of the ith multipath component relative to the direct path [W],
δ_i	time delay of the ith multipath component relative to the direct path (which must be negative when given sign convention is used) [s],

θ_{mi} — phase of the ith multipath component relative to the direct path [rad],

n — number of multipath signals.

Several attempts have been made to model the signal structure of the multipath to minimize its error (Van Nee & Siereveld 1994). Multipath range error is typically in the order of 0-50 metres depending on the environment, antenna type, receiver type and user dynamics. Multipath errors of over 100 metres have been reported near skyscrapers (Braasch 1996). In urban and forested environment, the multipath may severely degrade the positioning accuracy. With little or no redundancy, a position estimate may become highly vulnerable to contaminated GPS observations.

1.2 Literature Review

It has become common, as inexpensive and reliable positioning sensors are being introduced (Nakamura 1990, Phillips 1993, Allen et al. 1994, Martinelli & Ikeda 1995), to combine GPS with other positioning devices to enhance navigation capability in urban canyons. Most commercial GPS land navigation systems are capable of utilizing distance sensors (e.g. odometer) and heading rate sensors to enable GPS-independent positioning, called dead reckoning (DR), in the absence of sufficient GPS signals. Dead reckoning uses heading and distance sensors to measure the displacement vectors which are then used in a recursive manner to determine the current vehicle position.

Kao (1991) examined the possible combination of GPS and DR systems to obtain superior performance. He suggested the combination of a gyro, magnetic compass and odometer in the DR system. Gyro measurements are used to eliminate the short term magnetic anomalies in compass heading measurements. Geier et al. (1993) took a simpler approach as shown in Figure 1.1. They integrated an odometer and gyro into the Trimble Placer™ GPS/DR system. This DR sensor configuration is used in many DR and GPS/DR systems. The system uses the filtered position solutions which provide a level of multipath rejection.
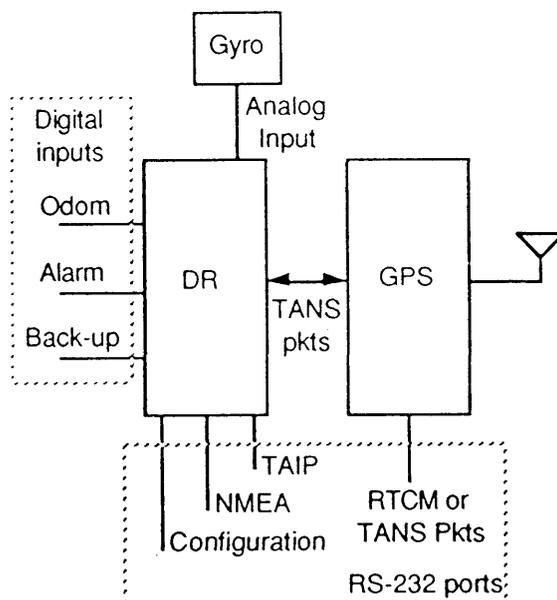
Figure 1.1. Trimble Placer™ GPS/DR System from (Geier et al. 1993)
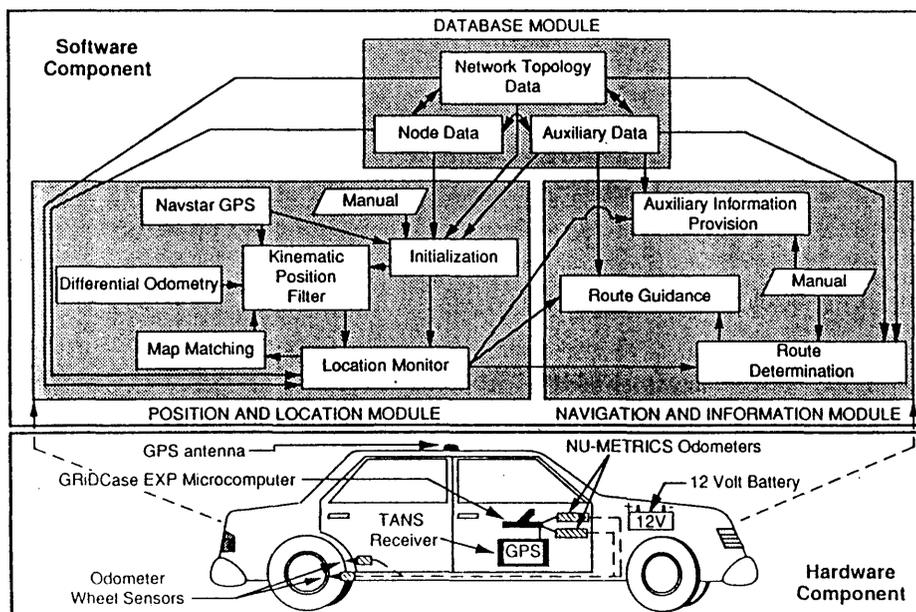
Figure 1.2. Architectural Design of the AVLIN 2000™ Prototype System from (Harris 1989)

Harris (1989) employed the differential odometry theory with a map database module and GPS as seen in Figure1.2. As each odometer only measures distances traveled by one wheel, two are required for differential odometry. This technique eliminates the need for rotation sensors since differential odometry can provide heading change information. Map matching and DR methods are used to update positions when GPS is not available. Ishikawa et al. (1995) utilized map matching technology in addition to a distance sensor, fibre optic gyro and GPS receiver to improve position accuracy. This system employed another technique to obtain a smooth trajectory. When a fibre optic gyro reading is below the threshold value, the vehicle is assumed to be on a straight line. The system then solves a regression line equation to smooth the vehicle trajectory. Bullock
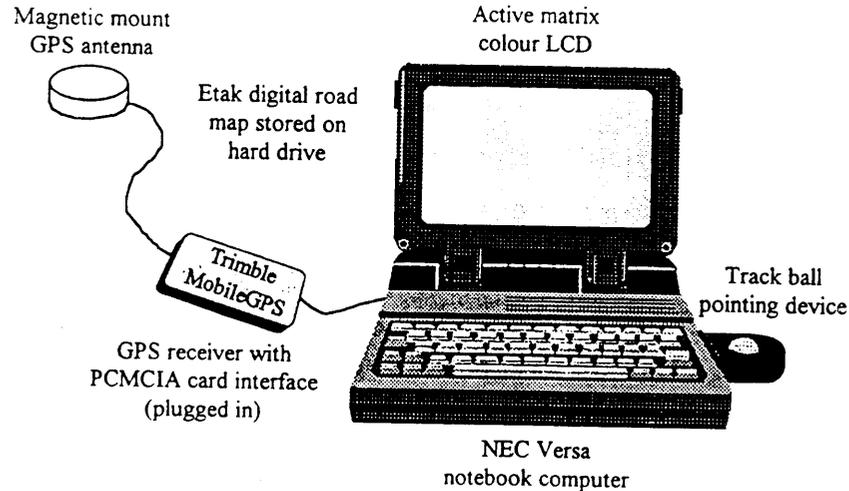
Figure 1.3. PortaNav Map-Aided GPS Navigation System from (Bullock 1995)

(1995) proposed a portable land navigation system which does not require an odometer or gyro as shown in Figure 1.3. He selected the Etak digital road maps and a Trimble MobileGPS, a PCMCIA card-type GPS receiver with six parallel channels and eight track satellites, and created the PortaNav map aided GPS navigation system. The system features an 8-state Kalman position filter, various route finding algorithms and map aiding logic.

1.3 System Requirements

The requirements of the navigation system proposed herein are (1) portability, (2) acceptable accuracy and (3) low cost. Requirement (1) is of primary importance due to the nature of the research project. A dedicated test vehicle would be ideal since certain sensors, such as an odometer, could be installed permanently. A vehicle equipped with anti-lock brakes may have odometer(s) to monitor the rotation of the wheels. However,

such a vehicle still requires the installation of an odometer output reader. Since most testing was done with a rental vehicle, modifying the vehicle was not an option. Requirement (2) depends on the system configuration, particularly that of GPS. Table 1.1 shows the error budgets of single point GPS positioning.

In single point mode, a GPS receiver is subject to errors from the atmosphere, multipath, satellite orbits, satellite clocks and receiver noise (Bullock 1995). However, it is known that the spatial correlation of satellite orbit and clock errors (includes selective availability) and atmospheric errors are reasonably high for short baselines in differential mode. Differential GPS takes advantage of this by placing a GPS monitor station at a control point. Given the accurate coordinate of the control point, the monitor receiver can compute a GPS range error mostly induced by spatially correlated errors. The range error is then sent to the remote GPS receiver as a range correction. This technique reduces the GPS positioning error dramatically, from 100 m to several metres for a code solution.

**Table 1.1. Single Point GPS Error Budgets
from (Lachapelle 1995, Braasch 1996, Bullock 1995)**

Error source	Typical C/A code range error
Tropospheric delay	2 - 30 m
Ionospheric delay	2 - 50 m
Satellite orbit errors	5 - 10 m
Satellite clock errors	10m
Selective availability (SA)	5 - 80 m
Measurement noise	0.1 - 3 m
Multipath	0 -50 m

For land navigation applications, it is desirable that the user be able to determine the location of a vehicle both on the highway and in dense downtown regions. US Department of Transportation defines the minimum accuracy requirement for the automatic vehicle location (AVL) applications as 30m 2DRMS (US Department of Transportation and Defense 1990). For the intelligent vehicle highway system (IVHS), required accuracies are between 1 and 7 metres in urban areas and 10-30 metres in rural areas (Chadwick 1994). For this project, the accuracy requirement is set to 10 m DRMS which is a typical width of a two-lane road. As a consequence, differential GPS mode is chosen to fulfill this requirement. The challenge lies in maintaining positioning accuracy while improving the position availability under the condition that the incoming GPS signal is insufficient and contaminated, satellite geometry is weak or even singular.

Requirement (3) is not important for the research project but absolutely critical for commercial applications. The proposed system is flexible in that the system can accept

input from sensors of diverse quality without redesigning the entire algorithm. All hardware components used in this system may be easily obtained. The current system supports the NovAtel GPSCard™ as the GPS receiver but should work with any GPS receiver which generates GPS time and raw data including pseudorange and carrier phase (for smoothing) observations.

1.4 Objectives

The research project presented in this thesis is primarily aimed at overcoming poor positioning performance in urban areas by introducing constraints on a vehicle's vertical and horizontal trajectory. The author initially tested a barometric height aided GPS system and still encountered poor horizontal geometry in urban areas which resulted in poor horizontal position estimates. The poor performance was caused by the fact that, ironically, height aided GPS navigation was capable of three-satellite positioning and three satellites formed weak geometry more often than four. We desire a widely distributed satellite constellation to ensure that the solution is not weak in any given direction. Consider the satellite constellation projected in the horizontal plane. If satellites are located on a line, the horizontal position accuracy of the direction perpendicular to the solid line shown in Figure 1.4 suffers greatly. This geometric weakness may be manifested as inaccurate position estimates as well as an unexpectedly high Horizontal Dilution of Precision (HDOP).
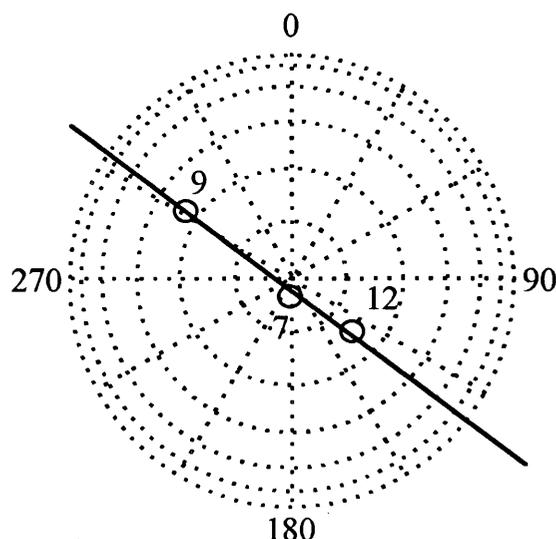
Figure 1.4. Weak Satellite Geometry.
Three GPS Satellites are Aligned As Shown By The Solid Line

In urban environments, weak satellite geometry is frequently observed in terms of the cross-track satellite geometry, a direction perpendicular to the vehicle trajectory. Consider driving a vehicle in a downtown area. There are more obstructions on each side of the vehicle (e.g. multi-storey buildings) than in front of or behind it. These obstructions block incoming GPS signals from the receiver and cause inferior cross-track satellite geometry. The poor satellite geometry, combined with the limited signal availability, increases the dilution of precision (DOP) in the cross-track direction by one to numerous orders of magnitude and causes poor positioning accuracy. Therefore, there is a need to enhance the satellite geometry in order to improve the cross-track position accuracy.

In this project, the author is proposing an inexpensive urban navigation system. Dead reckoning (DR) systems are relatively low cost but require a distance sensor such as an odometer. Since the system for this research had to be portable so that it could be

moved from vehicle to vehicle, a DR system could not be implemented. A new concept had to be developed in order to increase the position availability and accuracy without DR. The concept is called sensor constraint GPS navigation. It employs a barometric pressure transducer (barometer) and a fibre optic gyro (FOG) in addition to a GPS navigation unit. The vertical and horizontal (cross-track) position displacement is constrained according to the sensor information. It is also capable of two-satellite GPS navigation which increases position availability.

As mentioned earlier, solutions in urban and forested environment are more vulnerable to GPS range errors. Providing height and heading constraints implies that the position estimate is also "constrained" against the erroneous signal. Thus, this technology may also be used to reduce multipath error. The arising problem is how to correctly detect the solution containing the multipath error. There are some approaches to detect multipath. Since the vehicle dynamics is limited, we may use this fact as an error threshold. Another idea is to monitor the excessively large GPS range residuals.

We will develop a new land navigation system in the following chapters. Chapter Two describes the overview of the proposed system configuration. In Chapter Three, the current sensor technology is presented and the specifications of the barometer and heading rate gyro, which are employed in the project, are also given. The sensor constraint positioning algorithm is developed in Chapter Four. Various Kalman filters are developed in Chapter Five. In Chapter Six, the navigation software is described. Two field experiments, open sky testing for simulation and downtown Calgary testing, were conducted and results are given in Chapter Seven. The least squares approach is compared

to the Kalman filter approach. Finally, conclusions and recommendations are presented in

Chapter Eight.

CHAPTER TWO

SYSTEM DESIGN

2.1 System Structure

The structure of the sensor constraint GPS navigation system is shown in Figure 2.1. Basic hardware includes a GPS receiver, barometer and heading rate gyro. Data from the GPS, barometer and rate gyro are used in the "augmented" navigation algorithm. Differential GPS was selected to increase the positional accuracy. Thus, another GPS receiver is employed at the monitor station. The system has adopted the modular concept
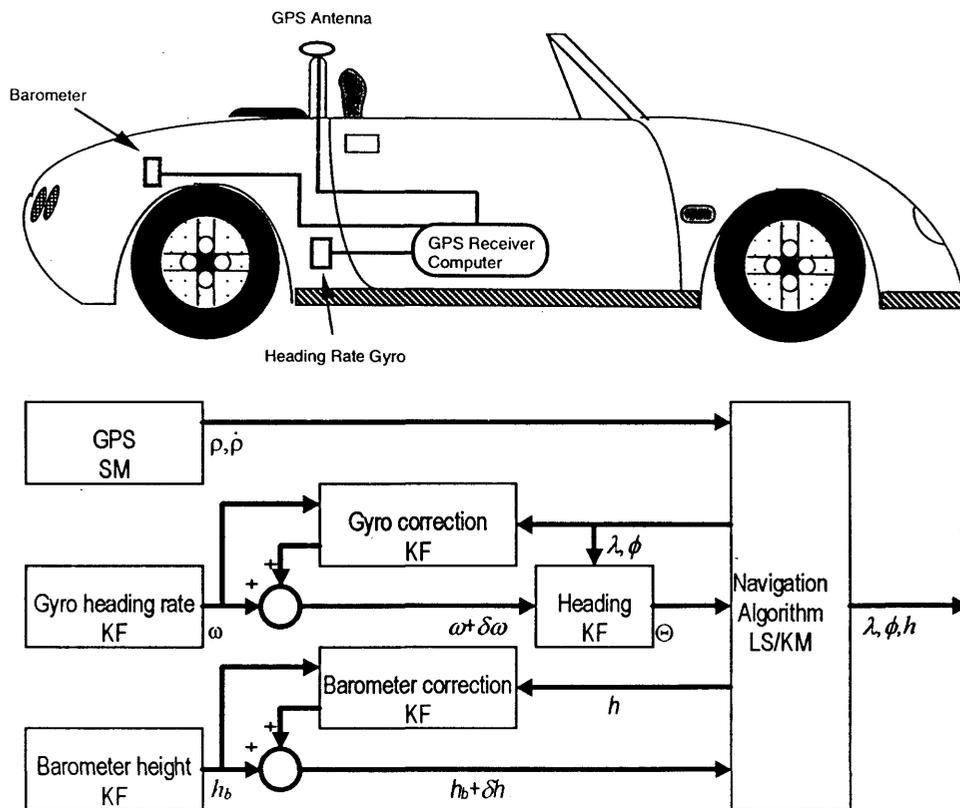
Figure 2.1. System Structure of Sensor Constraint GPS Navigation System. SM = Carrier Phase Range Smoothing Algorithm, KF = Kalman Filter and LS = Least Squares

to maintain flexibility. It operates with GPS alone, GPS and barometer, GPS and gyro or all three sensors.

The system utilizes a decentralized filter approach (Abousalem 1993). This approach is specifically used for multi-sensor systems (Abousalem 1993). The decentralized filtering algorithm is applied to smooth out the raw and noisy sensor measurements and to estimate their errors. This approach has a clear advantage over the conventional centralized filter in terms of the computation time and versatility. A barometric pressure transducer input is transformed into a barometric height, corrected and serves as a sensor height. At each epoch, the gyro sensor input is corrected and converted into a vehicle heading. When the GPS data is insufficient, corrupted or geometrically weak, the sensor height and heading data are utilized to constrain the position estimate. These data are treated as measurements that reduce the number of necessary GPS observations, normally four for a 4D solution, by the number of independent sensor constraints. Thus, the minimum number of GPS observations necessary for a position computation with the sensor height and heading information becomes two. It is possible to further reduce the number of required satellites by adding another sensor information. For instance, an estimated receiver clock offset in addition to the current system could reduce the required GPS observations to one. In addition, an odometer, or distance sensor, could be used for DR positioning during the GPS outage period.

2.2 Hardware Components

The hardware components are designed to be mounted in a vehicle without any

modification. This feature is important because rental cars were used for the project.

Consequently, the system needs to maintain portability. As shown in Figure 2.2, the

hardware system consists of a Viatran Model 246 barometric pressure transducer, an

Andrew AUTOGYRO™ digital fibre optic gyro, a NovAtel GPSCard™ 951R GPS

receiver and antenna, an Advantech PCL-711 12-bit data acquisition board, an IBM-

compatible laptop computer and 12 VDC power supply. Another NovAtel GPSCard™ is
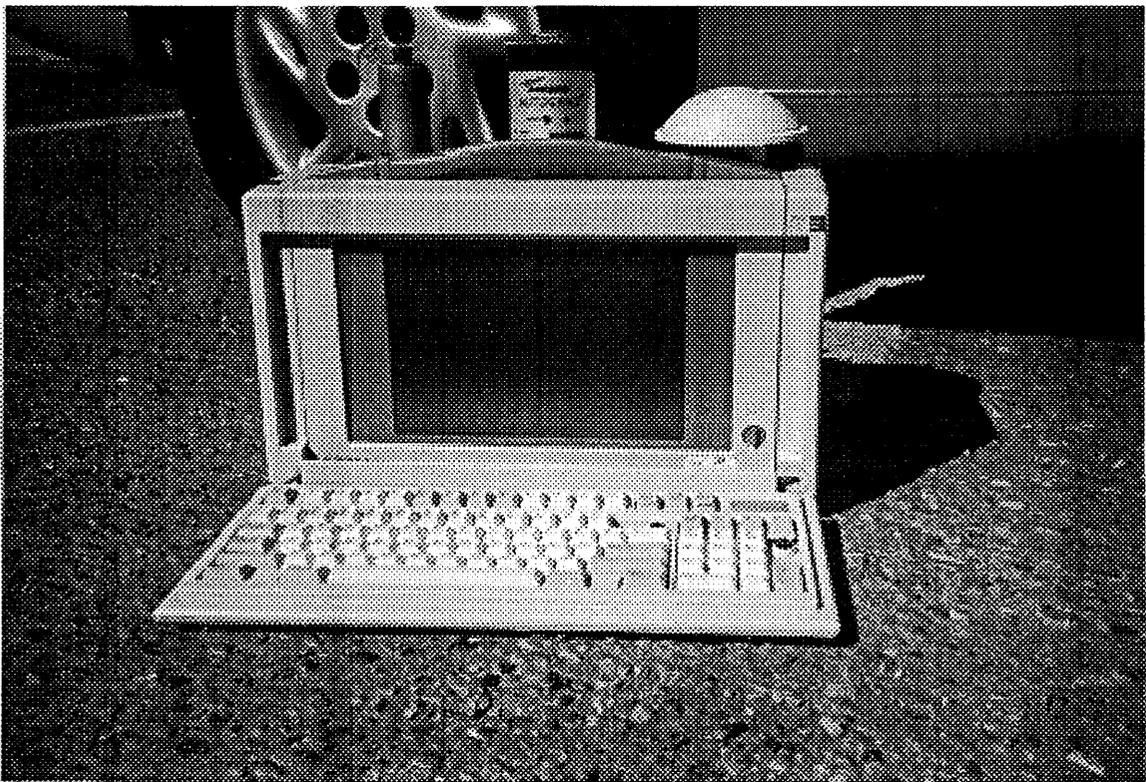
Figure 2.2. Hardware Configuration of Sensor Constraint GPS Navigation System. (From top left to right) Viatran Model246 Barometric Altimeter, Andrew AUTOGYRO™ Fiber Optic Gyro, NovAtel GPS Antenna, (centre) IBM-Compatible Laptop Computer Installed with NovAtel GPSCard™ 951R and Advantech PCL-711 DAC Board

used at the monitor station to generate differential GPS corrections.

The NovAtel GPSCard™ and the Advantech PCL-711 are IDE cards installed in the expansion slots of an IBM-compatible laptop computer. The computer is then placed on the back seat of the test vehicle. It may be necessary to secure the computer on the seat by straps when dynamic maneuvers are expected. A GPS antenna is mounted on the roof to attain maximum signal reception.

The Viatran Model 246 barometer is located on the rear seat as well. It is preferable not to install a barometer in the trunk to minimize the unexpected pressure change due to air flow. This barometer is specifically designed to measure barometric pressure (Viatran 1996). The unit senses an ambient barometric pressure and translates it into an output of voltage ranging from zero to five volts. The voltage output is converted into digital form in order to be processed with the computer. The barometer voltage output is converted into 12-bit digital data by the PCL-711 data acquisition board. A supply voltage between 8.5 and 40 VDC can be used to provide power to the unit. The 12 VDC car battery powers the barometer.

The Andrew AUTOGYRO™ heading rate gyro is located in the centre console as shown in Figure 2.3. A gyro is a device to measure the rotation rate of its axis. An AUTOGYRO™ is a one-axis gyro that measures the heading change of a vehicle. The gyro unit should be mounted on a flat surface in order to avoid a misalignment error. The manufacturer suggests that the mounting surface be parallel to the road surface within approximately 5 degrees (Andrew Corp. 1994). The gyro's minimum detectable angle is approximately 0.005 degrees. The AUTOGYRO ™ continuously generates heading rate

data with an interval of 0.1 seconds. This is a digital fibre optic gyro (FOG) in that it does not require a data acquisition board. The output connector of an AUTOGYRO™ is the DB-9P, also known as the COM port, although its pin layout is not a standard one. A special cable is therefore required to connect the gyro to the computer's communication (COM) port. The AUTOGYRO™ is designed to be operated with a car battery. The 12 VDC car battery is also used to power the gyro.

12 VDC car batteries were needed to power the laptop computer. With a fully-charged generic 50 Ah 12 V DC power supply and a Compaq 386 computer, this system operates for two hours. This was sufficient for this project since its typical operation period was approximately one hour. The operation time may be extended significantly if the vehicle's battery, which is constantly recharged by its alternator, is also used as a power supply.

2.3 System Software

Most land navigation applications require the real-time position determination. Although this system is intended for real-time operation, post processing was selected due to the complexity of obtaining differential GPS corrections in real-time. As a consequence, a data logger and position computation program were needed to operate the system. Real-time implementation, which largely relies on advanced wireless communications, is left for a future project.

New data logging software was written for this project by the author. This program, called ELGO, (1) sends appropriate commands to a GPS receiver and a data

acquisition board to generate specific information at a desired interval, (2) collects GPS data, (3) stores asynchronous gyro data into its buffer in the background, (4) collects barometer and gyro data and stores them with a current GPS time for synchronization during post-processing, and (5) shows current status. Essentially, ELGO operates a GPS receiver, a data acquisition board and a digital gyro simultaneously.

Data intervals of 1, 2, 5 and 10 epochs per second are supported. Barometric data is sampled at 100 Hz and averaged over the data interval period, i.e. one barometer output is an average of 20 raw barometer measurements if operated at 5 epochs per second. Heading rate data from the AUTOGYRO™ is asynchronous. This gyro has its own clock and continuously produces heading rates every 0.1 seconds. ELGO stores these data into a temporary storage space (buffer). When GPS data is obtained, ELGO immediately adds to it all the data in the buffer, adds a GPS time mark extracted from the GPS data, stores the gyro data with GPS time and clears the buffer for the next data. It becomes clear that there is a possibility of missing gyro data due to an inexpensive oscillator in the gyro. The manufacturer specifies the data spacing accuracy to be 0.001 seconds. This could lead to the possibility of missing data every 100 epochs. ELGO monitors the number of data stored in the buffer and corrects the output if possible. If the buffer contains k fewer data than it should, ELGO computes the average heading rate from the remaining data and adds this averaged rate k times to the output. ELGO may be used with GPS only or GPS and other sensor(s). Option strings allow ELGO to disable logging of barometer and / or gyro data.
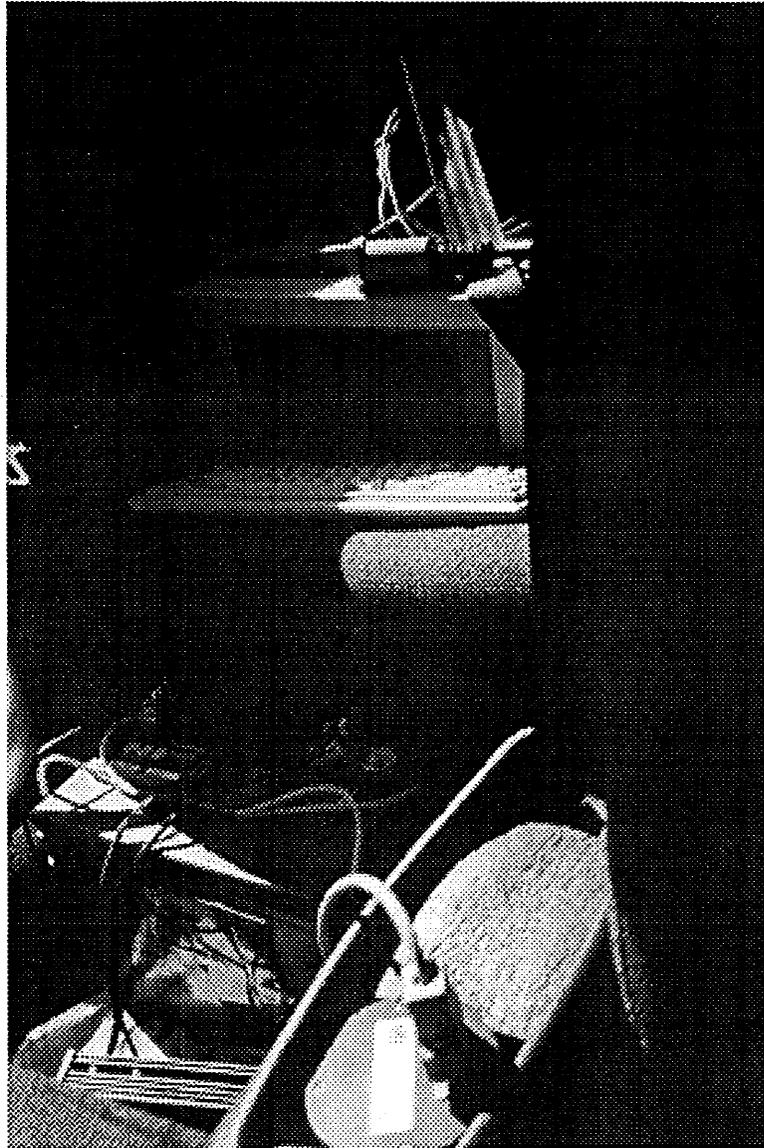
Figure 2.3. Typical Hardware Installation. (Top) Laptop Computer and Barometer in the Rear, (centre) 12 VDC Power Supply and DC-AC Converter and (bottom) AUTOGYRO™ Placed in the Centre Console

The navigation program is based on C^3NAV^{TM}, developed at The University of Calgary (Cannon & Lachapelle 1992). This is a between-receivers, single difference, carrier phase smoothed code DGPS navigation program. It does not solve carrier phase ambiguities and the differential GPS position accuracy is known to be at the metre-level

with NovAtel GPSCards^{TM} in ideal conditions (Cannon & Lachapelle 1992). For this project, this program was extensively modified by the author to accommodate the external sensor information. The modifications include the sensor data interface, the implementation of augmented position estimation routines for sensor constraint positioning and Kalman filters, and the GPS range error detection logic. This program is capable of generating receiver location, satellite location, receiver clock offset, dilution of precision (DOP) and vehicle's heading and velocity. Other features include new position estimation methods (least squares with inequality constraint and the Kalman filter in addition to standard least squares) and sensor constraint positioning (least squares or Kalman filter mode may be selected). Vehicle trajectory may be constrained in terms of heading, height or both.

All programs are written in the C language and compiled by Borland C ++ compiler version 3.1 on an IBM-compatible 486 computer. Currently, all programs run on MS-DOS and no graphical user interface is supported.

CHAPTER THREE

SENSOR DATA ACQUISITION PROCEDURE

A sensor is a device for receiving an external information such as heat, light, or pressure and transmitting it to a user. For most low cost land navigation applications, certain types of sensors are commonly used, namely distance, rotation, pressure and acceleration sensors. An inertial system is a unit in which rotation and acceleration sensors are integrated. Dead reckoning positioning systems have become common among commercial land navigation units aimed at urban use (Sakata 1996). They employ either a differential odometer or an odometer and a heading sensor to update a two dimensional position estimate in the absence of GPS (Geier et al. 1993). Although sensors are very useful devices, they require certain procedures to achieve their best performance. This chapter gives a brief overview of the current technology of some of inexpensive ($\leq$ $1000)
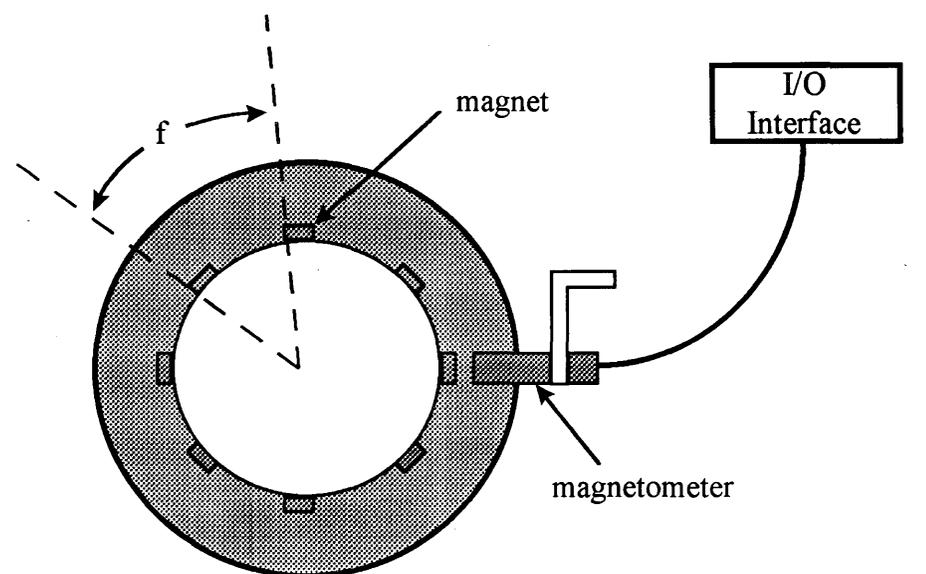
Figure 3.1. Odometer

sensors. Specific discussions of the barometric pressure transducer and the heading rate gyro employed in the current system are presented. Finally, the error models of barometric height, gyro heading rate, sensor heading and cross-track position, which are explicitly utilized in Chapter Four, are developed.

3.1 Overview of Sensor Technology

Odometer

An odometer, as shown Figure 3.1, is a device to provide the system with distance information. Using two odometers on each of the wheels of the vehicle may provide heading change information by taking the difference of the two odometer outputs. A distance is computed by observing the number of pulses detected from targets equally spaced around each wheel and then multiplying these pulse counts by a constant value f (scale factor) which depends on the perimeter of the wheel. Factors such as vehicle speed, tire pressure, vehicle payload and tire tread wear affect the actual tire size and thus the accuracy of measured distances.

Harris (1989) proposed the following theory of determining a heading change from differential odometers. Heading change is observed by differentiating the two odometer distance measurements from differential odometers as shown in Figure 3.2. The mean distance traveled over a data interval Δd is determined by
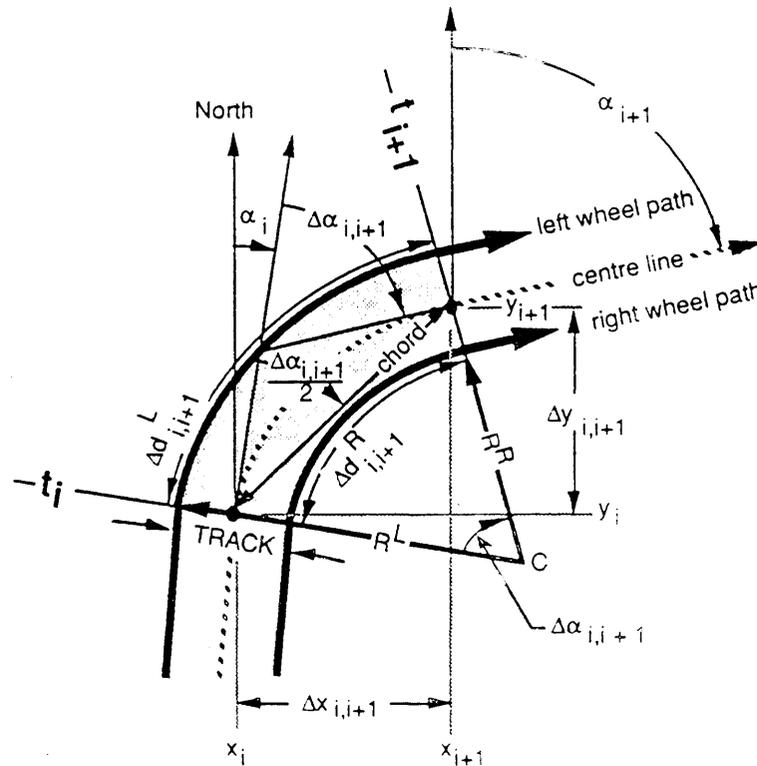
Figure 3.2. Differential Odometer Geometry from (Harris 1989)

$$\Delta d = \frac{\left(\Delta d^L - \Delta d^R\right)}{2}$$ (3.1)

where

$$\Delta d^L = d_{i+1}^L - d_i^L$$
$$\Delta d^R = d_{i+1}^R - d_i^R$$ (3.2)

and

d_i^L distance measured at time t_i by left wheel odometer,

d_i^R distance measured at time t_i by right wheel odometer,

d_{i+1}^L distance measured at time t_{i+1} by left wheel odometer,

d_{i+1}^R distance measured at time t_{i+1} by right wheel odometer.

A heading change over a data interval $\Delta\alpha$ is computed using equations (3.1) and (3.2) and the width of the vehicle's wheel path, TRACK, as

$$\Delta\alpha = \frac{\left(\Delta d^L - \Delta d^R\right)}{TRACK} \qquad (3.3)$$
$$= \alpha_{i+1} - \alpha_i$$

$$TRACK = R^L - R^R \qquad (3.4)$$

where

α_i azimuth heading of vehicle's forward direction at epoch t_i,

α_{i+1} azimuth heading of vehicle's forward direction at epoch t_{i+1},

R_L radius of the left wheel's curvilinear path,

R_R radius of the right wheel's curvilinear path.

The measurement accuracy of the differential odometer heading change is affected by distance measurement errors.

Flux Gate Compass

A flux gate compass is a device which provides heading information by measuring the intensity of a local external magnetic field as shown in Figure 3.3. Thus, the heading angle is measured relative to the Earth's magnetic pole, not to geodetic north. Flux gate

compasses use a pair of perpendicular coils to measure the direction of the magnetic field.

By measuring a vector direction from the two coil voltages, the direction of the magnetic

field may be determined (Kao 1991).

Since the steel structure of a vehicle may be magnetized, the actual magnetic field

direction measured by a compass in the vehicle becomes that of the combined magnetic

field of the Earth and the vehicle itself. Kao also writes that the compass measurements

suffer from the large electric current generated by the rear defroster and short term

magnetic anomalies due to power lines, steel structures, freeway underpasses and tunnels.

Compasses rely on gravity to isolate the Earth's horizontal magnetic field, and thus

acceleration and platform motion create short term compass errors (KVH 1994). Replaced
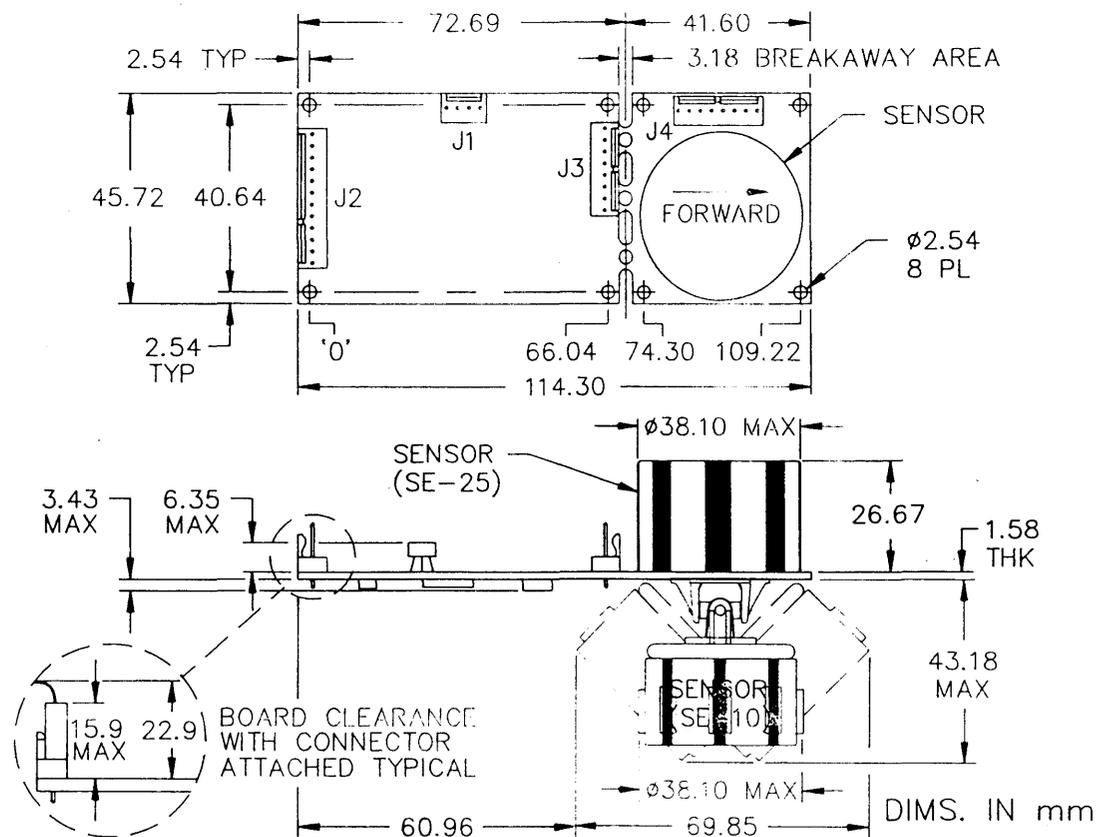
Figure 3.3. KVH C100 Compass Engine from (KVH 1994)

by gyros which have become available at reasonable prices, compasses are rarely used in current land vehicle navigation systems due to the above problem.

Rate Gyro

A rate gyro measures an angular velocity with respect to its rotation axis. Most gyros for land vehicle navigation are single axis heading rate sensors. For a constant sampling rate, the angular speeds are proportional to the relative headings. Gyros suffer from drifting caused by system noise, vibration, operation temperature change and other factors. Rate gyros are generally classified as one of these types: spinning rate, vibratory rate and optical gyros. Their relative merits are shown in Table 3.1.

Table 3.1 Relative Merits of Gyros from (Geier et al. 1993, Andrew 1994)

Type of Gyro	Drift [deg/hr]	Reliability	Pros	Cons
Spinning rate	100	Fair	High accuracy	Short life
Vibratory rate	100-3600	Good	Small size Long life Low cost	Errors caused by vibration Temperature sensitive
Optical (FOG)	10-18	Excellent	Very high accuracy No moving parts	Expensive

Traditionally the angular momentum of a spinning rotor is used to determine angular rate of displacement. Spinning rate gyros use a motor to spin a thin disk, as shown in Figure 3.4. When the axis of rotation of the disk is changed, gyroscopic forces occur which resist the change in direction of disk's momentum. These gyroscopic forces cause flexing of the spring spokes of the disk resulting in a change in disk position with respect
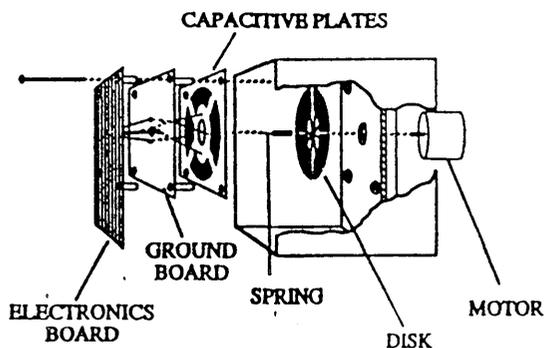
Figure 3.4. Spinning Rate Gyro from (Phillips 1993)

to the motor and chassis. These positional changes are detected by measurement of capacitance between the disk and the plates on the circuit board (Phillips 1993).

As the technology matures, cost and reliability continue to be of concern. Currently, the most popular type of gyros are piezoelectric vibratory rate gyros. Although their reliability and stability are inferior to interferometric gyros, such as FOG, they are of
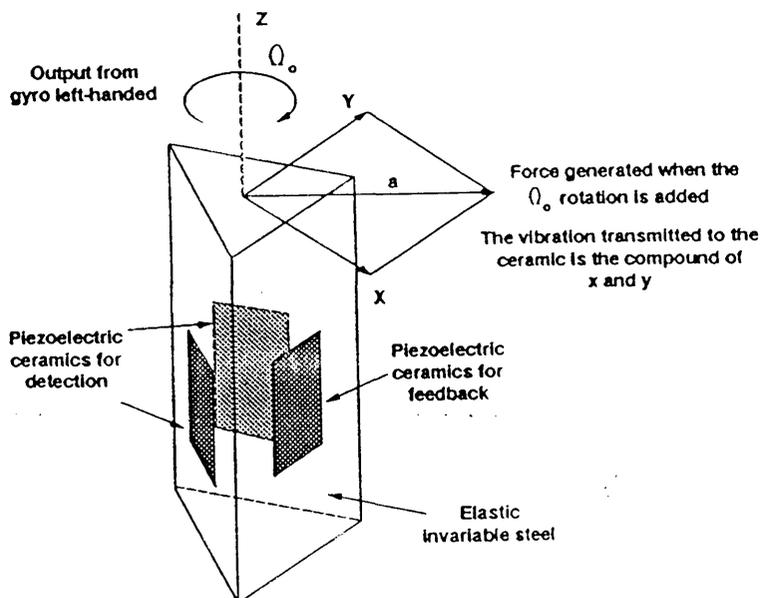
Figure 3.5. Murata GYROSTAR™ Piezoelectric Vibratory Rate Gyro from (Nakamura 1990)

exceptionally low cost. Piezoelectric vibratory rate gyros utilize a physical phenomenon called the Coriolis effect. As shown in Figure 3.5, an elastic steel bar and piezoelectric ceramic plates are pasted together and the vibrator is driven at the x axis. When the unit is rotated, an angular velocity is applied to the central (z) axis of the vibrator and a Coriolis force develops in the direction perpendicular to the vibration direction (Nakamura 1990). The structure of the GYROSTAR™ rate gyro of Murata Corp. is in the shape of an equilateral triangle to improve sensitivity and stability. This vibrating unit allows the left and right piezoelectric ceramics to be arranged in the direction of the compound vibration mode. The same ceramics may be used in both excitation and angular velocity detection, making both the structure and circuit simple. When rotating, the left and the right detection values are subtracted from each other as shown in Figure 3.6. Thus, the detection voltage is

$$(A+a)-(A-a) = 2a \tag{3.5}$$
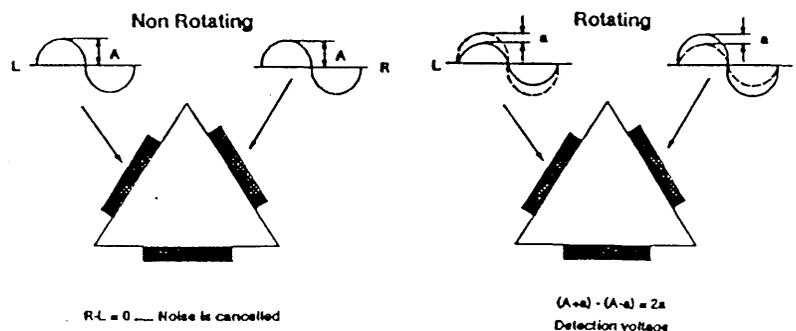
Figure 3.6. Murata GYROSTAR™ Output Detection Theory from (Nakamura 1990)

which yields a relatively large detection output of 90 degrees per second (Nakamura 1990).

Significant progress has been made in recent years towards the realization of practical interferometric fiber optic gyros (FOGs). Fiber optic gyros are beginning to replace mechanical gyros as their prices rapidly drop. FOGs are based on the phenomenon called the Sagnac effect that a circuit system has different optical path lengths in the two propagation directions when it is rotated (Perlmutter 1993). If two coherent light beams emanating from a common source travel in opposite directions around a stationary circular path (or ring) of radius R (with the source fixed on the ring), they are in phase when they return to the source as shown in Figure 3.7. If the ring is now rotated around its axis with a velocity v, the beam rotating with the ring has a longer optical path than that of the counter-rotating beam by a distance ΔL given by
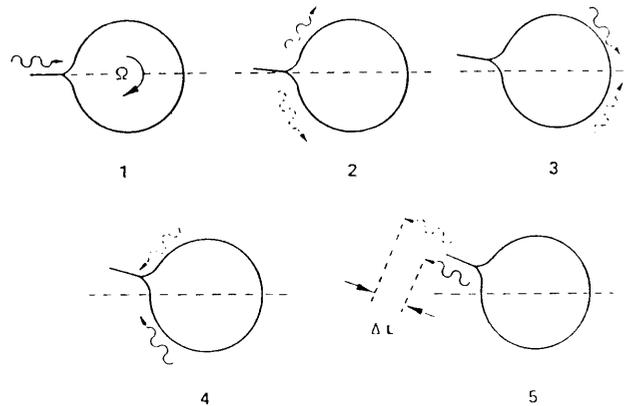
Figure 3.7. Path Length Difference Generated by the Sagnac Effect from (Liu & Adams 1990)

$$\Delta L = c \left(\frac{2\pi R v + 2\pi R v}{c^2} \right) = \frac{4\pi R v}{c} \qquad \text{[m]} \qquad (3.6)$$

where

c the speed of light in a vacuum [m/s],

π the ratio of the circumference of a circle to its diameter,

R Radius of the interferometer coil [m] and

v velocity of the rotation [m/s].

For monochromatic light of wavelength λ , this change in optical path length

$$\Delta L = \frac{\Delta \phi \lambda}{2\pi} \qquad \text{[m]} \qquad (3.7)$$

results in a non-reciprocal Sagnac phase difference

$$\Delta \phi = \frac{2\pi}{\lambda} \cdot \frac{4\pi R v}{c} = \frac{8\pi^2 R v}{\lambda c} \qquad \text{[rad]} \qquad (3.8)$$

between the two beams after a single pass around the ring. For a single ring (loop) enclosing an area $A = \pi R^2$, having N turns of fibre, and rotating with an angular velocity $\Omega = v / R$, equation (3.8) becomes

$$\Delta\phi = \frac{8\pi A\Omega N}{\lambda c} \ [\text{rad}].$$ (3.9)

Alternatively, we may express the resultant phase shift in terms of coil diameter $D = 2R$ and fiber length $L = \pi DN$,

$$\Delta\phi = \frac{2\pi \cdot 2R \cdot 2\pi RN \cdot \Omega}{\lambda c} = \frac{2\pi LD\Omega}{\lambda c} \ [\text{rad}].$$ (3.10)

Note that a constant angular velocity yields a constant phase difference. We may therefore think of a FOG as a rate gyro.

Barometric Pressure Transducer

Pressure transducers measure ambient pressures. A pressure transducer which is designed to measure barometric air pressures is called a barometric pressure transducer, barometric altimeter or simply barometer. Air pressure is measured by comparison with an opposing pressure. Mercury barometers use a mercury column. The aneroid barometer uses the tension of a spring connected to a vacuum box. Many portable altimeters used by hikers employ these principles. Different techniques are used in newer high-precision barometers. One technique used in military and commercial engine pressure sensors relies on a vibrating cylinder surrounded by a vacuum. As the pressure changes, the resonant frequency of the hoop mode of vibration also changes in a predictable fashion (Copley 1994). The conversion from air pressure to altitude is based on a theoretical standard

atmosphere and a corresponding pressure versus altitude curve. In reality, the real atmosphere varies widely from the theoretical standard and is quite dynamic. These variations must be taken into account when using a barometer.

Accelerometer

Accelerometers are used to measure the accelerations of a vehicle. Details of the principles of accelerometers are given in Lawrence (1993). All accelerometers operate by measuring the inertia force generated when a mass accelerates. The inertia force may
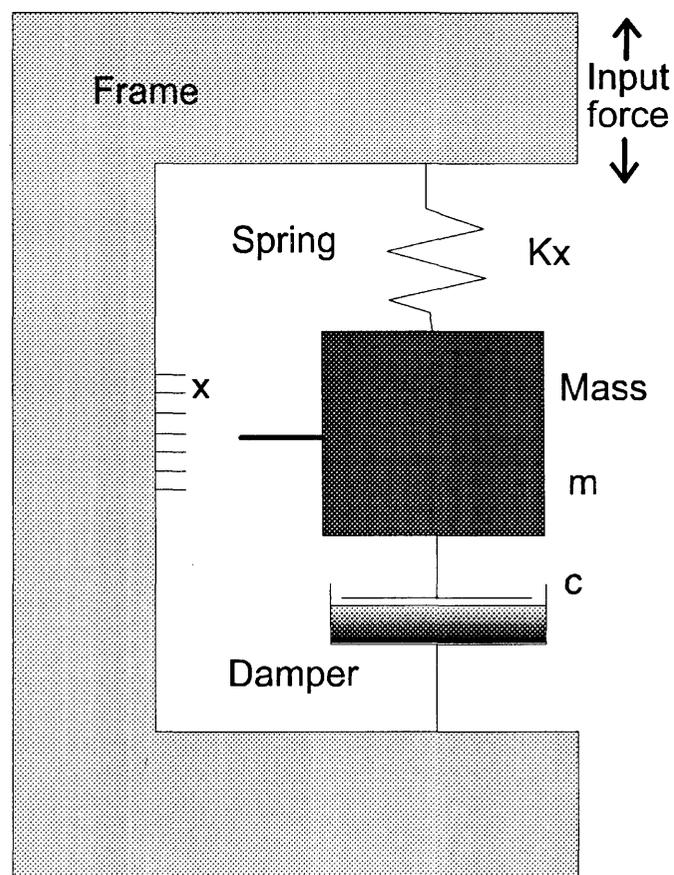
Figure 3.8. The Spring-Supported Mass Accelerometer

deflect a spring, whose deflection can be measured; it may change the tension in a string and hence its vibrating frequency; or it may move a capacitor plate closer to one fixed plate and further from another, causing a mismatch in the value of their capacitance and producing an output signal. Generally, for navigation purposes, only the longitudinal acceleration of a vehicle is of interest. The acceleration measurements are integrated to obtain vehicle velocities and traveling distances. Drifting problems are usually experienced during the integration operations (Kao 1991).

The spring-supported mass is a basic single degree of freedom accelerometer and is shown in Figure 3.8. The relationship between the size of the proof mass and the damping and stiffness of the spring determines its characteristics. The response of such a system to a force applied to the frame along the spring's axis may be determined by summing the force from inertia, fluid damping and spring displacement as

$$F = m\left(\frac{d^2 x}{dt^2}\right) + c\left(\frac{dx}{dt}\right) + K_x x \qquad \text{[N]} \qquad (3.11)$$

where

m weight of the mass [kg]

x displacement from the mass' rest position [m],

c damping coefficient [kg/s],

K_x spring stiffness [kg/s^2].

In some instruments the damping outweighs the inertia term so that equation (3.11) may be considered as first order. It is more usual for the inertia term to dominate, and the equation to be second order.

If the acceleration is steady and the mass displacement is steady, initial transient oscillations have subsided and the result is

$$m\left(\frac{d^2x}{dt^2}\right) = -K_x x .$$

(3.12)

That is, the inertia force is balanced by the opposing spring force and x may be considered as a measure of the acceleration.

3.2 Description of Selected Sensors

3.2.1 Barometric Pressure Transducer

A Viatran Model 246 barometric pressure transducer, shown in Figure 3.9, is used

for this project to measure barometric heights. This barometer is designed to measure

barometric pressures to within 0.01" Hg (Viatran 1996). Its full scale pressure range is

25" Hg to 32" Hg absolute which corresponds to a linear output of approximately 0 to 5

VDC (Viatran 1996). Specifications for the Viatran Model 246 are given in Table 3.2.

In order to examine the pressure output in the SI unit Pascal, the following

conversion is necessary. The particular barometer used was precisely calibrated at the

factory for

- 0.006 volts at 25.0" Hg and

4.988 volts at 32.0" Hg. (3.13)

NOTE:
1. ALL DIMENSIONS ARE NOMINAL, IN INCHES
   AND FOR REFERENCE PURPOSES ONLY

UNIT INFORMATION
LASER MARKED
ON HOUSING
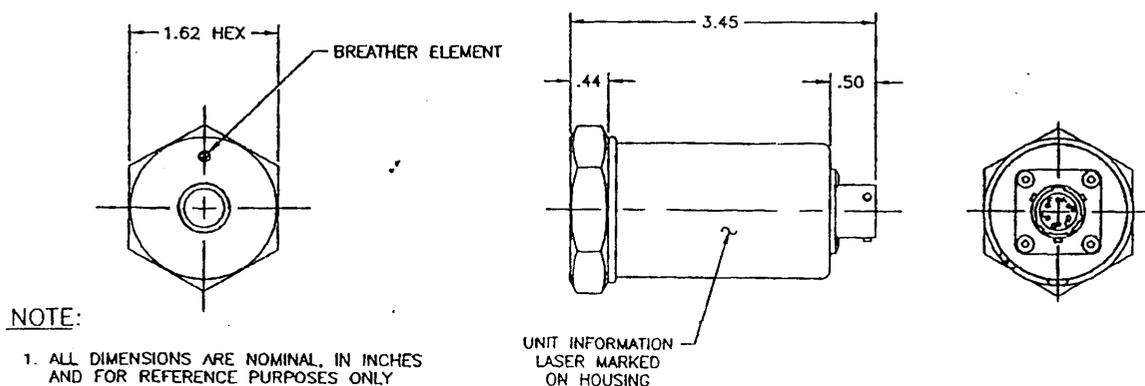
Figure 3.9. Viatran Model 246 Electronic Barometer from (Viatran 1996)

Pressure expressed in inches of Hg may be converted to Pascal using

$$\text{Pascal} = g \cdot \rho \cdot \text{mm Hg} \cdot 1000. \qquad (3.14)$$

For the values of (3.13),

Table 3.2 Viatran Model 246 Product Specifications from (Viatran 1996)

Full Scale Pressure Range	25" to 32" Hg absolute
Total Error Band due to Non-Linearity & Hysterisis & Repeatability	$\leq \pm 0.01$" Hg
Response Time	$\leq \pm 5$ msec
Zero Repeat After 100°F Temperature Shift	$\leq \pm 0.007$" Hg
Compensated Temperature Range	0°F to +200°F
Operating Temperature Range	-40°F to +250°F
Temperature Effect on Zero	$\leq \pm 0.0018$" Hg per 1°F
Temperature Effect on Span	$\leq \pm 0.0018$" Hg per 1°F
Long Term Stability	$\leq \pm 0.035$" Hg per 6 months
Supply Voltage	8.5 to 40 VDC
Power Supply Regulation	$\leq \pm 0.000007$" Hg per Volt
Output Signal	0 to 5 VDC
Output Signal Noise Levels	≤ 10 mV peak to peak

25" Hg = 635 mm Hg = 84464.31164 Pa and

32" Hg = 812.8 mm Hg = 108114.3189 Pa   (3.15)

where

g = 9.78049 [m/s^2]   gravity force,

ρ = 13600 [kg m^3]   density of Hg.

A linear relation between pressure in Pascal p and output voltage v is given from equations (3.13) and (3.15) as

$$p = (84464.31164 + 4735.684273(v + 0.006))\ [Pa].$$ (3.16)

Equation (3.16) gives air pressure in Pascals from the Viatran Model 246 barometer. The
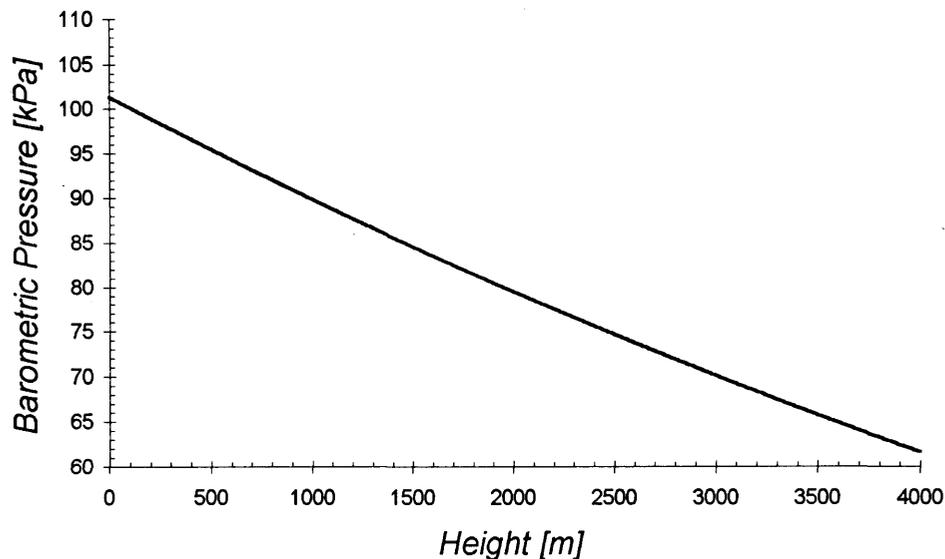
Figure 3.10. The US Standard Atmosphere Pressure-To-Height Conversion Chart from (Lutgens & Tarbuck 1982)

U.S. Standard Atmosphere (Lutgens & Tarbuck 1982) is used for the pressure-to-height conversion as shown in Figure 3.10. Since this table only defines the theoretical relationship between pressure and height, following errors must be taken into account in order to compensate the deviation from this model.

The error characteristics of the barometer vary depending on the environment. In a static environment, major error sources are the bias of the sensor and long term drift mainly due to the change in local pressure as shown in Figure 3.11. For vehicle navigation, the barometer is commonly located in a car. As a result, barometric measurements are disturbed by changes in ambient pressure caused by the acceleration and deceleration of the vehicle. Figure 3.12 shows this effect. As the vehicle accelerates, it creates a rise of pressure in the vehicle which pushes down the measured height. At the same time, a
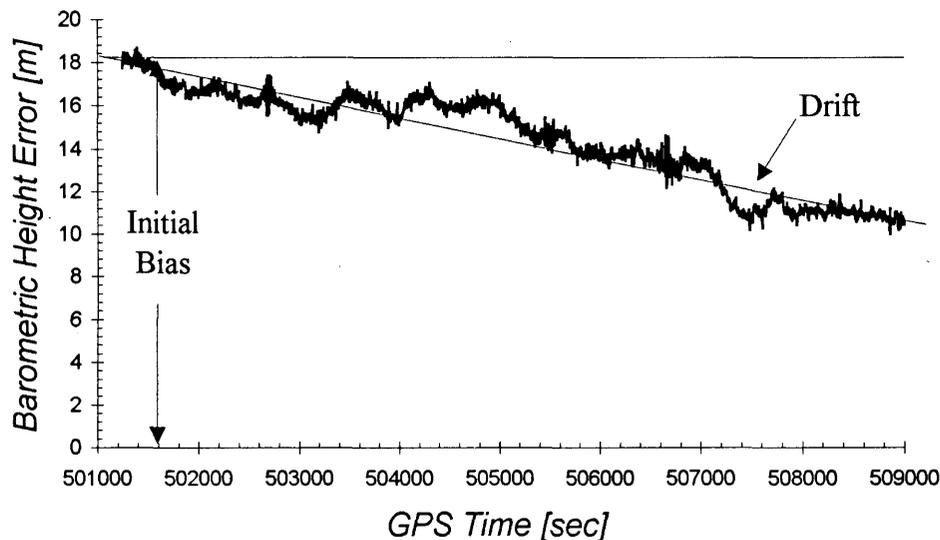
Figure 3.11. Viatran Model 246 Electronic Barometer Measurement Error in a Typical Static Environment
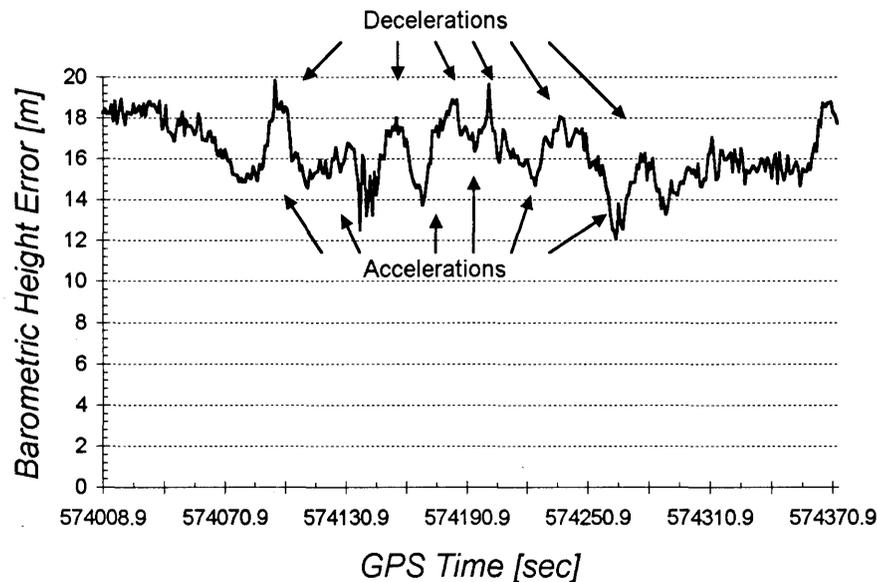
Figure 3.12. Viatran Model 246 Electric Barometer Measurement Error in a Typical Dynamic Environment

certain amount of air escapes from the vehicle's compartment and the barometric height increases to a certain extent. Other measurement errors may include a deviation from theoretical standard atmosphere caused by non-standard humidity and temperature, nonlinearities caused by vertically moving air, wind, weather fronts and conversion error. It is nearly impossible to distinguish the causes of error in dynamic environments and these errors are generally insignificant (Lutgens & Tarbuck 1982). Therefore, these errors are grouped into the constant bias or the drift.

3.2.2 Fiber Optic Gyro

For land vehicle navigation purposes, a single axis gyro is commonly used to determine vehicle headings. An Andrew AUTOGYRO™, shown in Figure 3.13, was

selected for this project. This gyro is a single axis, digital output, interferometric fiber optic rate gyro. The AUTOGYRO™ configuration is given in Figure 3.14. The AUTOGYRO™ employs an analog electronic signal processor and an all-fiber optical system (Andrew Corp. 1994). The fiber consists of a elliptical core of germanium surrounded by a fluorine-doped inner cladding (Allen et al. 1994). This fiber exhibits significantly lower coefficients to thermal and stress environments. The Andrew AUTOGYRO™ specifications are given in Table 3.3. The device measures angular rate which allows the vehicle turning angle to be accurately measured. Powered by a 12 VDC car battery, the AUTOGYRO™ produces a digitized output of incremental angular rotation every 0.1 second. The output is equivalent to the average rotation rate over that period (Andrew Corp. 1994).

Table 3.3 Andrew AUTOGYRO™ Product Specifications from (Andrew 1994)

Input Rotation Rate	± 100 deg/sec
Minimum Detectable Rotation Rate (in 100Hz bandwidth)	± 0.02 deg/sec (60 deg/hr) Angle Random Walk
Bias Drift (at stabilized temperature)	0.005 deg/sec, rms (18 deg/hr)
Scale Factor Non-Linearity	0.25%, rms
Scale Factor Temperature Stability (over temperature range)	0.5%, rms
Warm-up Time	1 second
Operating Temperature	-40°C to +75°C
Power	+9 to +18 VDC, 630mA
Sensor Output	RS-232E, 9600 baud
Connector Type	9-pin subminiature (DB-9 plug)
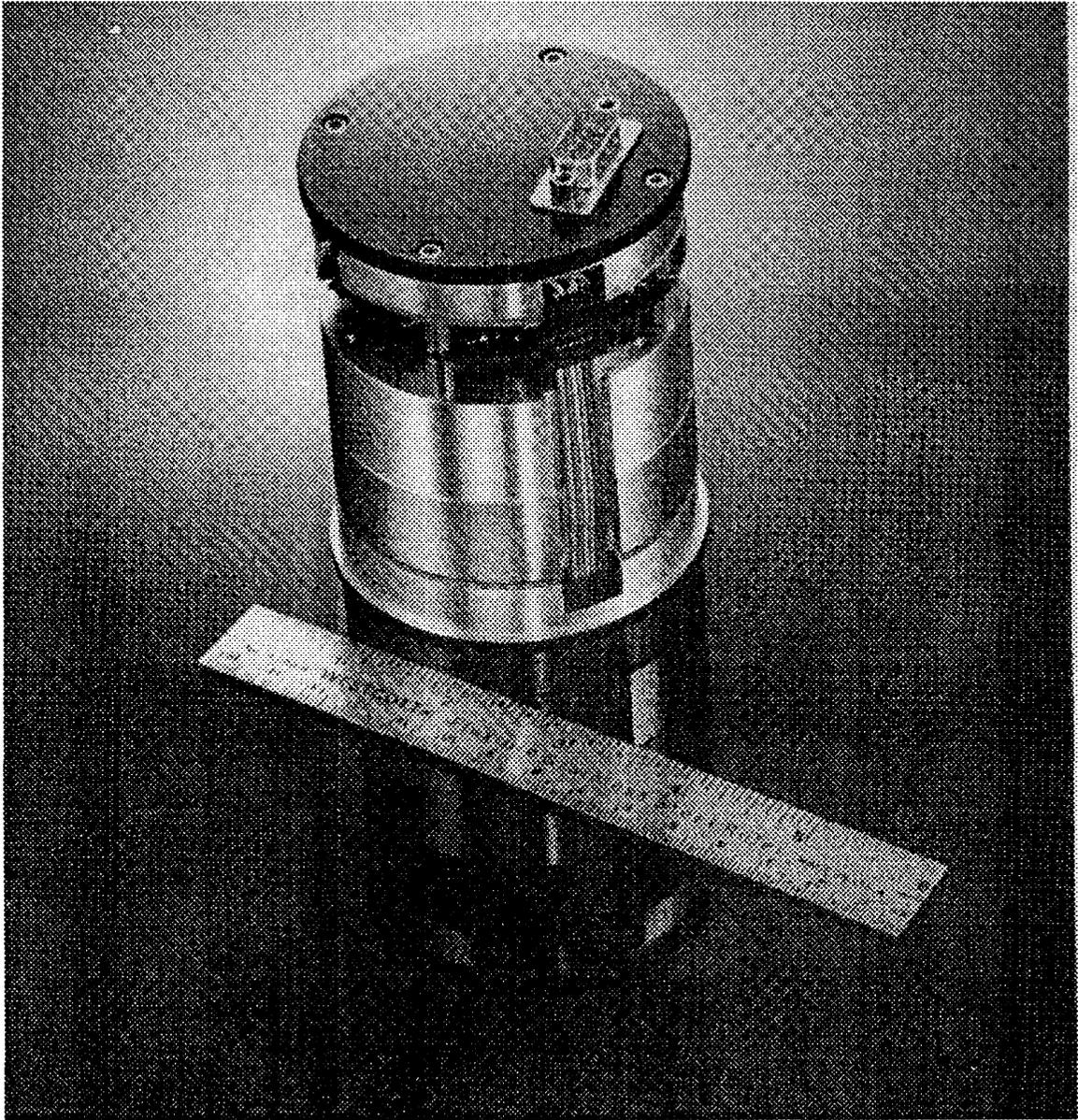
Figure 3.13. Andrew AUTOGYRO™ from (Allen et al. 1994)
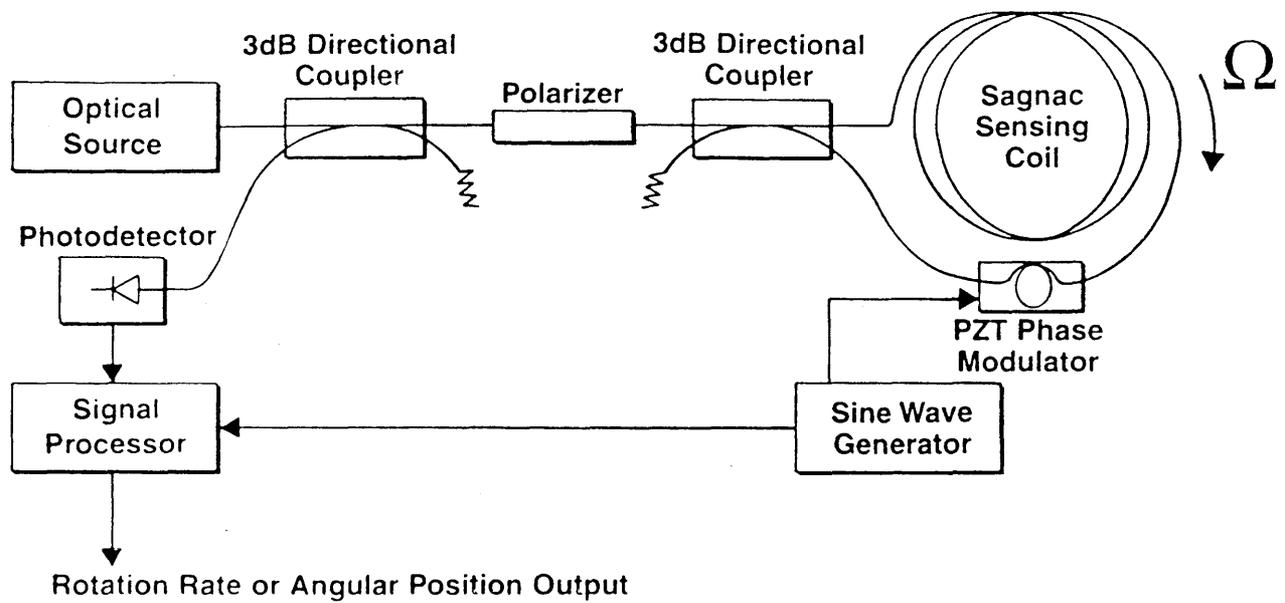
a) Open-Loop
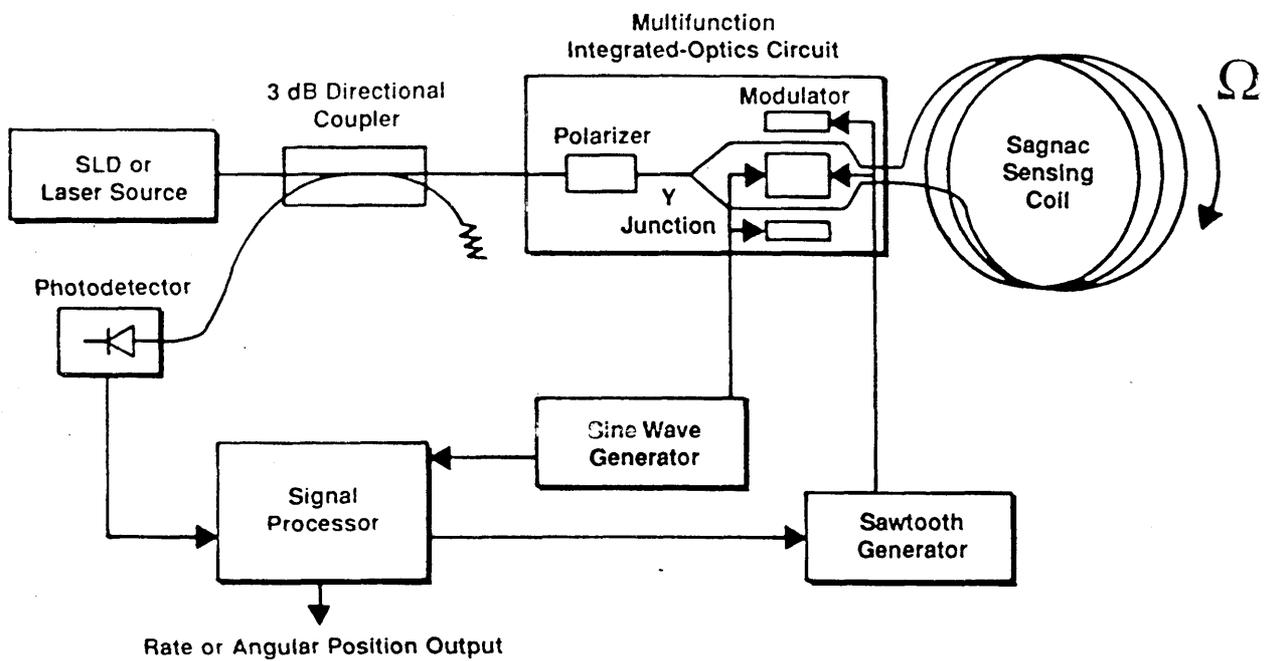
b) Closed Loop

Figure 3.14. Andrew AUTOGYRO™ Configuration from (Bennett & Enge 1994)
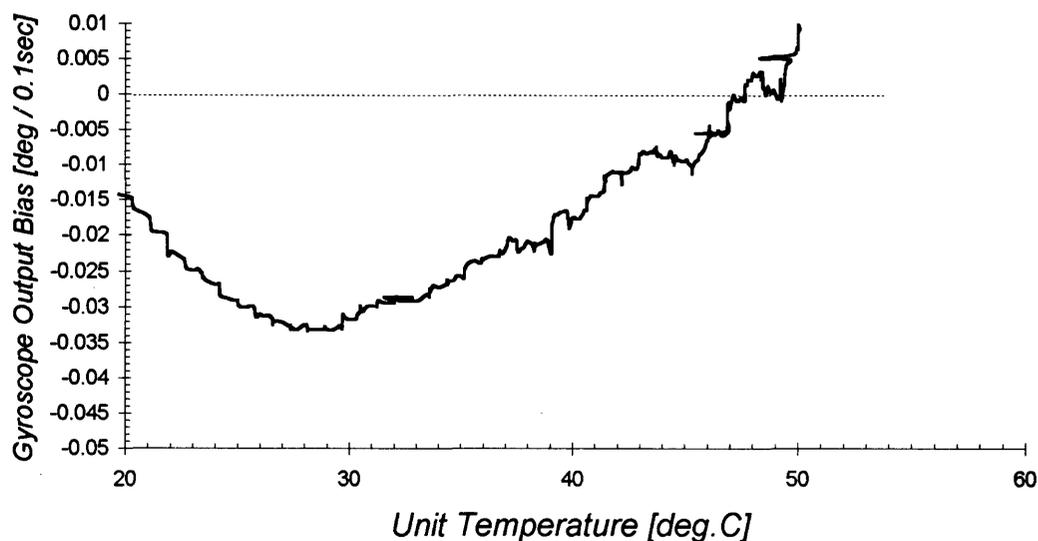
Figure 3.15. Andrew AUTOGYRO™ Output Bias vs. Unit Temperature

Figure 3.15 shows the relationship between unit temperature and gyro output bias. Although the bias can be largely corrected by the temperature-bias compensation table provided by the manufacturer, it is likely that a residual bias will remain. Appropriate calibration procedures and careful gyro temperature control should reduce this error.

Previous gyro experiment, Figure 3.16, have indicated that the gyro scale factor increases at an unexpected rate as the unit temperature rises. It is, therefore, necessary to correct the unit scale factor as a function of unit temperature. A scale factor may be determined by rotating a gyro unit a certain number of degrees while recording its outputs. The scale factor is then computed by

$$f = \Phi / n \tag{3.17}$$

where

f gyro scale factor,

Φ rotation given to the unit in degrees,

n digital gyro output count.

Performing this procedure at the desired unit temperature gives a gyro scale factor for that temperature, provided that the unit has an acceptable repeatability. Figure 3.16, obtained from a laboratory experiment conducted on August 23, 1996, shows the relationship between the scale factor and unit temperature. Since unit temperature will vary with the testing environment, appropriate scale factors must be determined with
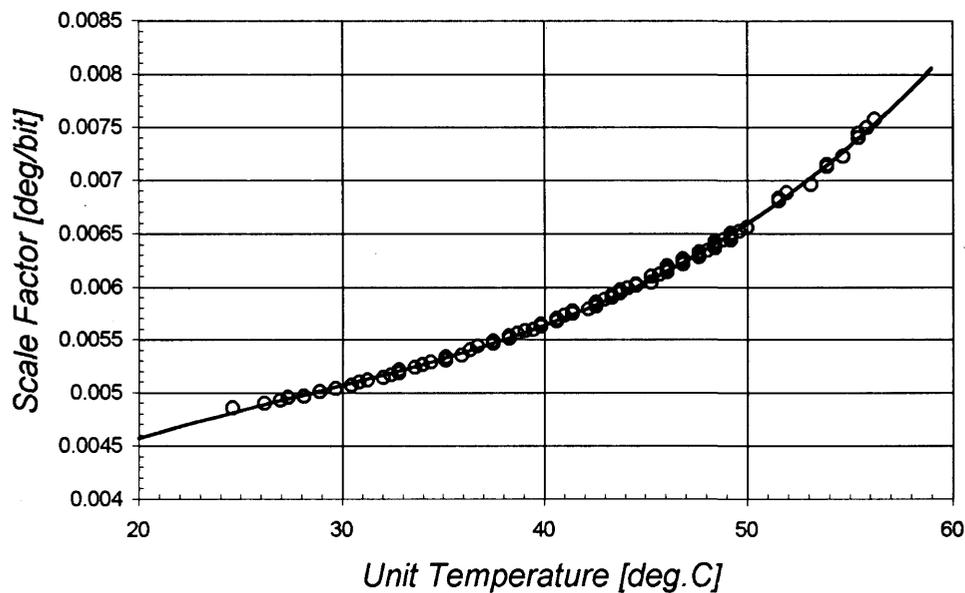
Figure 3.16. Andrew AUTOGYRO^{TM} Scale Factor vs. Unit Temperature

respect to actual operating temperature. The scale factor is modeled by a 3rd order polynomial equation (curve in figure 3.16) as

$$f(x) = a_0 + a_1 x + a_2 x^2 + a_3 x^3 \qquad (3.18)$$

where

x is gyro unit temperature [°C],

$a_0 = 0.00253199307659$,

$a_1 = 0.00016878071261$,

$a_2 = -0.00000439984368$,

$a_3 = 0.00000005296039$.
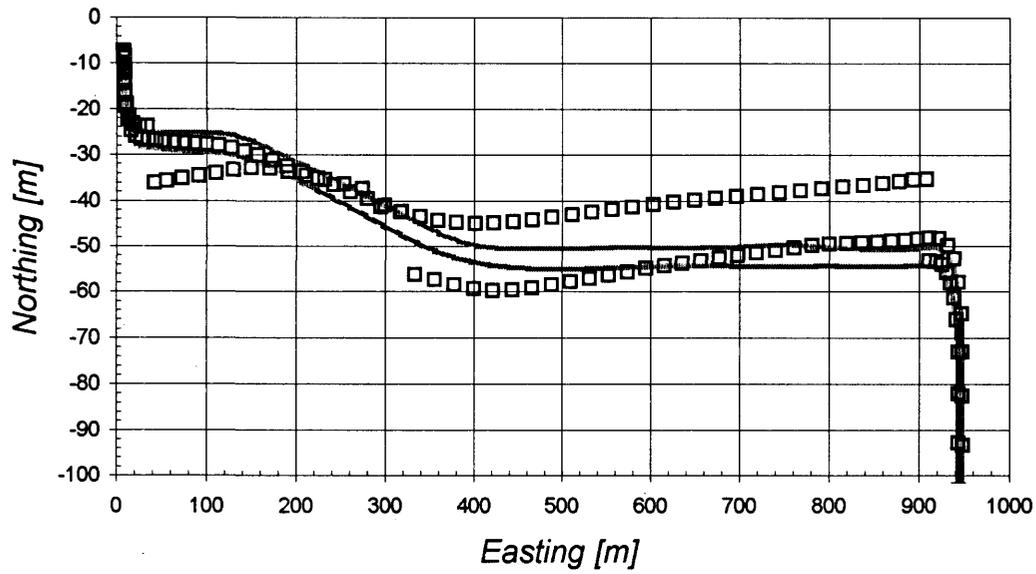
**Figure 3.17. Sensor Heading Constraint Solutions without Corrected Scale Factor.
Default Scale Factor (0.00499 [deg/bit]) Used.
Solid Line Indicates Reference Trajectory**
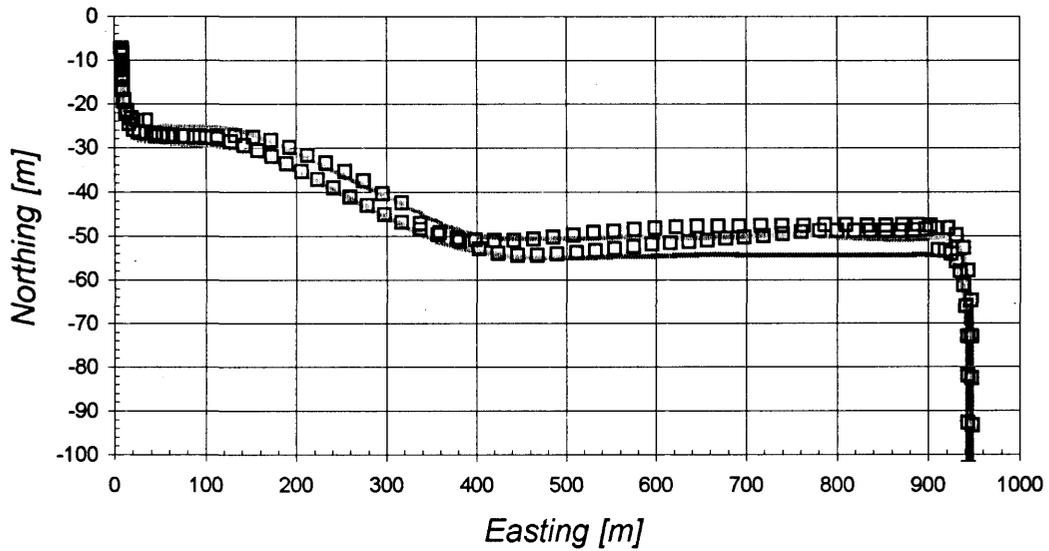
**Figure 3.18. Sensor Heading Constraint Solutions with Corrected Scale Factor. Solid
Line Indicates Reference Trajectory**

The effect of appropriate scale factor determination is obvious from figures 3.17 and 3.18. Forward and reverse runs are shown in each figure. Improper scale factor may cause severe position estimate displacement and a filter breakdown if the Kalman position estimator is employed. Equation (3.18) is implemented in the navigation module to compute the scale factor as a function of unit temperature. The data logging software is designed to include gyro unit temperature output. As the unit ages, the scale factor may change because of the mechanical degradation. Therefore, the coefficients of (3.18) should periodically be updated.

3.3 Sensor Error Models

In this section, sensor error models are developed. It is necessary to determine error models for the barometric height, gyro heading rate and sensor heading to evaluate the weights of the sensor measurements. The sensor heading error model is then implemented in the cross-track position error model. These models are used in Chapter Four to calculate weights and variances of sensor measurements.

3.3.1 Barometric Height Error Model

For barometric height, the primary error source is the barometric height offset with respect to GPS height. This is mainly due to the initial sensor bias, the disagreement between barometric (or orthometric) height and GPS height, and the height offset between the sensor unit and the GPS antenna. The bias error is constant and, therefore, it may be

removed by initial calibration. The residual (non-constant) errors are absorbed by the second error source, height drift, and need not be taken into account at this point.

The secondary error source is the height drift caused by changes in pressure around the barometer. The ambient barometric pressure slowly changes as high and low pressure systems approach. In a stationary environment, the barometric height change of approximately 50 metres in an hour has been observed by the author. For land navigation applications, height drift is also caused by in-vehicle pressure disturbances due to the acceleration and deceleration of the vehicle, temperature changes, etc. Additional errors may include the aging of the sensor unit as well as hardware and software limitations.

Assuming that GPS updates are obtained consistently (e.g. every 10 minutes), we may consider the height offset and the height drift rate to be constant. The height error model may then be defined as

$$
\begin{aligned}
\varepsilon_b(t_0) &= \varepsilon_b \\
\varepsilon_b(t_{k+1}) &= \varepsilon_b(t_k) + \dot{\varepsilon}_b(t_k)\Delta t
\end{aligned}
$$

(3.19)

where

$\varepsilon_b(t_{k+1})$ barometric height error at time t_{k+1} [m],

ε_b barometric height offset (residual) error at the calibration time t_0 [m],

$\dot{\varepsilon}_b$ linear barometric height drift rate [m/s],

Δt update interval between t_k and t_{k+1} [s].

Modeling the long-term behavior of $\dot{\varepsilon}_b$ is extremely difficult since there are many factors which can alter the ambient pressure when the vehicle is not stationary. In this project, $\dot{\varepsilon}_b$ is assumed constant between calibration periods. Calibration may be performed when good GPS solutions are available. Therefore, good GPS coverage is periodically necessary (e.g. every ten minutes).

3.3.2 Gyro Heading Rate Error Model

The most significant gyro error source is the heading rate offset error due to the gyro bias. The heading rate offset is temperature-dependent and the manufacture often provides rate offset versus temperature charts (Andrew Corp. 1994). This error may be considered constant by stabilizing the gyro unit temperature at a certain value. Stabilizing the unit temperature is strongly suggested since it stabilizes the scale factor error as well.

The another significant error source is the gyro scale factor error. The scale factor error is negligible as long as the vehicle follows a straight line. However, it becomes obvious as the heading rate increases (e.g. sudden heading change). Thus, the scale factor error is a function of the substantial heading rate. The author has found that the scale factor error fluctuates with unit temperature. This error may be minimized by calibrating the gyro at the operational unit temperature.

The gyro drift error is an outstanding error source as well. This may be caused by temperature change, instability of the unit, environmental stresses, mechanical failures, and so on. Other errors such as g-sensitivity, cross-axis sensitivity, nonlinear errors (Abbott &

Powell, 1995) and the effect of the earth rotation (Da & Dedes, 1995) are ignored in this thesis since they are negligible for most land navigation applications.

Assuming that the gyro unit temperature is stabilized, the gyro error model may be expressed as

$$
\begin{aligned}
\varepsilon_g(t_0) &= \varepsilon_g \\
\varepsilon_g(t_{k+1}) &= \varepsilon_g(t_k) + \dot{\varepsilon}_g \Delta t
\end{aligned}
$$

(3.20)

where

$\varepsilon_g(t_{k+1})$ gyro error at t_{k+1} [rad/s],

ε_g gyro heading rate offset (residual) error at t_0 [rad/s],

$\dot{\varepsilon}_g$ gyro drift error [rad/s^2],

Δt update interval between t_k and t_{k+1} [s].

Note that in this thesis the gyro offset is calibrated when the vehicle is stationary and the heading change is not expected. We may say that the gyro drift error $\dot{\varepsilon}_g$ is constant between calibrations. Needless to say, periodic calibration is recommended to validate this assumption. Although the scale factor error and gyro offset may be evaluated with respect to the reference heading rate, this technique is not implemented in the current system.

3.3.3 Sensor Heading Error Model

Since the fibre optic gyro only senses the change in vehicle heading, the initial heading must be obtained from GPS or other sources. The heading error due to an inaccurate initial heading should be included. The sensor heading error may be written as

$$\varepsilon_\Theta(t_0) = \varepsilon_\Theta$$
$$\varepsilon_\Theta(t_{k+1}) = \varepsilon_\Theta(t_k) + \varepsilon_g(t_{k+1})$$

(3.21)

where

$\varepsilon_\Theta(t_{k+1})$ heading error at t_{k+1} [rad],

ε_Θ initial heading error [rad],

$\varepsilon_g(t_{k+1})$ gyro error at t_{k+1} computed from equation (3.18) [rad/s].

Since the gyro error grows over time, the heading error may become intolerable after a certain period. Good GPS geometry (e.g. at intersections) may be used to frequently update the gyro (e.g. every five minutes).

3.3.4 Cross-Track Position Error Model

Finally, the cross-track position error model is obtained using equation (3.21). The cross-track position error may be expressed as

$$\varepsilon_{CT}(t_0) = \varepsilon_{GPS}$$
$$\varepsilon_{CT}(t_{k+1}) = \varepsilon_{CT}(t_k) + v_k \tan(\varepsilon_\Theta(t_{k+1}))\Delta t$$

(3.22)

where

$\epsilon_{CT}(t_{k+1})$ cross-track position error at t_{k+1} [m],

ϵ_{GPS} GPS cross-track position estimate error [m],

v_k vehicle velocity [m/s],

$\epsilon_\Theta(t_{k+1})$ heading error at t_{k+1} obtained from equation (3.21) [rad],

Δt update interval between t_k and t_{k+1} [s].

These parameters are illustrated in Figure 3.19.

It is uncertain in urban areas when good GPS coverage can be obtained. Therefore, the system is designed to initiate the calibration process whenever the good GPS coverage is obtained..
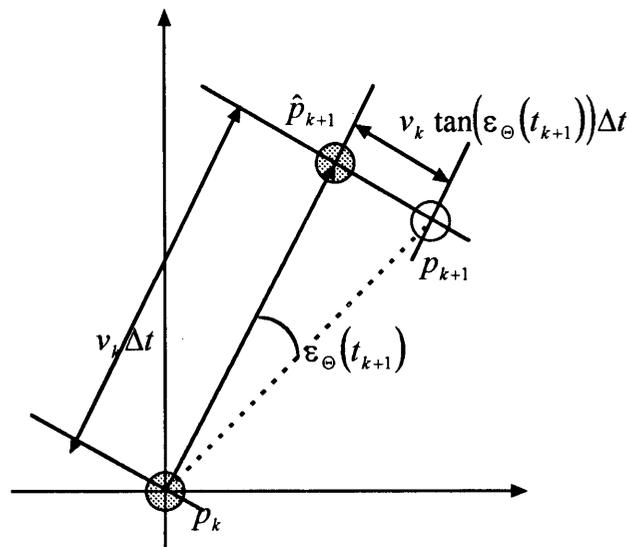
Figure 3.19. Cross-Track Position Displacement Induced by Sensor Heading Error.

CHAPTER FOUR

SENSOR CONSTRAINT POSITIONING THEORY

This chapter discusses the sensor constraint positioning algorithm. In sensor constraint positioning, position estimates are constrained by the sensor measurements when GPS measurements are weak, erroneous or absent. To implement sensor constraint positioning, an augmented least squares estimator is introduced and developed.

4.1 Concept of Sensor Constraint Positioning

In sensor constraint positioning, information regarding the relative position of a vehicle is provided by non-GPS sensors and used to constrain the position estimate so that it is less affected by the number, quality and geometry of GPS measurements. In this project, the vehicle height and heading information, which may be obtained from the barometer and gyro, are selected as constraints. A barometric height constrains vertical position while a sensor heading constrains horizontal position.

4.2 Mathematical Models

A mathematical model of the GPS range measurement is given by

$$p = \rho + d\rho + c(dt - dT) + d_{ion} + d_{trop} + \varepsilon_p \qquad (4.1)$$

where

$\quad p \qquad\qquad$ range measurement [m],

$\rho = \|\mathbf{r} - \mathbf{R}\|$ geometric range [m],

$\mathbf{r}$ position vector of a satellite,

$\mathbf{R}$ position vector of a land vehicle,

$d\rho$ range error induced by orbital error [m],

dt satellite clock error [s],

dT receiver clock error [s],

d_{ion}, d_{trop} ionospheric and tropospheric delays [m],

ε_p receiver noise [m].

For the barometric height measurement, the mathematical model may be simplified as

$$h = h_b + \varepsilon_b \tag{4.2}$$

where

h_b barometric height measurement [m],

h true height [m],

ε_b barometric height measurement error [m].

For the horizontal heading measurement, as shown in Figure 4.1, two consecutive coordinates are required to construct a mathematical model as

$$\Theta = \tan^{-1}\left(\frac{d\lambda}{d\phi}\right) + \varepsilon_\Theta \tag{4.3}$$

where

Θ heading defined clockwise from zero to 2π relative to north [rad],

$d\phi$ distance between two consecutive epochs in latitude [m],

$d\lambda$ distance between two consecutive epochs in longitude [m],

ε_Θ heading error [rad].

Note that the barometric height and heading errors are evaluated by equations (3.17) and (3.19).
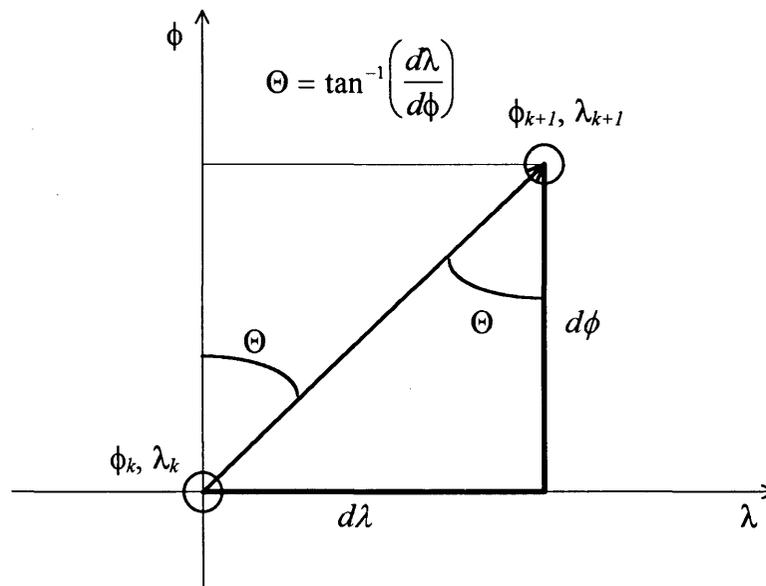
Figure 4.1. Heading Computation

4.3 Augmented Least Squares Estimator

This section describes an algorithm for sensor constraint least squares positioning. It is in fact an augmented weighted least squares estimator. Consider the parametric weighted least squares equation. Given the design matrix $\mathbf{A}$, the covariance matrix of

measurements $\mathbf{C}_l$, the *a priori* position estimate vector $\mathbf{x}^0$ and the misclosure vector $\mathbf{w}^0$, a solution vector $\hat{\mathbf{x}}$ may be obtained by the following equations (Krakiwsky, 1990)

$$\mathbf{w}^0 = f(\mathbf{x}^0, \mathbf{l}) \tag{4.4}$$

$$\delta = -\left[\mathbf{A}^T \mathbf{C}_l^{-1} \mathbf{A}\right]^{-1} \mathbf{A}^T \mathbf{C}_l^{-1} \mathbf{w}^0 \tag{4.5}$$

$$\hat{\mathbf{x}} = \mathbf{x}^0 + \delta \tag{4.6}$$

where

$\mathbf{l}$ observation vector,

δ least squares adjustments to parameters.

An augmented design matrix $\mathbf{A}$ may be obtained by linearizing equations (4.1) to (4.3) with respect to the geodetic coordinate system and receiver clock offset. For a GPS range,

$$\mathbf{A}_i = \left[\frac{\partial p_i}{\partial \phi}, \ \frac{\partial p_i}{\partial \lambda}, \ \frac{\partial p_i}{\partial h}, \ -1\right] \tag{4.7}$$

for a barometric height,

$$\mathbf{A}_b = \begin{bmatrix} 0, & 0, & 1, & 0 \end{bmatrix} \tag{4.8}$$

and for heading

$$\mathbf{A}_\Theta = \left[-\frac{d\phi}{d\phi^2 + d\lambda^2}, \quad \frac{d\lambda}{d\phi^2 + d\lambda^2}, \quad 0, \quad 0 \right] \tag{4.9}$$

where

$d\phi$ distance between two consecutive epochs in latitude [m],

$d\lambda$ distance between two consecutive epochs in longitude [m].

Equations (4.7) to (4.9) form an augmented design matrix. Sensor height and heading inputs are treated as the measurements in this augmented least squares estimator. Solving equations (4.4) to (4.6) with the augmented design matrix yields height and heading constraint position estimates.

The effect of the constraint is defined by the diagonal elements of the weight matrix $\mathbf{C}_l^{-1}$

$$\mathbf{C}_l^{-1} = \begin{bmatrix} \sigma_1^2 & 0 & \cdots & 0 & 0 & 0 \\ 0 & \sigma_2^2 & \cdots & 0 & 0 & 0 \\ \vdots & \vdots & \ddots & \vdots & \vdots & \vdots \\ 0 & 0 & \cdots & \sigma_n^2 & 0 & 0 \\ 0 & 0 & \cdots & 0 & \sigma_b^2 & 0 \\ 0 & 0 & \cdots & 0 & 0 & \sigma_\Theta^2 \end{bmatrix}^{-1} \tag{4.10}$$

where

$\sigma_1^2, \cdots, \sigma_n^2$ GPS range error variances [m^2],

σ_b^2 barometric height error variance [m^2],

$\sigma_\ominus^2$ sensor heading error variance [rad^2].

The navigation program is based on C^{3}NAV^{TM} developed at the University of Calgary. It is capable of smoothing range measurements by carrier phase observations to improve the accuracy (Cannon & Lachapelle 1992). A smoothed range measurement may be given by

$$\hat{P}_k = WP_k + (1-W)\{\hat{P}_{k-1} + (\Phi_k - \Phi_{k-1})\} \tag{4.11}$$

where

$\hat{P}_k, \hat{P}_{k-1}$ smoothed range measurement at t_k and t_{k-1} [m],

W weight of a range measurement that is decreased from 1.0 to zero by a specified number at each epoch,

P_k raw range measurement at t_k [m],

$1-W$ weight of carrier phase measurements,

Φ_k, Φ_{k-1} measured carrier phase measurement at t_k and t_{k-1} [m].

The variance of smoothed range measurements may be expressed as a function of the range and carrier phase errors. The smoothed range measurement variance may be given as

$$\sigma_P^2 \approx \sigma_\varepsilon^2 + \sigma_{\delta trop}^2 + \sigma_{\delta ion}^2 + \sigma_{\delta\rho}^2 + \sigma_{\delta dt}^2 \qquad (4.12)$$

where

σ_ε^2 measurement noise [m²],

$\sigma_{\delta trop}^2$ tropospheric delay [m²],

$\sigma_{\delta ion}^2$ ionospheric delay [m²],

$\sigma_{\delta\rho}^2$ orbital error [m²],

$\sigma_{\delta dt}^2$ satellite clock error [m²].

Martin (1980) gives tropospheric and ionospheric error models as a function of elevation as

$$\sigma^2_{\delta trop} = \left\{ \Delta C N(h) \csc(E) \right\}^2$$

$$= \left\{ \Delta C \exp\left(\frac{-0.034}{T} h \right) \csc(E) \right\}^2 \tag{4.13}$$

$$\sigma^2_{\delta ion} = \left[\frac{-b}{4\pi^2 f^2} I_v \left\{ \csc(E^2 + 20.3^2) \right\}^{0.5} \right]^2$$

$$= \left\{ \Delta K \csc\left(E^2 + 20.3^2 \right)^{0.5} \right\}^2 \tag{4.14}$$

where

$N(h)$ linear integral of user to satellite refractivity function,

ΔC residual compensation magnitude ($\Delta C \approx 0.1$ m),

T temperature,

h vehicle altitude,

E satellite elevation in degrees,

b $= 1.6 \times 10^3 =$ constant in MKS unit,

f carrier frequency in Hz,

I_v vertical electron content in electrons $/ m^2$,

ΔK fractional value of reduced ionospheric delay ($0.5 < \Delta K < 5$ m).

The smoothed range measurement variance should decrease proportional to the weight of the carrier phase measurement. The resulting measurement variance may be expressed as

$$\sigma_\varepsilon^2 = W\sigma_{range}^2 + (1-W)\sigma_{phase}^2 \qquad (4.15)$$

where

W weight of a range measurement,

σ_{range}^2 range measurement error variance [m^2]

σ_{phase}^2 carrier phase measurement error variance [m^2].

Equations (4.12) to (4.15) are used to compute a GPS range variance.

The measurement error variances of barometric height and sensor heading at t_k are given by

$$\sigma_b^2(t_k) = \varepsilon_b(t_k)^2 \qquad (4.16)$$

$$\sigma_\Theta^2(t_k) = \varepsilon_\Theta(t_k)^2 \qquad (4.17)$$

where

$\varepsilon_b(t_k)$ barometric height error at t_k from equation (3.17),

$\varepsilon_\ominus(t_k)$ sensor heading error at t_k from equation (3.19).

Note that the variances computed by equations (4.16) and (4.17) increase with time, reflecting the cumulative sensor measurement errors. Equations (4.15) to (4.17) allow a navigation algorithm to find an optimal position estimate at any given time.

CHAPTER FIVE

KALMAN FILTERS

This chapter describes the Kalman filter algorithm and its implementation. First, the general Kalman filter algorithm is briefly presented. Then, the sensor filters are developed. Finally, a Kalman filter version of the sensor constraint position estimator is designed and discussed.

5.1 Kalman Filter Algorithm

The general discrete Kalman filter algorithm is briefly described in this section. Detailed discussions of Kalman filters are given in Brown & Hwang (1992) and Gelb et al. (1974). Let us assume that the random process to be estimated can be modeled in the linear form

$$\mathbf{x}_{k+1} = \phi_k \mathbf{x}_k + \mathbf{w}_k \tag{5.1}$$

where

$\mathbf{x}_{k+1}$ process state vector at time t_{k+1},

ϕ_k transition matrix relating $\mathbf{x}_k$ and $\mathbf{x}_{k+1}$ in absence of a forcing function,

$\mathbf{w}_k$ white noise with known system noise covariance structure

and measurement of the process is assumed to occur at discrete points in time according to the linear relationship

$$\mathbf{z}_k = \mathbf{A}_k \mathbf{x}_k + \mathbf{v}_k \qquad (5.2)$$

where

$\mathbf{z}_k$ measurement vector at t_k,

$\mathbf{A}_k$ design matrix which gives noiseless connection between the measurement and state vector at t_k,

$\mathbf{v}_k$ measurement error assumed to be white with a known covariance structure.

The covariance matrices for $\mathbf{w}_k$ and $\mathbf{v}_k$ are given by

$$E\left[\mathbf{w}_k \mathbf{w}_i^T\right] = \begin{cases} \mathbf{Q}_k, & i = k \\ 0, & i \neq k \end{cases} \qquad (5.3)$$

$$E\left[\mathbf{v}_k \mathbf{v}_i^T\right] = \begin{cases} \mathbf{C}_{l_k}, & i = k \\ 0, & i \neq k \end{cases} \qquad (5.4)$$

$$E\left[\mathbf{w}_k \mathbf{v}_i^T\right] = 0. \qquad (5.5)$$

where

$\mathbf{Q}_k$ variance matrix of process noise at t_k,

$\mathbf{C}_{l_k}$ variance matrix of measurement error at t_k.

The standard Kalman filter equations are derived as follows (Brown & Hwang 1992). The blending factor called Kalman filter gain is given by

$$\mathbf{K}_k = \mathbf{P}_k^- \mathbf{A}_k^T \left(\mathbf{A}_k \mathbf{P}_k^- \mathbf{A}_k^T + \mathbf{C}_{l_k} \right)^{-1} \tag{5.6}$$

where $\mathbf{P}_k^-$ is error covariance matrix associated with projected estimate.

The optimal estimate at t_k is obtained by linearly blending the noisy measurement $\mathbf{z}_k$, projected estimate $\hat{\mathbf{x}}_k^-$ and the filter gain $\mathbf{K}_k$

$$\hat{\mathbf{x}}_k = \hat{\mathbf{x}}_k^- + \mathbf{K}_k \left(\mathbf{z}_k - \mathbf{A}_k \hat{\mathbf{x}}_k^- \right). \tag{5.7}$$

The covariance matrix associated with the optimal estimate may be computed by

$$\mathbf{P}_k = \left(\mathbf{I} - \mathbf{K}_k \mathbf{A}_k \right) \mathbf{P}_k^- \left(\mathbf{I} - \mathbf{K}_k \mathbf{A}_k \right)^T + \mathbf{K}_k \mathbf{C}_{l_k} \mathbf{K}_k^T \tag{5.8}$$

or

$$\mathbf{P}_k = \left(\mathbf{I} - \mathbf{K}_k \mathbf{A}_k \right) \mathbf{P}_k^- \tag{5.9}$$

where the optimal gain has been substituted in. Since $\mathbf{w}_k$ in equation (5.1) has zero mean and is not correlated with any of the previous $\mathbf{w}$'s by definition, the contribution of $\mathbf{w}_k$ to the projected estimate may be ignored. Thus, the projected estimate at t_{k+1} is given by

$$\hat{\mathbf{x}}_{k+1}^- = \phi_k \hat{\mathbf{x}}_k \, . \tag{5.10}$$

The error covariance matrix associated with the projected estimate is obtained by

$$\mathbf{P}_{k+1}^- = \phi_k \mathbf{P}_k \phi_k^T + \mathbf{Q}_k \, . \tag{5.11}$$

Equations (5.6) to (5.11) constitute the Kalman filter recursive equations. The Kalman filter is an algorithm for making optimal estimates from discrete measurements.

5.2 Sensor Filters

There are many factors to consider when implementing a Kalman filter for sensors. In the most common implementation, one Kalman filter takes all measurements into account and updates all estimates at the same time. This approach is called the centralized Kalman filter (e.g. Carlson 1987 and Abousalem 1993). This is not an efficient way for this project since the sensor measurements are independent and the update intervals are not identical. For instance, the gyroscope measurement bias estimate may be updated only when the vehicle heading rate is perfectly known (e.g. heading rate should be zero when a

vehicle is not moving). Also, it is preferable to keep the size of matrices used in the filter as small as possible since a matrix inversion is required to calculate the Kalman gain. Another concern is flexibility. For instance, it is not desirable to update the gyro bias estimate when the gyro measurement is absent.

Considering these factors, an array of independent two-state Kalman filters is implemented. It consists of two measurement filters, two error correctors and a heading filter, which are developed in the following sections. The strengths of this approach are that the interval epoch may be adjusted, the system may de-activate a certain filter when it is unnecessary and the computational load is less than the centralized Kalman filter. This approach was selected as it conforms to the modular programming concept. Every software component may be transported to any other program to reduce programming and debugging time. The navigation program presented in Chapter Six uses these filters extensively.

The general dynamic model is described immediately below. If the behavior of a phenomenon to be sensed is modeled by a linear parameter system, the dynamics of such a system may be represented by the first-order equation (Gelb et al. 1974)

$$\mathbf{x}(t) = \mathbf{F}(t)\mathbf{x}(t) + \mathbf{G}(t)\mathbf{w}(t) \tag{5.12}$$

where

$\mathbf{x}(t)$ system state vector,

$\mathbf{w}(t)$ random forcing function,

$\mathbf{F}(t), \mathbf{G}(t)$ matrices arising in the formulation.

Several researchers suggest that the integrated Gauss-Markov process may be appropriate for the sensor filter models (e.g. Brown & Hwang 1992, Abbot & Powell, 1995). A general continuous model in this case is (Brown & Hwang 1992)

$$\begin{bmatrix} \dot{x} \\ \ddot{x} \end{bmatrix} = \begin{bmatrix} 0 & 1 \\ 0 & -\beta \end{bmatrix} \begin{bmatrix} x \\ \dot{x} \end{bmatrix} + \mathbf{I} \begin{bmatrix} w_1 \\ w_2 \end{bmatrix} \tag{5.13}$$

where β is time constant for the process.

For the Kalman filter, the transition matrix and the covariance matrix associated with $\mathbf{w}$ are derived using this model. The transition matrix is determined by (Brown & Hwang 1992)

$$\begin{aligned}
\phi &= \left[\mathcal{L}^{-1} \left[(s\mathbf{I} - \mathbf{F})^{-1} \right] \right]_{t=\Delta t} \\
&= \mathcal{L}^{-1} \begin{bmatrix} s & -1 \\ 0 & s+\beta \end{bmatrix}^{-1} \\
&= \mathcal{L}^{-1} \begin{bmatrix} \dfrac{1}{s} & \dfrac{1}{s(s+\beta)} \\ 0 & \dfrac{1}{s+\beta} \end{bmatrix} \\
&= \begin{bmatrix} 1 & \dfrac{1}{\beta}\left(1 - e^{-\beta \Delta t}\right) \\ 0 & e^{-\beta \Delta t} \end{bmatrix}
\end{aligned} \tag{5.14}$$

where $\mathcal{L}^{-1}$ is inverse Laplace transform operator.

Although analytical evaluation of the covariance matrix $\mathbf{Q}_k$ is not a trivial task, this is a good opportunity to derive it. Formally, $\mathbf{Q}_k$ is expressed in integral form as (Brown & Hwang 1992, Gelb et al. 1974)

$$
\begin{aligned}
\mathbf{Q}_k &= E\left[\mathbf{w}_k \mathbf{w}_k^T\right] \\
&= E\left\{\left[\int_{t_k}^{t_{k+1}} \phi(t_{k+1},\xi)\mathbf{G}(\xi)\mathbf{u}(\xi)d\xi\right]\left[\int_{t_k}^{t_{k+1}} \phi(t_{k+1},\eta)\mathbf{G}(\eta)\mathbf{u}(\eta)d\eta\right]^T\right\} \\
&= \int_{t_k}^{t_{k+1}}\int_{t_k}^{t_{k+1}} \phi(t_{k+1},\xi)\mathbf{G}(\xi)E\left[\mathbf{u}(\xi)\mathbf{u}^T(\eta)\right]\mathbf{G}^T(\eta)\phi^T(t_{k+1},\eta)d\xi d\eta
\end{aligned}
\tag{5.15}
$$

where the matrix $E\left[\mathbf{u}(\xi)\mathbf{u}^T(\eta)\right]$ is a matrix of Dirac delta functions

$$
E\left[u(\xi)u(\eta)\right] = \delta(\xi-\eta) = \begin{cases} \infty, & \xi=\eta \\ 0 & \xi\neq\eta \end{cases}
\tag{5.16}
$$

which is zero anywhere except at $\xi=\eta$. At $\xi=\eta$, it is infinite in such a way that the integral of the function across the singularity is unity (Gelb et al. 1974). An important property of the delta function, which follows from this definition, is

$$
\int_{-\infty}^{\infty} G(x)\delta(x-x_0)dx = G(x_0)
\tag{5.17}
$$

Substituting equations (5.3), (5.13), (5.14), (5.16) and (5.17) into equation (5.15) yields

$$
\begin{aligned}
\mathbf{Q}_k &= \int_{t_k}^{t_{k+1}} \int_{t_k}^{t_{k+1}} \begin{bmatrix} 1 & \frac{1}{\beta}\left(1-e^{-\beta\xi}\right) \\ 0 & e^{-\beta\xi} \end{bmatrix} \begin{bmatrix} w_1 \\ w_2 \end{bmatrix} E\left[\mathbf{u}(\xi)\mathbf{u}^T(\eta)\right] \begin{bmatrix} w_1 \\ w_2 \end{bmatrix}^T \begin{bmatrix} 1 & \frac{1}{\beta}\left(1-e^{-\beta\eta}\right) \\ 0 & e^{-\beta\eta} \end{bmatrix}^T d\xi d\eta \\[2mm]
&= \int_{t_k}^{t_{k+1}} \begin{bmatrix} 1 & \frac{1}{\beta}\left(1-e^{-\beta\xi}\right) \\ 0 & e^{-\beta\Delta\xi} \end{bmatrix} \begin{bmatrix} w_1 \\ w_2 \end{bmatrix}\begin{bmatrix} w_1 \\ w_2 \end{bmatrix}^T \begin{bmatrix} 1 & \frac{1}{\beta}\left(1-e^{-\beta\xi}\right) \\ 0 & e^{-\beta\xi} \end{bmatrix}^T d\xi \\[2mm]
&= \int_0^{\Delta t} \begin{bmatrix} 1 & \frac{1}{\beta}\left(1-e^{-\beta\xi}\right) \\ 0 & e^{-\beta\Delta\xi} \end{bmatrix} \begin{bmatrix} q_1 & 0 \\ 0 & q_2 \end{bmatrix} \begin{bmatrix} 1 & \frac{1}{\beta}\left(1-e^{-\beta\xi}\right) \\ 0 & e^{-\beta\xi} \end{bmatrix}^T d\xi \\[2mm]
&= \int_0^{\Delta t} \begin{bmatrix} \frac{1}{\beta^2}\left(q_1\beta^2 + q_2 - 2q_2 e^{-\beta\xi} + q_2 e^{-2\beta\xi}\right) & \frac{q_2}{\beta}\left(e^{-\beta\xi} - e^{-2\beta\xi}\right) \\ \frac{q_2}{\beta}\left(e^{-\beta\xi} - e^{-2\beta\xi}\right) & q_2 e^{-2\beta\xi} \end{bmatrix} d\xi.
\end{aligned}
$$

$$(5.18)$$

The integration of each element gives the final form

$$
\mathbf{Q}_k = \begin{bmatrix} Q_{11} & Q_{12} \\ Q_{21} & Q_{22} \end{bmatrix}
\tag{5.19}
$$

where

$$
\begin{aligned}
Q_{11} &= \int_0^{\Delta t} \frac{1}{\beta^2}\left(q_1\beta^2 + q_2 - 2q_2 e^{-\beta\xi} + q_2 e^{-2\beta\xi}\right) d\xi \\[2mm]
&= \frac{1}{\beta^2}\left[\left(q_1\beta^2 + q_2\right)\Delta t - 2q_2\left(-\frac{1}{\beta}\right)\left(e^{-\beta\Delta t} - 1\right) + q_2\left(-\frac{1}{2\beta}\right)\left(e^{-2\beta\Delta t} - 1\right)\right] \\[2mm]
&= -\frac{3}{2\beta^3}q_2 + \left(q_1 + \frac{q_2}{\beta^2}\right)\Delta t + \frac{2q_2}{\beta^3}e^{-\beta\Delta t} - \frac{q_2}{2\beta}e^{-2\beta\Delta t}
\end{aligned}
\tag{5.20}
$$

$$Q_{12} = \int_0^{\Delta t} \frac{q_2}{\beta} \left(e^{-\beta \xi} - e^{-2\beta \xi} \right) d\xi$$

$$= \frac{q_2}{\beta} \left\{ \left(-\frac{1}{\beta} \right) \left(e^{-\beta \Delta t} - 1 \right) - \left(-\frac{1}{2\beta} \right) \left(e^{-2\beta \Delta t} - 1 \right) \right\} \qquad (5.21)$$

$$= \frac{q_2}{\beta^2} \left(\frac{1}{2} - e^{-\beta \Delta t} + \frac{1}{2} e^{-2\beta \Delta t} \right)$$

$$Q_{22} = \int_0^{\Delta t} q_2 e^{-2\beta \xi} d\xi$$

$$= \left(-\frac{q_2}{2\beta} \right) \left(e^{-2\beta \Delta t} - 1 \right) \qquad (5.22)$$

$$= \frac{q_2}{2\beta} \left(1 - e^{-2\beta \Delta t} \right)$$

and

$$Q_{21} = Q_{12}. \qquad (5.23)$$

Note that there is an important distinction to be made between q and Q. The q is an element of the spectral density matrix and the Q is called a covariance matrix (Gelb et al. 1974). A spectral density matrix may be converted to a covariance matrix through multiplication by the Dirac delta function (Gelb et al. 1974). The relationship between the variance of the process noise σ^2, the spectral density q and the correlation time β is defined as (Bullock 1995)

$$q = 2\beta\sigma^2.$$
(5.24)

The above discussion facilitates the development of the sensor filters. All sensor filters use the integrated Gauss-Markov model of equation (5.13). The barometric height dynamic model may be expressed as

$$\begin{bmatrix} \dot{h} \\ \ddot{h} \end{bmatrix} = \begin{bmatrix} 0 & 1 \\ 0 & -\beta_h \end{bmatrix} \begin{bmatrix} h \\ \dot{h} \end{bmatrix} + \begin{bmatrix} w_{h1}(t) \\ w_{h2}(t) \end{bmatrix}.$$
(5.25)

The gyroscope heading rate model is

$$\begin{bmatrix} \dot{\omega} \\ \ddot{\omega} \end{bmatrix} = \begin{bmatrix} 0 & 1 \\ 0 & -\beta_\omega \end{bmatrix} \begin{bmatrix} \omega \\ \dot{\omega} \end{bmatrix} + \begin{bmatrix} w_{\omega1}(t) \\ w_{\omega2}(t) \end{bmatrix}.$$
(5.26)

The barometric height bias model is

$$\begin{bmatrix} \delta\dot{h} \\ \delta\ddot{h} \end{bmatrix} = \begin{bmatrix} 0 & 1 \\ 0 & -\beta_{dh} \end{bmatrix} \begin{bmatrix} \delta h \\ \delta\dot{h} \end{bmatrix} + \begin{bmatrix} w_{\delta h1}(t) \\ w_{\delta h2}(t) \end{bmatrix}.$$
(5.27)

The gyroscope heading rate bias model is

$$\begin{bmatrix} \delta\dot{\omega} \\ \delta\ddot{\omega} \end{bmatrix} = \begin{bmatrix} 0 & 1 \\ 0 & -\beta_{\delta\omega} \end{bmatrix} \begin{bmatrix} \delta\omega \\ \delta\dot{\omega} \end{bmatrix} + \begin{bmatrix} w_{\delta\omega1}(t) \\ w_{\delta\omega2}(t) \end{bmatrix}. \qquad (5.28)$$

Finally, the sensor heading model is

$$\begin{bmatrix} \dot{\Theta} \\ \ddot{\Theta} \end{bmatrix} = \begin{bmatrix} 0 & 1 \\ 0 & -\beta_{\Theta} \end{bmatrix} \begin{bmatrix} \Theta \\ \dot{\Theta} \end{bmatrix} + \begin{bmatrix} w_{\Theta1}(t) \\ w_{\Theta2}(t) \end{bmatrix} \qquad (5.29)$$

where β is the time correlation constant for the corresponding sensor input.

Note that although equations (5.25) to (5.29) are of the same form, an appropriate time constant and white noise variance must be determined for each model taking into account the measurement characteristics, operation environment, and so on. For this thesis, these parameters were selected and listed in Chapter Seven. The significance of these filters is that the system accepts a wide range of sensors with various accuracies. Adjustment to a new sensor may be done by choosing a proper β and q. The determination of β and q is based on laboratory experiments and specifications provided by the manufacturer. Corresponding transition matrices and noise covariance matrices may be evaluated using equations (5.14) and (5.19), or by less demanding numerical evaluations based on approximations (Brown & Hwang 1992). For this thesis, these parameters were selected and listed in Chapter Seven.

5.3 Kalman Position Estimator with Sensor Constraint

Designing a Kalman filter with sensor constraints involves the filter dimension, the determination of a proper mathematical model and implementation of the sensor constraint strategy. In many land vehicular applications, a constant velocity model is often chosen since the introduction of the acceleration state does not significantly improve positioning accuracy for moderate vehicle dynamics (e.g. Cannon 1991, Gao 1992, Bullock 1995). The estimate state consists of eight parameters

$$\mathbf{x} = \left\{ \delta\phi \quad \delta\dot{\phi} \quad \delta\lambda \quad \delta\dot{\lambda} \quad \delta h \quad \delta\dot{h} \quad c\delta t \quad c\delta\dot{t} \right\}^{T} \tag{5.30}$$

where

$\delta\phi, \delta\dot{\phi}$ latitude position and rate errors,

$\delta\lambda, \delta\dot{\lambda}$ longitude position and rate errors,

$\delta h, \delta\dot{h}$ height position and rate errors,

$c\delta t, c\delta\dot{t}$ receiver clock offset and drift errors.

An integrated Gauss-Markov model is used as the sensor filter model. The dynamic model of the position estimate may be described by

$$\dot{\mathbf{x}} = \begin{bmatrix} 0 & 1 & 0 & 0 & 0 & 0 & 0 & 0 \\ 0 & -\beta_\phi & 0 & 0 & 0 & 0 & 0 & 0 \\ 0 & 0 & 0 & 1 & 0 & 0 & 0 & 0 \\ 0 & 0 & 0 & -\beta_\lambda & 0 & 0 & 0 & 0 \\ 0 & 0 & 0 & 0 & 0 & 1 & 0 & 0 \\ 0 & 0 & 0 & 0 & 0 & -\beta_h & 0 & 0 \\ 0 & 0 & 0 & 0 & 0 & 0 & 0 & 1 \\ 0 & 0 & 0 & 0 & 0 & 0 & 0 & -\beta_{cdt} \end{bmatrix} \mathbf{x} + \begin{bmatrix} w_\phi(t) \\ w_{\dot{\phi}}(t) \\ w_\lambda(t) \\ w_{\dot{\lambda}}(t) \\ w_h(t) \\ w_{\dot{h}}(t) \\ w_{cdt}(t) \\ w_{cdi}(t) \end{bmatrix} \qquad (5.31)$$

where

β_ϕ time correlation constant of latitude estimate,

β_λ time correlation constant of longitude estimate,

β_h time correlation constant of height estimate,

β_{cdt} time correlation constant of receiver clock offset estimate,

$w_\phi(t), w_{\dot{\phi}}(t)$ white noise input of latitude position and rate errors,

$w_\lambda(t), w_{\dot{\lambda}}(t)$ white noise input of longitude position and rate errors,

$w_h(t), w_{\dot{h}}(t)$ white noise input of height position and rate errors,

$w_{cdt}(t), w_{cdi}(t)$ white noise input of receiver clock offset and drift errors.

The state transition matrix of this model is derived as

$$\phi_k = \left[\mathcal{L}^{-1}\left[(s\mathbf{I} - \mathbf{F})^{-1} \right] \right]_{t=\Delta t}$$

$$= \begin{bmatrix} 1 & \frac{1}{\beta_\phi}\left(1 - e^{-\beta_\phi \Delta t}\right) & 0 & 0 & 0 & 0 & 0 & 0 \\ 0 & e^{-\beta_\phi \Delta t} & 0 & 0 & 0 & 0 & 0 & 0 \\ 0 & 0 & 1 & \frac{1}{\beta_\lambda}\left(1 - e^{-\beta_\lambda \Delta t}\right) & 0 & 0 & 0 & 0 \\ 0 & 0 & 0 & e^{-\beta_\lambda \Delta t} & 0 & 0 & 0 & 0 \\ 0 & 0 & 0 & 0 & 1 & \frac{1}{\beta_h}\left(1 - e^{-\beta_h \Delta t}\right) & 0 & 0 \\ 0 & 0 & 0 & 0 & 0 & e^{-\beta_h \Delta t} & 0 & 0 \\ 0 & 0 & 0 & 0 & 0 & 0 & 1 & \frac{1}{\beta_{cdt}}\left(1 - e^{-\beta_{cdt} \Delta t}\right) \\ 0 & 0 & 0 & 0 & 0 & 0 & 0 & e^{-\beta_{cdt} \Delta t} \end{bmatrix}$$

$$(5.32)$$

The corresponding process noise covariance matrix may be obtained from equations (5.15) and (5.32) as

$$\mathbf{Q}_k = \begin{bmatrix} Q_{11} & Q_{12} & 0 & 0 & 0 & 0 & 0 & 0 \\ Q_{21} & Q_{22} & 0 & 0 & 0 & 0 & 0 & 0 \\ 0 & 0 & Q_{33} & Q_{34} & 0 & 0 & 0 & 0 \\ 0 & 0 & Q_{43} & Q_{44} & 0 & 0 & 0 & 0 \\ 0 & 0 & 0 & 0 & Q_{55} & Q_{56} & 0 & 0 \\ 0 & 0 & 0 & 0 & Q_{65} & Q_{66} & 0 & 0 \\ 0 & 0 & 0 & 0 & 0 & 0 & Q_{77} & Q_{78} \\ 0 & 0 & 0 & 0 & 0 & 0 & Q_{87} & Q_{88} \end{bmatrix}$$

$$(5.33)$$

where

$$Q_{11} = -\frac{3}{2\beta_\phi^3}q_{\dot\phi} + \left(q_\phi + \frac{q_{\dot\phi}}{\beta_\phi^2}\right)\Delta t + \frac{2q_{\dot\phi}}{\beta_\phi^3}e^{-\beta_\phi\Delta t} - \frac{q_{\dot\phi}}{2\beta_\phi}e^{-2\beta_\phi\Delta t}, \tag{5.34}$$

$$Q_{12} = \frac{q_{\dot\phi}}{\beta_\phi^2}\left(\frac{1}{2} - e^{-\beta_\phi\Delta t} + \frac{1}{2}e^{-2\beta_\phi\Delta t}\right), \tag{5.35}$$

$$Q_{21} = Q_{12}, \tag{5.36}$$

$$Q_{22} = \frac{q_{\dot\phi}}{2\beta_\phi}\left(1 - e^{-2\beta_\phi\Delta t}\right), \tag{5.37}$$

$$Q_{33} = -\frac{3}{2\beta_\lambda^3}q_{\dot\lambda} + \left(q_\lambda + \frac{q_{\dot\lambda}}{\beta_\lambda^2}\right)\Delta t + \frac{2q_{\dot\lambda}}{\beta_\lambda^3}e^{-\beta_\lambda\Delta t} - \frac{q_{\dot\lambda}}{2\beta_\lambda}e^{-2\beta_\lambda\Delta t}, \tag{5.38}$$

$$Q_{34} = \frac{q_{\dot\lambda}}{\beta_\lambda^2}\left(\frac{1}{2} - e^{-\beta_\lambda\Delta t} + \frac{1}{2}e^{-2\beta_\lambda\Delta t}\right), \tag{5.39}$$

$$Q_{43} = Q_{34}, \tag{5.40}$$

$$Q_{44} = \frac{q_{\dot\lambda}}{2\beta_\lambda}\left(1 - e^{-2\beta_\lambda\Delta t}\right), \tag{5.41}$$

$$Q_{55} = -\frac{3}{2\beta_h^3}q_{\dot h} + \left(q_h + \frac{q_{\dot h}}{\beta_h^2}\right)\Delta t + \frac{2q_{\dot h}}{\beta_h^3}e^{-\beta_h\Delta t} - \frac{q_{\dot h}}{2\beta_h}e^{-2\beta_h\Delta t}, \tag{5.42}$$

$$Q_{56} = \frac{q_{\dot h}}{\beta_h^2}\left(\frac{1}{2} - e^{-\beta_h\Delta t} + \frac{1}{2}e^{-2\beta_h\Delta t}\right), \tag{5.43}$$

$$Q_{65} = Q_{56}, \tag{5.44}$$

$$Q_{66} = \frac{q_{\dot h}}{2\beta_h}\left(1 - e^{-2\beta_h\Delta t}\right), \tag{5.45}$$

$$Q_{77} = -\frac{3}{2\beta_{cdt}^3}q_{cdi} + \left(q_{cdt} + \frac{q_{cdi}}{\beta_{cdt}^2}\right)\Delta t + \frac{2q_{cdi}}{\beta_{cdt}^3}e^{-\beta_{cdt}\Delta t} - \frac{q_{cdi}}{2\beta_{cdt}}e^{-2\beta_{cdt}\Delta t}, \tag{5.46}$$

$$Q_{78} = \frac{q_{cdt}}{\beta_{cdt}^2}\left(\frac{1}{2} - e^{-\beta_{cdt}\Delta t} + \frac{1}{2}e^{-2\beta_{cdt}\Delta t}\right),$$ (5.47)

$$Q_{87} = Q_{78},$$ (5.48)

and

$$Q_{88} = \frac{q_{cdt}}{2\beta_{cdt}}\left(1 - e^{-2\beta_{cdt}\Delta t}\right),$$ (5.49)

where

$q_\phi, q_{\dot\phi}$	spectral density of latitude position and rate errors,
$q_\lambda, q_{\dot\lambda}$	spectral density of longitude position and rate errors,
$q_h, q_{\dot h}$	spectral density of height position and rate errors,
$q_{cdt}, q_{c\dot dt}$	spectral density of receiver clock offset and drift errors.

Determination of spectral densities for the position random process is at best a "guesstimate" roughly based on expected vehicle dynamics (Brown & Hwang 1992). In many vehicular applications, the random perturbations to the intended path are greater in the horizontal plane than in the vertical.

The same augmented design matrix shown in equations (4.7) to (4.9) is used in the Kalman position estimator to implement the sensor constraint. The Kalman filter sensor constraint algorithm is identical to that of the least squares estimator, the effectiveness of the constraint is controlled by the measurement variance matrix. The Kalman filter position estimates tend to oscillate after a tight turn of the vehicle because of the presence of the velocity state. This is not desirable for sensor constraint positioning since the initial

heading is determined by previous position estimates. Thus, it may introduce a significant initial heading bias into the Kalman position estimator and cause a filter to breakdown. An adaptive process noise covariance matrix routine was thus created to avoid such oscillation. This routine takes the gyroscope heading change into account in order to increase the process noise of the horizontal plane components as

$$\hat{Q} = Q \cdot e^{k|\omega|} \qquad\qquad (5.50)$$

where

$\hat{Q}$	adapted process noise covariance,
Q	initial process noise covariance,
k	adaptation gain constant,
ω	gyroscope heading change [rad].

The adapted value is exponentially proportional to the initial value and is a function of the heading change. An appropriate adaptation gain constant must be selected to avoid possible filter breakdown for any given heading change. For this thesis, adaptation gain of 10.0 was selected. This value yields $k|\omega| = 1.0$ when ω is approximately 5.7 [deg/s].

CHAPTER SIX

SOFTWARE AND IMPLEMENTATION CONSIDERATIONS

This chapter describes the navigation software algorithm. The program, called EC3, is based on C^{3}NAV^{TM}, developed at The University of Calgary (Cannon & Lachapelle 1992). C^{3}NAV^{TM} is a between-receiver, single difference, carrier phase smoothed code DGPS navigation program. EC3 uses the basic components of C^{3}NAV^{TM} such as satellite ephemeris decoding, satellite orbit computation, satellite clock computation, ionospheric and tropospheric corrections, generating or applying differential corrections, carrier smoothed code generation and standard least squares estimation. New modules were developed to accommodate sensor constraint positioning. EC3 is written in C language. The chapter concludes with discussions of sensor constraint position estimators and operational considerations.

6.1 Overview

Figure 6.1 shows an overview of the navigation program. Basic flow is identical to that of C^{3}NAV^{TM} (Cannon & Lachapelle 1992). There are, however, a number of enhancements for sensor constraint positioning. The barometer and/or gyro data for the vertical and horizontal constraint may be applied to solutions. EC3 has two position estimators, the least squares and Kalman filter, and a user can select one of these estimator for computations. Utilizing this feature enables to compare least squares solutions to Kalman filter ones. The barometer and gyro measurement data reader obtains the

corresponding sensor data of the current GPS time for each epoch. These raw measurements are sent to the sensor constraint positioning module with corrected GPS observations, satellite coordinates and initial receiver coordinates. The positioning module returns a value to flag the success or failure of the position estimate process. Upon success, the receiver coordinates are updated, displayed and stored. Filtering of the sensor measurements is done in the sensor constraint positioning module and is therefore not seen at this level.

```
                        ┌──────────────────┐
                        │  Read Option File │
                        └──────────────────┘
                                 │
                        ┌──────────────────┐
                        │  Read Ephemeris   │
                        │       File        │
                        └──────────────────┘
                                 │
                        ┌──────────────────┐
                        │    Read GPS,      │
                        │    Barometer      │
                        │   and/or Gyro     │◄────────────┐
                        │   Measurement     │             │
                        │      Data         │             │
                        └──────────────────┘             │
                                 │                         │
                      Yes      ◇ Differential              │
              ┌──────────────── Processing? ◇              │
              │                    │ No                    │
   ┌──────────────────┐            │                       │
   │ Get Differential │            │                       │
   │   Corrections    │            │                       │
   └──────────────────┘            │                       │
              │         ┌──────────────────────────────┐   │
              │         │ Compute Satellite Coordinates │   │
              └────────►│ Compute and Apply Satellite Clock, │
                        │ Troposphere and Ionosphere Correction │
                        │ Compute Carrier Phase Smoothed Range │
                        │ Reject Satellites Under Cutoff Angle │
                        └──────────────────────────────┘   │
                                 │                          │
                        ┌──────────────────┐               │
                        │ Compute Position Estimates │      │
                        │ - Least Squares or Kalman  │      │
                        │ - Standard or Sensor       │      │
                        │   Constraint               │      │
                        └──────────────────┘               │
                                 │                          │
                              ◇ Get Estimates? ◇───No───────┤
                                 │ Yes                      │
                              ◇ Compute                     │
                               Differential ◇──Yes──┐       │
                               Corrections?         │       │
                                 │ No     ┌──────────────────┐
                                 │        │ Compute and Store│
                                 │        │   Corrections    │
                                 │        └──────────────────┘
                        ┌──────────────────┐               │
                        │  Output Results   │───────────────┘
                        └──────────────────┘
```

Figure 6.1 Flowchart of EC3

6.2 Sensor Constraint Positioning Module

Flowcharts for the sensor constraint positioning module are shown in Figure 6.2 (least squares) and Figure 6.3 (Kalman). Although they appear identical, fault tolerant routines are implemented in the Kalman position estimator as explained later in this chapter. Kalman sensor measurement filters are first used to obtain filtered sensor measurements. A "standard" DGPS position estimator, without sensor constraint, first tries to find a solution without the aid of sensor constraints. The routine evaluates the result and immediately decides whether sensor constraint positioning should be used or not. The current criteria for acceptable position estimates are (1) the range residuals and (2) satellite geometry expressed by the dilution of precision (DOP). In this thesis, these values are taken to achieve the best result. These values used for computation are explicitly written in Chapter Seven in which testing results are presented.

If a position estimate without sensor constraints is acceptable, the routine tries to update sensor measurement errors and heading. First, it initiates the Kalman barometric height error corrector using an updated GPS height. Then, the Kalman gyro error corrector is activated if the receiver is stationary, i.e. the reference heading change is zero. Finally, it determines an estimated maximum GPS heading error with respect to the velocity of the vehicle as

$$\varepsilon_{\Theta_{GPS}} = \sin^{-1}\left(\frac{\varepsilon_{p_{GPS},k} + \varepsilon_{p_{GPS},k-1}}{v_k}\right) \qquad (6.1)$$
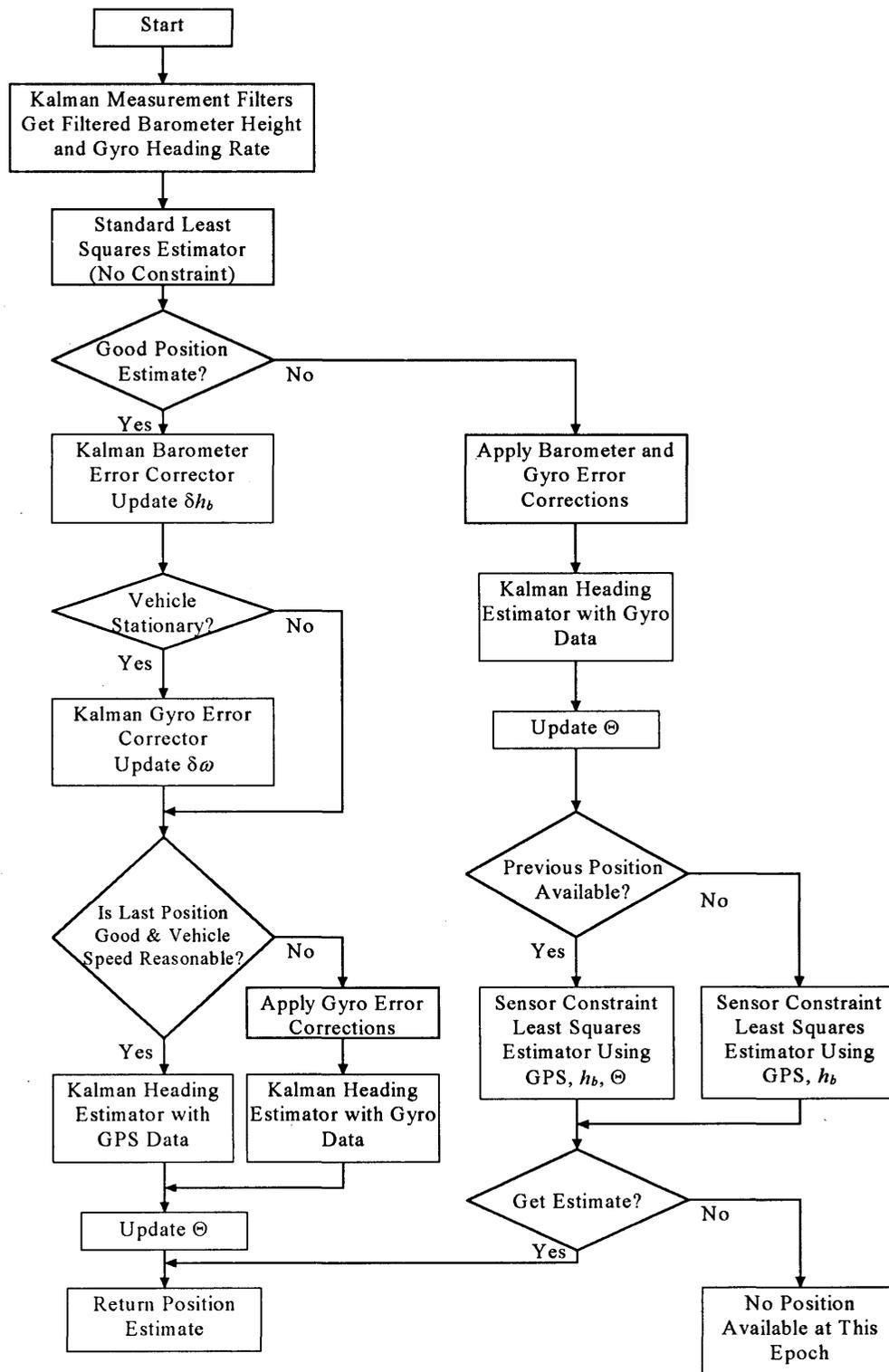
Figure 6.2 Flowchart of Sensor Constraint Least Squares Position Estimator

```
                    ┌──────────┐
                    │  Start   │
                    └──────────┘
                         │
                         ▼
        ┌──────────────────────────────┐
        │  Kalman Measurement Filters    │
        │  Get Filtered Barometer Height │
        │  and Gyro Heading Rate         │
        └──────────────────────────────┘
                         │
                         ▼
            ┌──────────────────┐
            │ Standard Kalman   │
            │ Position Estimator│
            │ (No Constraint)   │
            └──────────────────┘
                    │
                    ▼
              ◇ Good Position ◇──── No ────────┐
               ◇ Estimate? ◇                   │
                    │ Yes                       │
                    ▼                           ▼
        ┌──────────────────┐        ┌──────────────────┐
        │ Kalman Barometer  │        │ Apply Barometer   │
        │ Error Corrector   │        │ and Gyro Error    │
        │ Update δh_b       │        │ Corrections       │
        └──────────────────┘        └──────────────────┘
                    │                           │
                    ▼                           ▼
              ◇ Vehicle ◇── No ──┐   ┌──────────────────┐
              ◇Stationary?◇      │   │ Kalman Heading    │
                    │ Yes        │   │ Estimator with Gyro│
                    ▼            │   │ Data              │
        ┌──────────────────┐    │   └──────────────────┘
        │ Kalman Gyro Error │    │            │
        │ Corrector         │    │            ▼
        │ Update δω         │    │      ┌───────────┐
        └──────────────────┘    │      │ Update Θ  │
                    │            │      └───────────┘
                    ▼            │            │
            ◇ Is Last Position ◇ │            ▼
            ◇ Good & Vehicle  ◇─ No ◇ Previous Position ◇── No ──┐
            ◇Speed Reasonable?◇      ◇   Available?    ◇          │
                │ Yes    │           │ Yes                        │
                │        ▼           │                            │
                │  ┌──────────────┐  │                            │
                │  │ Apply Gyro   │  │                            │
                │  │ Error        │  │                            │
                │  │ Corrections  │  │                            │
                │  └──────────────┘  │                            │
                ▼        ▼           ▼                            ▼
        ┌──────────┐ ┌──────────┐ ┌──────────────┐ ┌──────────────┐
        │Kalman    │ │Kalman    │ │Sensor        │ │Sensor        │
        │Heading   │ │Heading   │ │Constraint    │ │Constraint    │
        │Estimator │ │Estimator │ │Kalman Position│ │Kalman Position│
        │with GPS  │ │with Gyro │ │Estimator Using│ │Estimator Using│
        │Data      │ │Data      │ │GPS, h_b, Θ   │ │GPS, h_b      │
        └──────────┘ └──────────┘ └──────────────┘ └──────────────┘
                │                        │                 │
                ▼                        ▼                 │
        ┌───────────┐              ◇ Get Estimate? ◇── No ─┤
        │ Update Θ  │              ◇              ◇        │
        └───────────┘                   │ Yes             │
                │                        │                 ▼
                ▼                        │     ┌──────────────────┐
        ┌──────────────┐                 │     │ No Position      │
        │ Return       │◄────────────────┘     │ Available at This│
        │ Position     │                       │ Epoch            │
        │ Estimate     │                       └──────────────────┘
        └──────────────┘
```

Figure 6.3 Flowchart of Sensor Constraint Kalman Position Estimator

where

$\varepsilon_{p_{GPS},k}, \varepsilon_{p_{GPS},k-1}$ GPS position error at t_k and t_{k-1},

v_k vehicle velocity at t_k.

This error is inversely proportional to the vehicle velocity. Therefore, a reasonable vehicle velocity yields an acceptable GPS heading. If the error is below a predetermined threshold, GPS data is used to update the heading as

$$\Theta_k = \tan^{-1}\left(\frac{\lambda_k - \lambda_{k-1}}{\phi_k - \phi_{k-1}}\right) \tag{6.2}$$

where

ϕ_k, ϕ_{k-1} latitude position estimate at t_k and t_{k-1},

λ_k, λ_{k-1} longitude position estimate at t_k and t_{k-1}.

Otherwise, the latest gyro heading change, which is filtered and corrected at an earlier stage, is appended to the last heading

$$\Theta_k = \Theta_{k-1} + \omega_k. \tag{6.3}$$

The heading is then filtered by the Kalman heading estimator with appropriate parameters.

The algorithm constantly monitors the GPS solution whether it is error-free or not. The error may be exposed as excessively large range residuals, intolerably high dilution of precision (DOP) e.g. GDOP of over 10, large position change, or lack of solution due to insufficient GPS range observations. If the position estimate, without sensor constraints, is not acceptable, the routine initiates necessary procedures to perform sensor constraint positioning. First, it updates the heading with a gyro heading change measurement. Next, if a barometer measurement is available, the barometric height constraint is activated and its error is calculated from equation (3.17). The routine then determines if a previous position is available to construct the heading row of the design matrix of equation (4.9). If this is the case, the heading constraint is applied and its error computed from equation (3.19). The augmented position estimator then computes a sensor constraint position estimate. The result is evaluated and, if acceptable, returned.

The result is considered unacceptable when no estimate is given due to (1) insufficient number of measurements or (2) divergence (least squares only). Condition (1) will be due to a shortage of GPS measurements. Note that with height and heading constraints activated, there is still a minimum requirement of two GPS measurements for computation. With only one constraint, three or more satellites are needed to complete the calculation. Condition (2) may be caused by corrupted GPS ranges, failure to correct GPS ranges, a poor initial position estimate, weak satellite geometry, inaccurate barometric height and/or heading measurements, sensor error(s) and/or heading determination failure or linear approximation errors.

6.3 Miscellaneous Considerations

6.3.1 Position Estimator Breakdown Problem

Since the standard Kalman estimator cannot diverge, there is a real possibility of poor estimate if some measurements are intolerably erratic. The least squares and Kalman estimators may give very inaccurate estimates when the quality of sensor constraint information is poor. For the Kalman position estimator, a least squares estimator is used to get the a priori estimate if (1) no *a priori* estimate is available, (2) the *a priori* estimate is exceedingly inaccurate or (3) the filter update interval is too long, i.e. no estimate is obtained for a long time. This feature helps the Kalman position estimator to recover quickly.

6.3.2 Operational Considerations

Static positioning of several minutes under an open sky is used in the prototype system to obtain the initial barometer and gyro measurement errors. It also gives the GPS receiver time to adjust its internal receiver clock to GPS time. Since a gyro senses the rotation of the unit, there is a need to determine the initial heading before a heading constraint is applied. If the system is permanently attached to the vehicle, the last heading may be stored, thus eliminating the need for redetermining an initial heading each time. However, this concept is not valid for this project since portability is of primary concern. It is therefore preferred for this system to begin operation at a location where a large number of satellites are visible and to then drive into an urban area.

6.3.3 Real-Time Implementation

A real-time operation was not implemented for this project due to the complexity of obtaining differential GPS corrections in urban areas. However, it would not be difficult to modify the system for real-time operation. In land navigation applications, it is common to update the position every second. With the current configuration, which includes five two-state and one eight-state Kalman filters, the process time is approximately five epochs per second using a 486DX-100MHz IBM compatible computer. It takes less than 0.1 seconds to obtain GPS, barometer and gyro data using a 386-20MHz IBM compatible computer. The latency of DGPS corrections and transmitting time should be also considered, however, the operation of real-time system at 1 Hz may be feasible if 486DX-100MHz or faster computer is employed.

### 6.3.4 Optimal Estimator Configuration

The system presented herein currently employs sensor information only when either GPS-only position estimate is not accurate or GPS ranges are not sufficient to compute a solution. Such system is considered sub-optimal. This approach was taken in this thesis in order to distinguish various sensor errors with GPS ones and to minimize the position error induced by the sensor measurements. The system is considered theoretically optimal when all observations are used for solutions at all times.

However, the arising problem of the optimal system is that if sensor measurements are not as accurate as expected, they may deteriorate the position accuracy. Shown in

Figure 6.4 are the position errors induced by the poor heading information during the non-constraint positioning period. Position errors of the optimal system are much higher than those of the sub-optimal (current) system. As smaller weight (larger standard deviation) is given to the heading measurement, the solutions become closer to ones of the current system. Then, if good heading can be obtained during the non-constraint period, position errors of the optimal system become considerably small as shown in Figure 6.5. Thus, it is critical for an optimal system to determine the weight of sensor measurement during the constraint-free period. Current error models are designed for the short-term constraint positioning. They are based on the linear drift approximation and they cannot be used for an extended period, e.g. longer than five minutes. Error models of higher order may be needed for an optimal system.
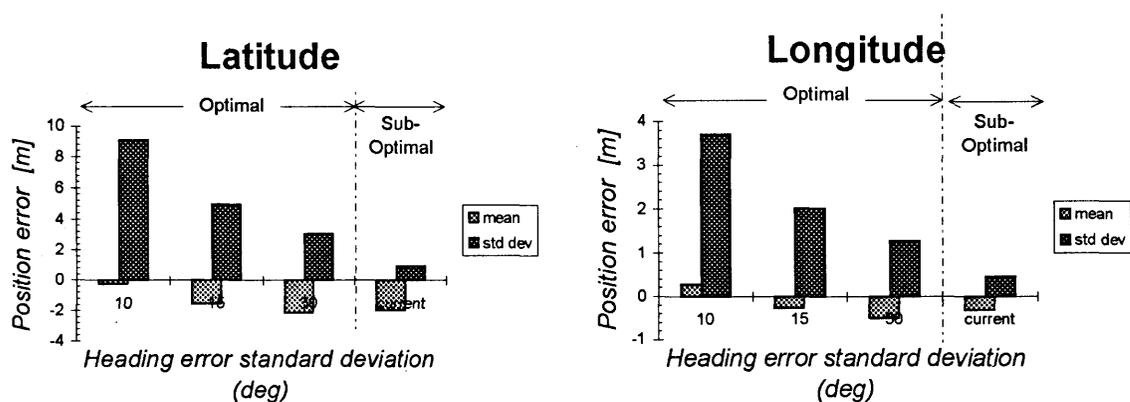
Figure 6.4. Position Error of Optimal Estimator with Poor Initial Heading
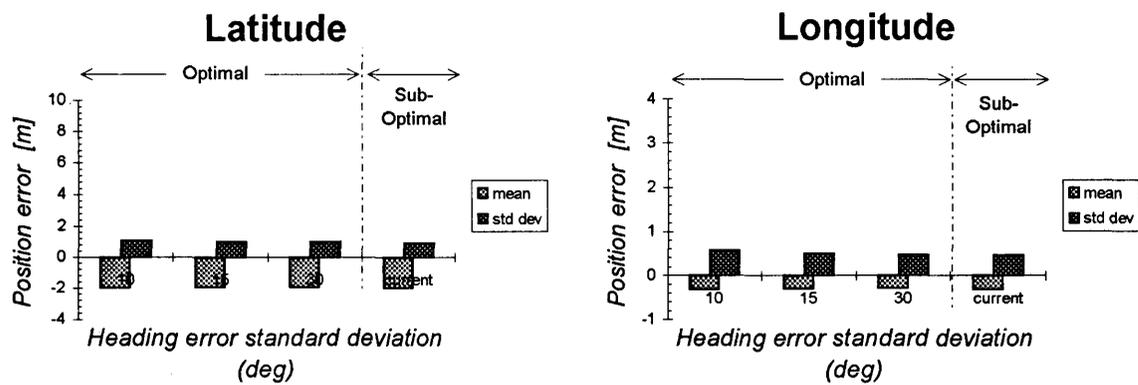
Figure 6.5. Position Error of Optimal Estimator with Good Initial Heading

CHAPTER SEVEN

SYSTEM TESTING AND RESULTS

The sensor constraint portable GPS vehicle navigation system has been developed in previous chapters. The purpose of this chapter is to evaluate its performance. Generally, estimates from the new system could be compared with certain "reference" estimates given by a performance-proven precise navigation program. If the system could be operated in an ideal environment, free from multipath and with excellent satellite coverage and geometry, we would be able to obtain a precise 3D reference trajectory using a DGPS navigation program such as FLYKIN^{TM} (Lachapelle et al. 1996). However, this assumption does not hold in urban environments where ideal signal reception is not obtained.

Two DGPS field tests were carried out for system evaluation. The first was at Springbank, Alberta, on June 29, 1996, in order to obtain clean, strong and sufficient GPS signal coverage. The reference trajectory was computed and an urban environment simulated by rejecting satellites below a certain cutoff angle. The second was in downtown Calgary, Alberta, on August 17, 1996. Numerous buildings and skywalks prevented the GPS receiver from enjoying an optimal GPS coverage.

The data was processed in several manners. For this project, the unaided and barometric height constraint least squares solutions are first presented. Then sensor constraint estimators (least squares and Kalman) are used to assess the improvement in terms of position accuracy and availability.

7.1 Urban Environment Simulation

7.1.1 Route Description and Reference Trajectory

The first field test was carried out at Springbank, Alberta on June 29, 1996. The system, described in Chapter Two, was mounted in a 1996 Ford Thunderbird. The reference station was located at control point 661-24.2. The test route is shown in Figure 7.1. The route was run in a direction as indicated by arrows in Figure 7.1. Data was collected every second. The location is very good for GPS positioning since there are few obstructions along the test route. Most of the test route was in farmland except near Calaway Park, where trees covered a portion of the sky. Sections A and B are marked in Figure 7.1 to indicate sections magnified in later position plots. The number of visible satellites and DOPs are shown in Table 7.1 and Figure 7.2.
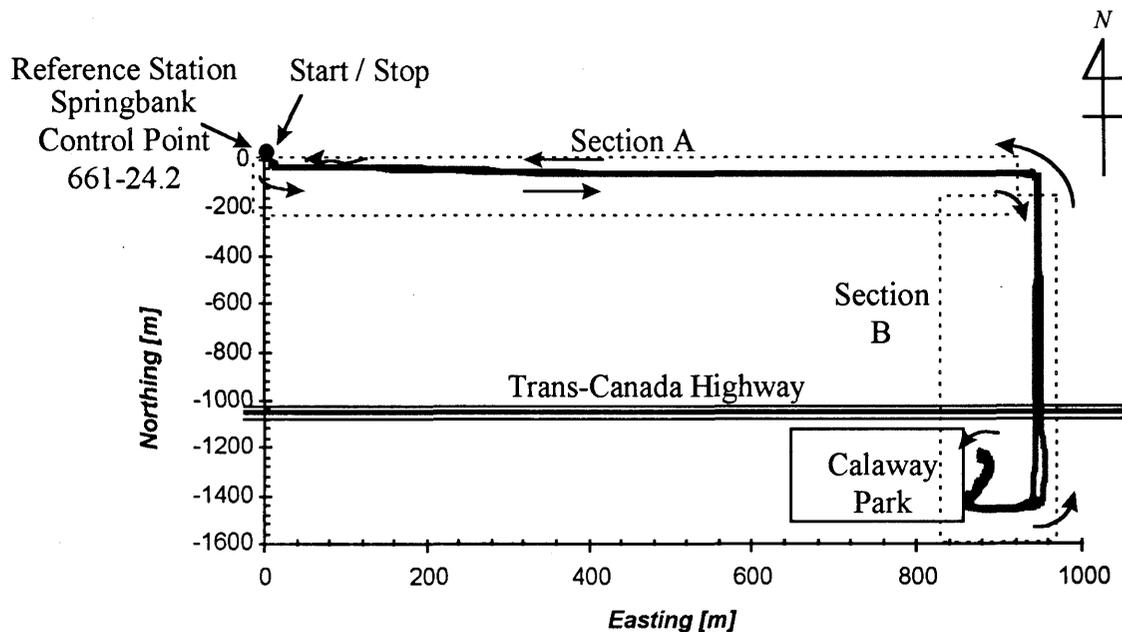

Figure 7.1 Test Route for Simulation

Table 7.1. Satellite Coverage and DOP, Springbank, June 29, 1996

Total Epochs	# of Satellites	GDOP	NDOP	EDOP	VDOP
356 (1-sec intervals)	5-8	1.7-5.8	0.7-2.3	0.6-1.4	1.3-4.1
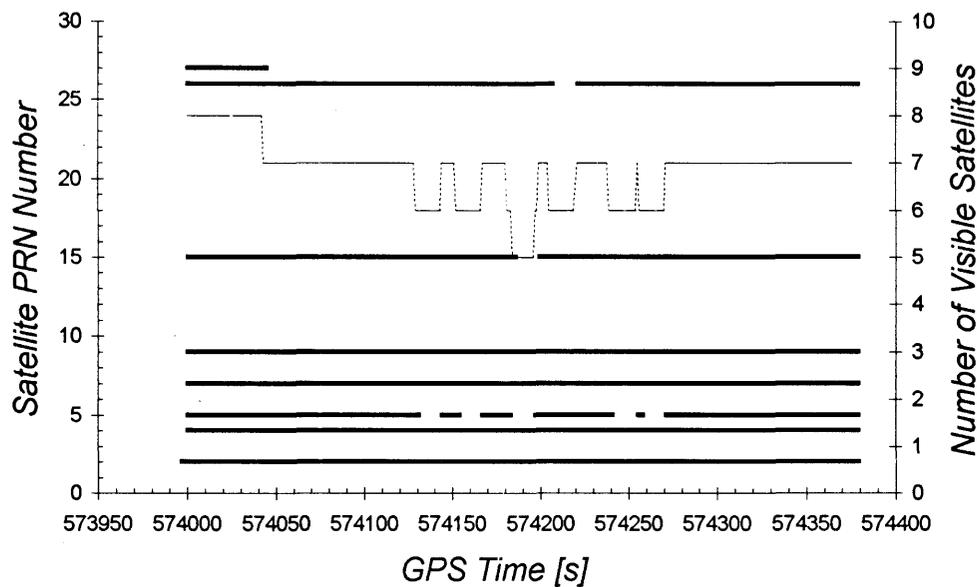
Figure 7.2. Visible Satellites, Springbank, June 29, 1996

The reference trajectory was obtained using two NovAtel GPSCard™ 951R receivers with FLYKIN™ double difference, carrier phase, float ambiguity solutions (Lachapelle et al. 1996). With these receivers, the accuracy of the position estimate given by this program is known to be decimetre level, whereas C^3NAV^{TM} gives an estimate accuracy at the metre level with carrier phase smoothed range observations (Cannon & Lachapelle 1992). Therefore, the disagreement between these two solutions, in an ideal environment, should not exceed several metres. FLYKIN™ and C^3NAV^{TM} solutions were

Table 7.2. Position Estimate Difference between SEMIKIN™ and C³NAV™ Solutions, Springbank, June 29, 1996

	Latitude	Longitude	Height
Mean [m]	-1.68	0.09	-0.57
Standard Deviation [m]	0.19	0.14	0.21
Max. Difference [m]	-2.39	-0.60	-1.35
Min. Difference [m]	-1.41	0.00	-0.18

compared to validate this assumption. The results are shown in Table 7.2. The double difference float ambiguity solution was employed for FLYKIN™ and the single difference carrier phase smoothed code solution chosen for C³NAV™. A mean bias of 1.67 m in the latitude component is observed. However, the standard deviation of the position differences is 19 to 21cm. Since the desired accuracy of the sensor constraint positioning system is 10 metres DRMS, the reference trajectory obtained with FLYKIN™ is accurate enough to determine the accuracy of the system. For instance, standard deviations of approximately 7 metres in latitude and longitude would yield a DRMS error of 10 metres.

Parameters used for computations are listed in Table 7.3 (error models) and Tables 7.4 to 7.6 (Kalman filters). Equations (4.12) to (4.15) are used to compute GPS measurement variances. Equations (3.19) and (4.16) are used for barometric height measurement variances. Equations (3.20), (3.21) and (4.17) are used for gyro heading measurement variances. These measurement variances are employed in the augmented position estimator to obtain constrained solutions. The same set of parameters are used for both simulations and downtown testing. These values are selected such that the solutions from the Kalman estimator are comparable to those from the least squares. Thus, solutions

Table 7.3. Parameters Used in Error Models

Barometric height offset error ε_b	m	1.0
Barometric height drift rate $\dot{\varepsilon}_b$	m/s	0.01667
Gyro heading rate offset error ε_g	rad/s	0.05
Gyro drift error $\dot{\varepsilon}_g$	rad/s^2	0.01
Initial heading error ε_Θ	rad	$\tan^{-1}(1.0 / v)$ where v is velocity of the vehicle
GPS code measurement error $\sigma_{\varepsilon_{range}}$	m	2.0
GPS carrier phase measurement error $\sigma_{\varepsilon_{phase}}$	m	0.02
GPS ephemeris error $\sigma_{\delta\rho} + \sigma_{\delta dt}$	m	6.0

Table 7.4. Parameters Used in Kalman Position Estimator

Description		Latitude	Longitude	Height	Clock offset
Time correlation β	1/s	1.0	1.0	1.0	1.0
Spectral density, position q	m^2/s	400.0	400.0	400.0	400.0
Spectral density, rate q	m^2/s^3	100.0	100.0	4.0	4.0

from both estimators should be similar unless other factor alter one's solutions from another.

**Table 7.5. Parameters Used in Kalman Barometer Measurement
and Correction Filters**

Description		Barometer measurement	Barometer correction
Time correlation β	1/s	1/5	1/30
Spectral density q	m^2/s^3	1.0	1.0
Measurement error r	m	1.0	1.0

**Table 7.6. Parameters Used in Kalman Gyro Measurement,
Correction and Heading Filters**

Description		Gyro measurement	Gyro correction	Heading
Time correlation β	1/s	1.0	1.0	1/3
Spectral density q	rad^2/s^3	25.0	1.0	9.0
Measurement error r	rad	1.0	0.5	1.0

7.1.2 Virtual Wall Concept

A conventional satellite rejection routine sets one single cutoff angle and rejects all satellites below this cutoff angle. Such a satellite rejection routine does not ideally simulate an urban environment. In an urban environment, weak satellite geometry is frequently observed in terms of the cross-track satellite geometry, the direction perpendicular to the vehicle trajectory. The virtual wall concept is introduced in this project. This routine computes a cutoff angle based on simulated obstructions along the street, parallel to the vehicle trajectory. Figure 7.3 illustrates the virtual wall concept.

Figure 7.3. Virtual Wall Concept

Given a cross-track cutoff angle α_{CT}, the relation between the distance to the walls perpendicular to the trajectory d_{CT} and the height of the walls h is

$$\tan(\alpha_{CT}) = \frac{h}{d_{CT}}.$$

(7.1)

Assuming d_{CT} is a constant, the height of the walls may be computed as

$$h = \tan(\alpha_{CT}) \cdot d_{CT}.$$

(7.2)

Given a vehicle's heading at t_i, Θ_i, and the azimuth of a satellite β_k, the relative azimuth of a satellite with respect to the vehicle's heading γ_k may be obtained as

$$\gamma_k = \beta_k - \Theta_i.$$

(7.3)

Then, the distance from the vehicle to the walls at this relative azimuth d_k is given by

$$d_k = \frac{d_{CT}}{\sin(\gamma_k)}.$$

(7.4)

Finally, the cutoff angle of a satellite α_k may be computed as

$$\alpha_k = \tan^{-1}\left(\frac{h}{d_k}\right).$$

(7.5)

If the elevation of a satellite is less than α_k, this satellite information is not used for the position computation. This algorithm simulates the urban area well. However, in reality it

is not likely that one will encounter a continuous array of buildings at the same height. It would be desirable to change the distance from the obstruction and its height so that the algorithm could create more realistic situation.

7.1.3 Simulation Results

A cross-track cutoff angle of 30, 45 and 60 degrees is applied to the test data using the virtual wall satellite rejection angle algorithm described above. This corresponds to wall heights of 5.77, 10.0 and 17.32 metres assuming a cross-track distance to the wall of $d_{CT} = 10.0$ m. To simulate intersections where better satellite coverage is expected and the vehicle is often brought to a stop, the satellite rejection algorithm is disabled when the vehicle speed is less than 10 metres per second. The unaided least squares, barometric height constraint least squares, height and gyro heading constraint least squares and height and heading constraint Kalman filter solutions are compared.

Figures 7.4 shows the visible satellites using the virtual wall concept at cross-track cutoff angles of 30, 45 and 60 degrees with 0 degree vehicle azimuth (heading north-south) and 90 degrees vehicle azimuth (east-west). Dotted lines in the figures indicate the cutoff thresholds generated by the algorithm. There are sufficient satellites when the cross-track cutoff angle is 30 degrees. Three satellites and weak geometry are observed when the cutoff angle is 45 and 60 degrees and the vehicle trajectory is east-west. Two satellites are visible when the cutoff angle is 60 degrees and the vehicle trajectory is north-south. Note that some satellites close to the threshold line may not be observed at a particular instance since the threshold angle is a function of the vehicle heading and satellite azimuth.

Cutoff Angle = 30°, Azimuth = 0°

Cutoff Angle = 30°, Azimuth = 90°

Cutoff Angle = 45°, Azimuth = 0°

Cutoff Angle = 45°, Azimuth = 90°

Cutoff Angle = 60°, Azimuth = 0°

Cutoff Angle = 60°, Azimuth = 90°
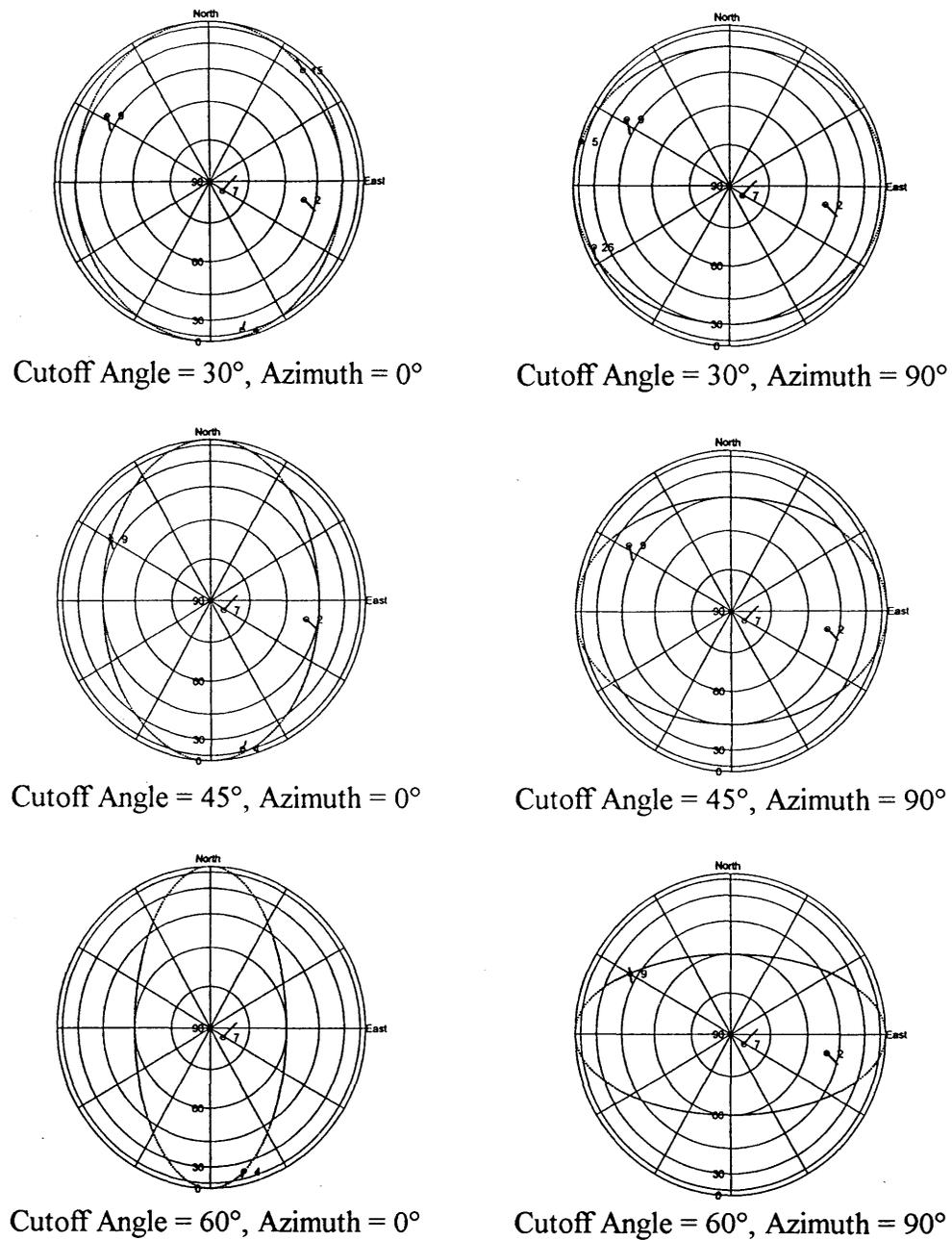
**Figure 7.4. Visible Satellites with Virtual Wall Concept,
Springbank, June 29, 1996**

The number of satellites, dilution of precision and range residuals are monitored to

determine the quality of the GPS solution. If one or more of these exceeds the

predetermined threshold value, the barometric height and / or heading constraint are used to improve the positioning accuracy. The threshold values are listed in Table 7.7. There may be a more effective strategy to properly determine whether the GPS estimate is acceptable. This topic is left for future investigation.

Table 7.7. Threshold Values for Acceptable GPS Estimate

Number of Satellites	≥ 4
HDOP = $[NDOP^2 + EDOP^2]^{1/2}$	≤ 10
Range Residuals (magnitude)	≤ 5.0 metres
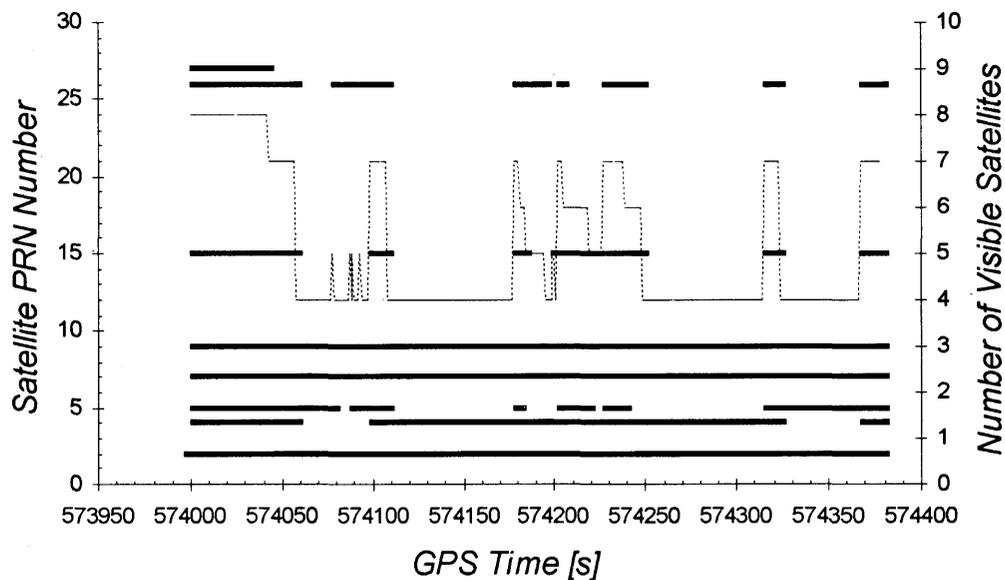
**Figure 7.5. Visible Satellites, Springbank, June 29, 1996.**
**(30° Cross-Track Cutoff Angle)**
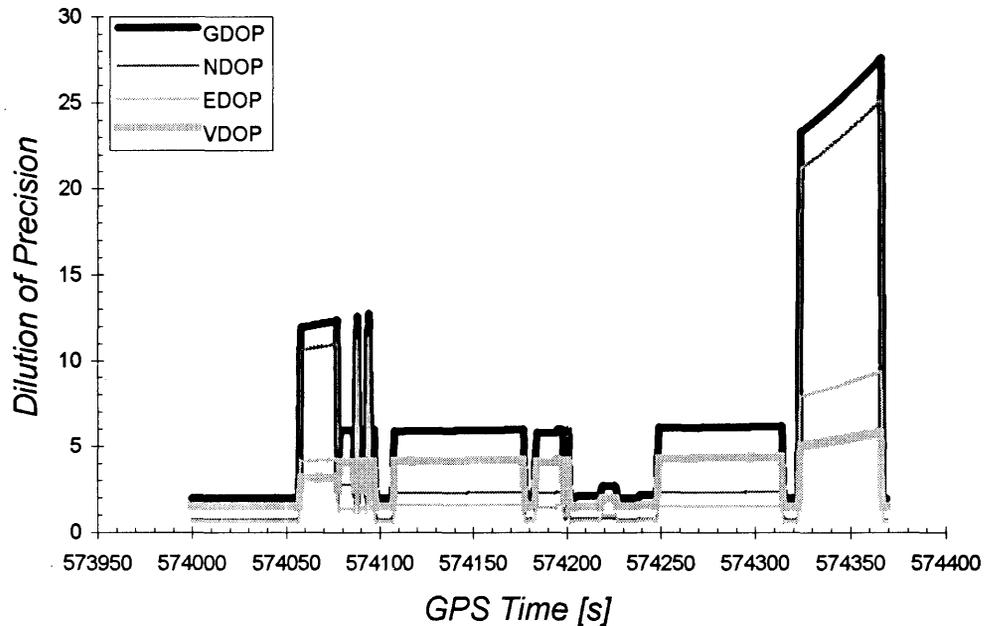
Figure 7.6. DOPs, Springbank, June 29, 1996.
(30° Cross-Track Cutoff Angle, Unaided Least Squares)

7.1.3.1 Cross-Track Cutoff Angle of 30 Degrees

At the cross-track cutoff angle of 30 degrees, the receiver could observe a sufficient number of GPS satellites all the time to compute position estimates. The number of observed satellites was four or more for the entire test as shown in Figure 7.5. In Figure 7.6, one sees, however, that poor satellite geometry developed at the end of the session. This occurred when the test vehicle was in Section A of Figure 7.1. It manifests itself as an unreasonably high NDOP. At that time the observed satellites, PRN 2, 5, 7 and 9, are almost lined up. Figures 7.7 and 7.8 show the 2D position plots using unaided least squares for the forward and reverse segment of the run. One sees from Figure 7.8 that the position estimates stray northerly and southerly from the reference trajectory (dotted line) by about two metres and there is a discontinuity due to a satellite constellation change.
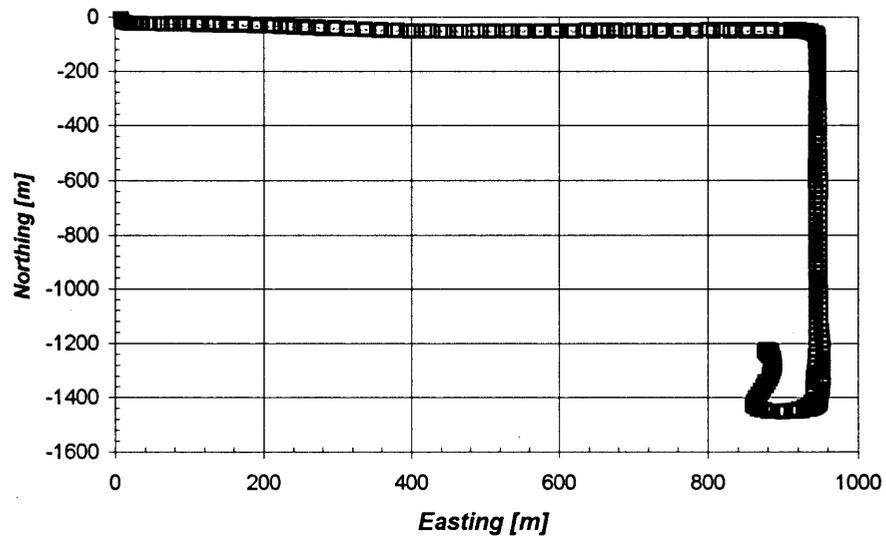
Figure 7.7. 2D Position, Springbank, June 29, 1996.
(30° Cross-Track Cutoff Angle, Unaided Least Squares)
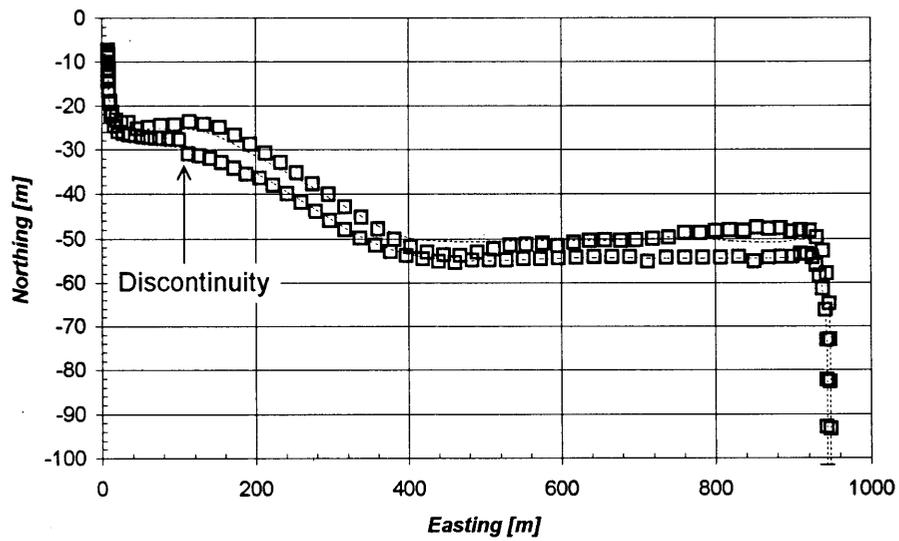
Figure 7.8. 2D Position, Section A, Springbank, June 29, 1996.
(30° Cross-Track Cutoff Angle, Unaided Least Squares)

Table 7.8. Position Estimate Difference Between Reference Trajectory and Unaided Least Squares Solutions, Springbank, June 29, 1996.
(30° Cross-Track Cutoff Angle)

	Latitude	Longitude	Height
Mean [m]	-2.02	-0.44	-0.51
Standard Deviation [m]	1.46	0.61	0.37
Max. Difference [m]	3.44	1.57	1.58
Min. Difference [m]	0.05	0.00	0.00
Position Availability	100 % / 356 epochs		
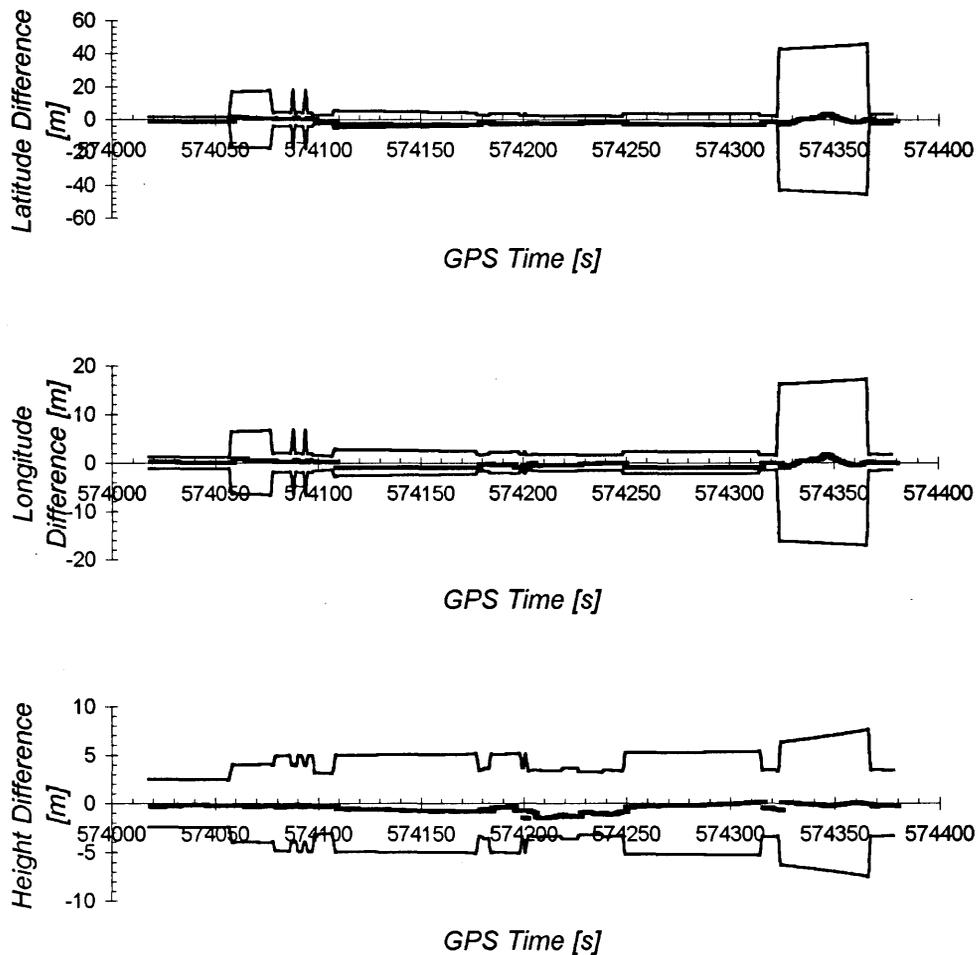
Figure 7.9. Unaided Least Squares Position Errors, Springbank, June 29, 1996.
(30° Cross-Track Cutoff Angle)

Figure 7.9 shows the differences between the reference trajectory and the unaided least squares solutions with 2σ error envelopes. 2σ estimated error envelopes are obtained from $\mathbf{C}_{\hat{\delta}}$, the covariance matrix associated with position estimates. For the least squares, $\mathbf{C}_{\hat{\delta}}$ may be computed by (Krakiwsky 1990)

$$\mathbf{C}_{\hat{\delta}} = \left[\mathbf{A}^{\mathrm{T}}\mathbf{C}_l^{-1}\mathbf{A}\right]^{-1} \tag{7.6}$$

where

$\mathbf{A}$ design matrix from equations (4.7) to (4.9),

$\mathbf{C}_l^{-1}$ weight matrix from equation (4.10).

For the Kalman filter, $\mathbf{C}_{\hat{\delta}}$ may be obtained from the covariance matrix associated with updated estimates $\mathbf{P}_k$ of equation (5.9). The 2σ error corresponds to the 95% probability region in 2-D, therefore 95% of errors should be within the envelope.

As seen in Figure 7.9, the differences between the reference trajectory and unaided least squares solutions are within the envelopes. The size of envelopes roughly corresponds to that of DOPs comparing Figures 7.6 and 7.9. The position estimator expects large position displacements when large DOPs are observed. One notices that the latitude and longitude position estimates do not maintain consistency at the start and end of the session. This agrees with the poor DOPs seen in Figure 7.6. The accuracy of the position estimates is still reasonable as summarized in Table 7.8. The DRMS is approximately 2.6m.

Height constraint least squares solutions are then examined. Although four or more satellites were observed for the entire session, the algorithm employed the height constraint when the HDOP computed with GPS data only was greater than 10. Figure 7.10 shows the DOPs with the height constraint. The DOPs are significantly decreased, especially the VDOP. One property of height constraint positioning is that with height information, the VDOP is always small, close to 1.0. The additional information also contributes to an improved NDOP and EDOP as explained in Tang (1996). As a result, the GDOP is reduced to about 12, from a maximum of over 25 as shown in Figure 7.6.

Figures 7.11 and 7.12 are 2D position plots with height constraint least squares positioning. Estimates are not superior to those of unaided least squares. They seem to be
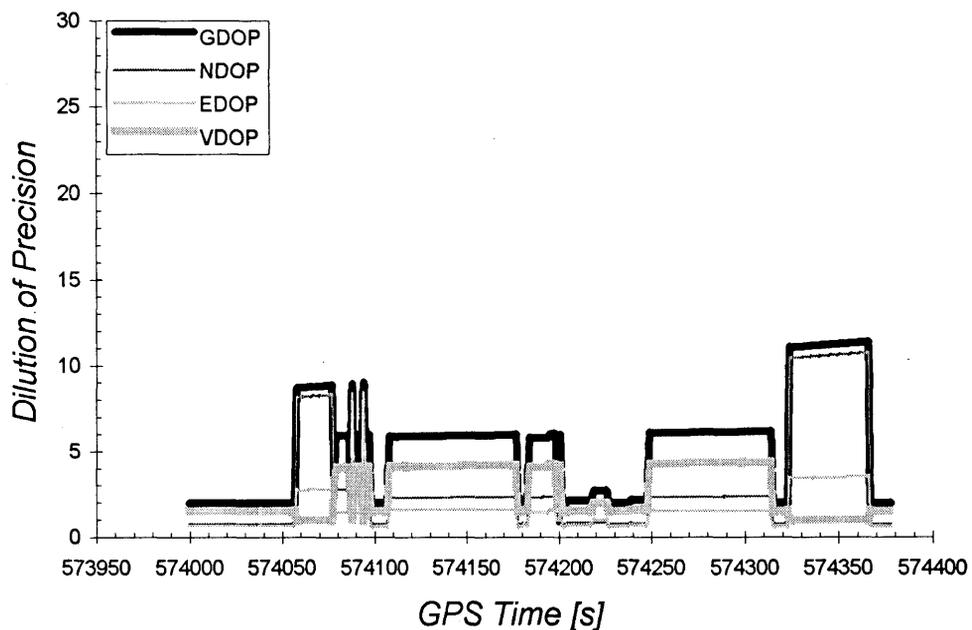

Figure 7.10. DOPs, Springbank, June 29, 1996.
**(30° Cross-Track Cutoff Angle, Height Constraint Least Squares)**

Table 7.9. Position Estimate Difference Between Reference Trajectory and Height Constraint Least Squares Solutions, Springbank, June 29, 1996. (30° Cross-Track Cutoff Angle)

|	Latitude	Longitude	Height
Mean [m]	-1.38	-0.17	-0.67
Standard Deviation [m]	2.87	1.15	0.49
Max. Difference [m]	9.35	4.05	2.37
Min. Difference [m]	0.07	0.00	0.00
Position Availability	100% / 356 epochs		

weak and wandering. Comparing Figure 7.12 to Figure 7.8, one sees that the solutions of Figure 7.12 deviate more than those of Figure 7.8. This may be due to the inferior barometric height accuracy to the GPS height. The height error in Figure 7.13 is larger than that in Figure 7.9. Figure 7.13 shows the difference between the reference trajectory and the height constraint least squares solutions with 2σ estimated error envelopes. The differences are within the envelopes. These envelopes are significantly smaller than those of unaided least squares (Figure 7.9) due to the improved redundancy. Since the sensor error models take cumulative errors into account as shown in equations (3.19) to (3.21), the estimated position errors should grow accordingly when the constraints are applied. As a consequence, estimated height errors are gradually increased at the beginning and end of the session as seen in Figure 7.13. As shown in Table 7.9, the latitude and longitude errors reach 9.35 and 4.05 metres, respectively. The DRMS is approximately 3.4 metres.
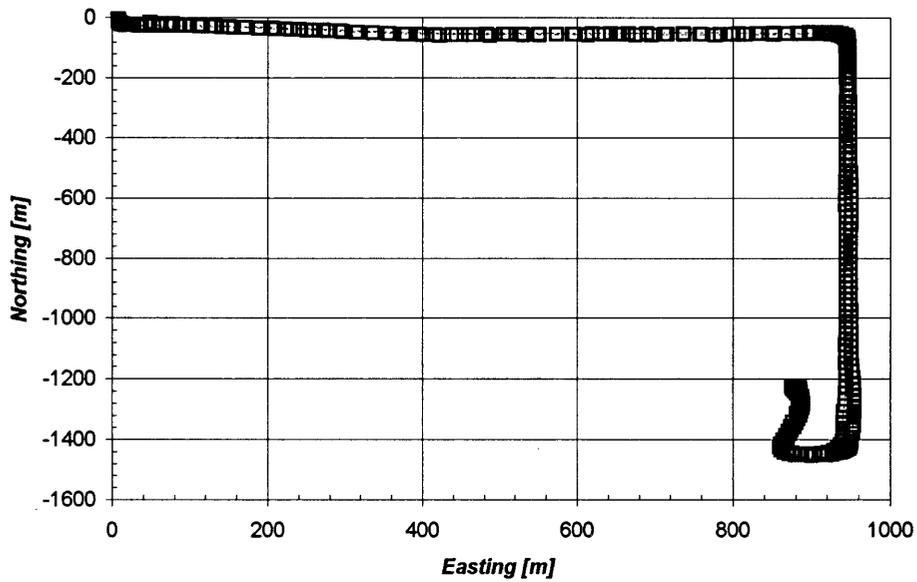
Figure 7.11. 2D Position, Springbank, June 29, 1996.
(30° Cross-Track Cutoff Angle, Height Constraint Least Squares)
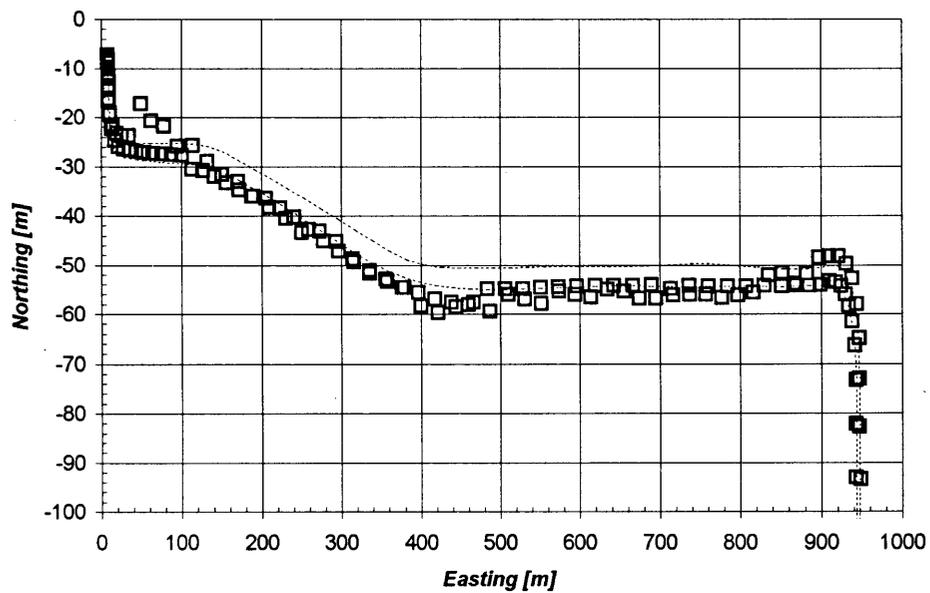
Figure 7.12. 2D Position, Section A, Springbank, June 29, 1996.
**(30° Cross-Track Cutoff Angle, Height Constraint Least Squares)**
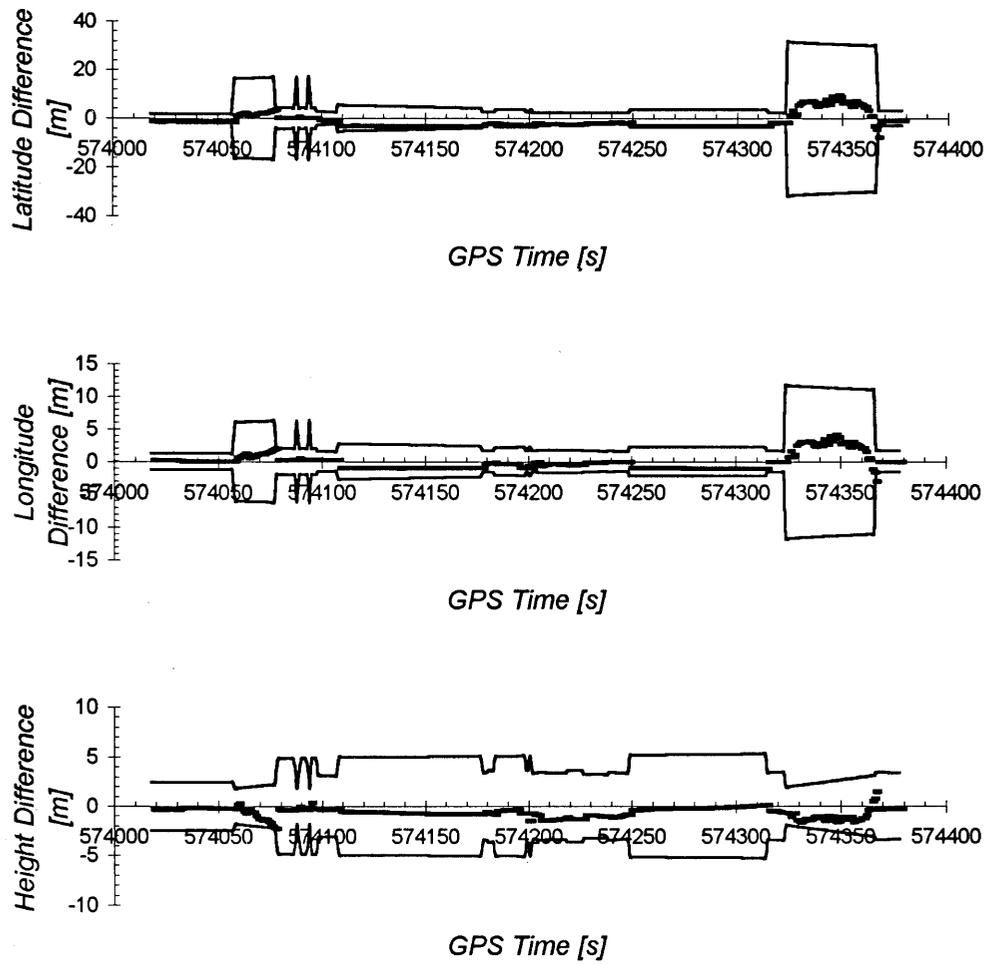
Figure 7.13. Height Constraint Least Squares Position Errors, Springbank, June 29, 1996. (30° Cross-Track Cutoff Angle)

Both height and heading constraints are used next. The observations, sensor measurements and constraint positioning periods of least squares are identical to those of the Kalman filter. As a consequence, the DOPs are also identical. Figure 7.14 shows the DOP plot with height and heading constraint positioning. One notices that the GDOP is further reduced to about 8. The satellite geometry is effectively enhanced by height and heading constraints.

The least squares estimator is first employed. Figures 7.15 and 7.16 are 2D position plots of the height and heading constraint least squares solutions. Two discontinuities are observed. These are caused by the GPS-only position updates. Errors at these points are mainly due to the sensor heading error, which grows in a quadratic fashion. The sensor heading error, which affects the horizontal position accuracy, may be seen more obviously in Figure 7.17. Latitude error grows rapidly towards the end of the trajectory, although the maximum errors and standard deviations shown in Table 7.10 are still well within the requirements. The resultant DRMS is approximately 2.8 metres.

Table 7.10. Position Estimate Difference Between Reference Trajectory and Height and Heading Constraint Least Squares Solutions, Springbank, June 29, 1996. (30° Cross-Track Cutoff Angle)

	Latitude	Longitude	Height
Mean [m]	-1.87	-0.35	-0.67
Standard Deviation [m]	1.91	0.77	0.48
Max. Difference [m]	5.89	2.39	2.35
Min. Difference [m]	0.08	0.00	0.00
Position Availability	100 % / 356 epochs		
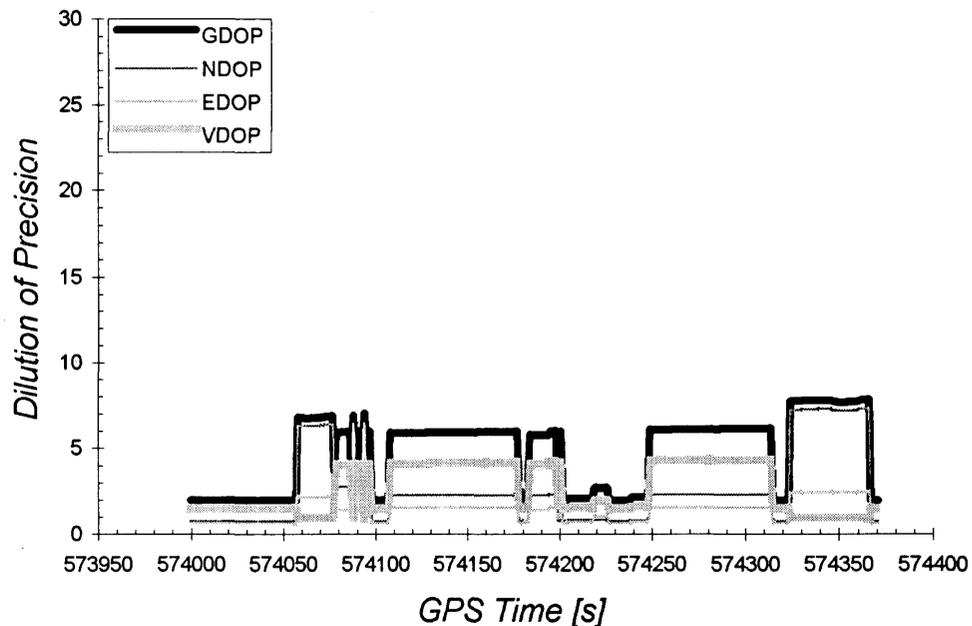
Figure 7.14. DOPs, Springbank, June 29, 1996.
(30° Cross-Track Cutoff Angle, Height and Heading Constraint
Least Squares and Kalman Filter)

Figure 7.17 shows the difference between the reference trajectory and the height and heading constraint least squares solutions with 2σ error envelopes. Error envelopes in Figure 7.17 are reduced as compared to the use of the height constraint positioning in Figure 7.13. All position errors are within the error envelopes. The error envelope growth at the end of the session is caused by the error increase in the height and heading constraints as a function of time. Thus, the sensor error models described in Chapter Three take the actual errors into account very well.

The Kalman filter estimator was also used. Figures 7.18 and 7.19 show 2D position plots of the height and heading constraint The Kalman filter solutions. Kalman filter solutions do not show a position discontinuity. This smoothness is a significant

advantage of Kalman filters. As shown in Table 7.11, the accuracy and standard deviation are both superior to those of the least squares due to the smoothed solutions. The maximum latitude and longitude errors are 4.15 and 1.42 metres, respectively. The DRMS is approximately 2.6 metres. The difference between the reference trajectory and the height and heading constraint Kalman filter solutions with 2σ estimated error envelopes are shown in Figure 7.20. The errors are mostly within error envelopes, indicating the filter is working properly. The error envelopes are similar to those generated by the least squares solutions.

The accuracy of constraint positioning largely depends on the quality of calibration and operation time. Prolonged sensor constraint positioning should be avoided since the sensor errors are cumulative.

Table 7.11. Position Estimate Difference Between Reference Trajectory and Height and Heading Constraint Kalman Filter Solutions, Springbank, June 29, 1996. (30° Cross-Track Cutoff Angle)

|	Latitude	Longitude	Height
Mean [m]	-2.11	-0.45	-0.67
Standard Deviation [m]	1.33	0.58	0.51
Max. Difference [m]	4.15	1.42	2.42
Min. Difference [m]	0.00	0.00	0.00
Position Availability	100 % / 356 epochs		
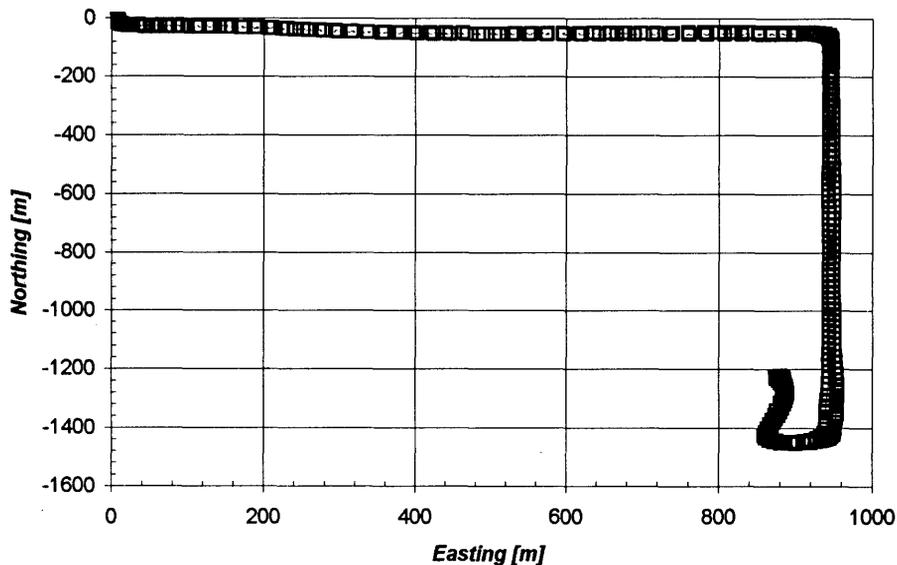
Figure 7.15. 2D Position, Springbank, June 29, 1996.
(30° Cross-Track Cutoff Angle, Height and Heading Constraint Least Squares)
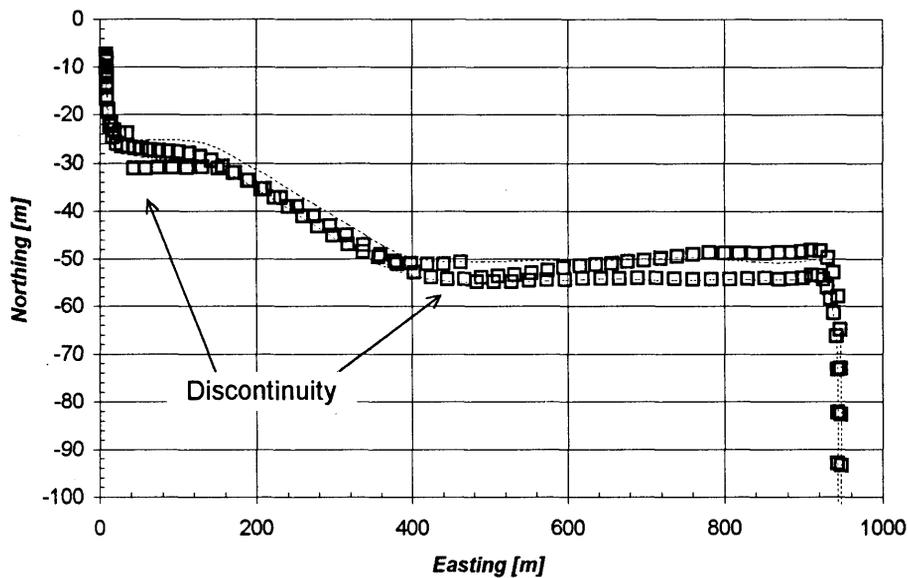

Figure 7.16. 2D Position, Section A, Springbank, June 29, 1996.
(30° Cross-Track Cutoff Angle, Height and Heading Constraint Least Squares)
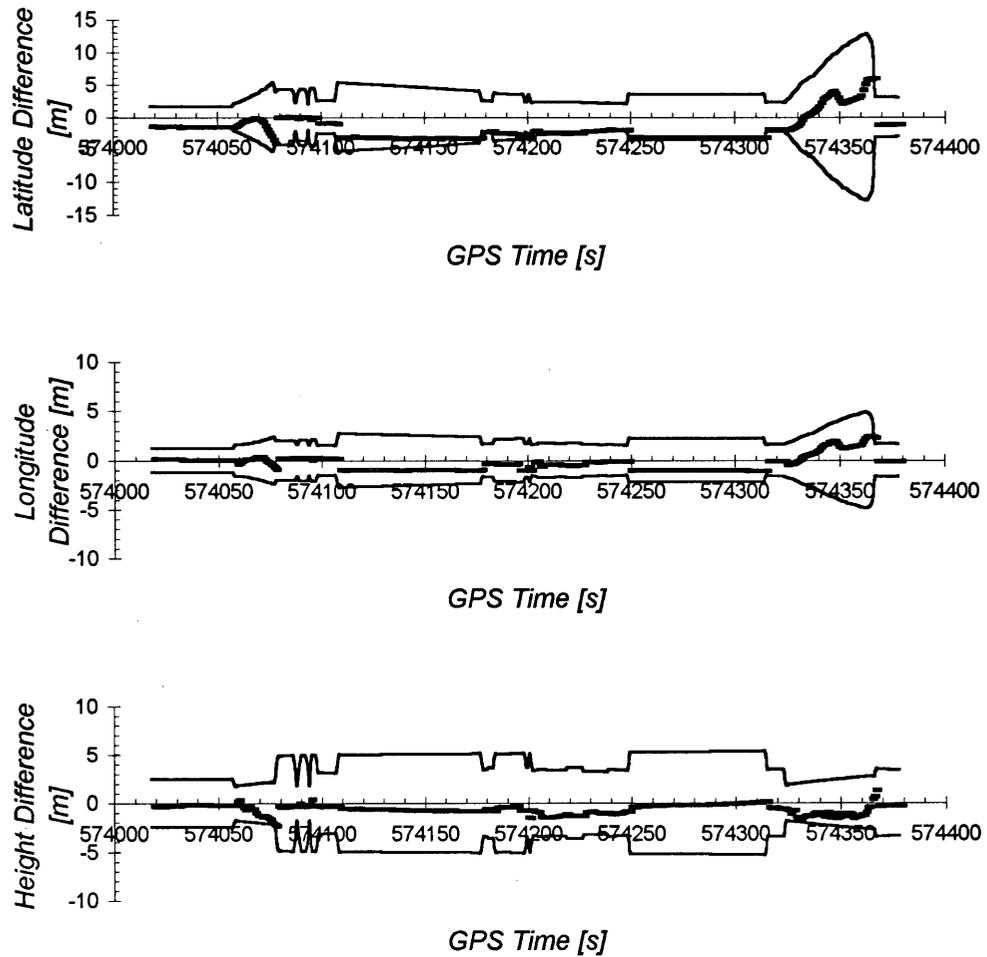
Figure 7.17. Height and Heading Constraint Least Squares Position Errors, Springbank, June 29, 1996. (30° Cross-Track Cutoff Angle)
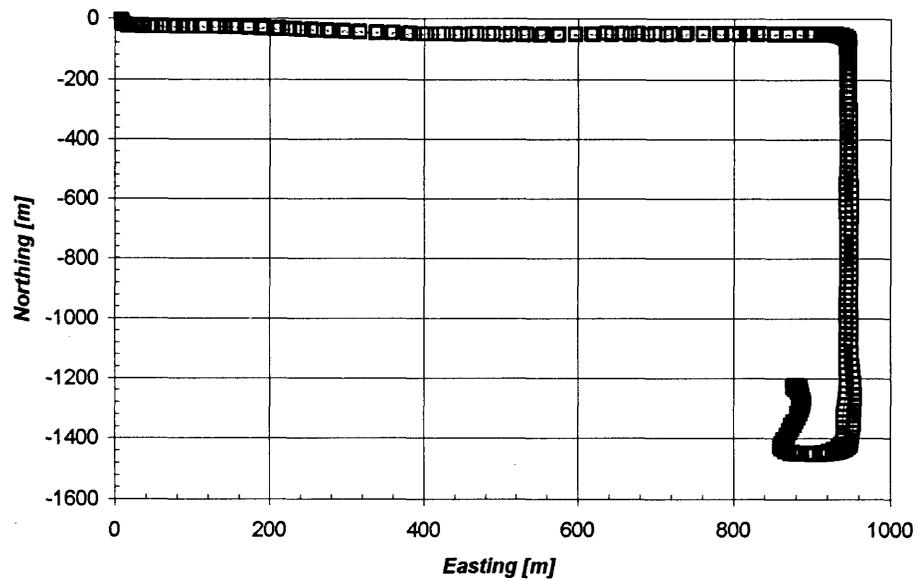
Figure 7.18. 2D Position, Springbank, June 29, 1996.
(30° Cross-Track Cutoff Angle, Height and Heading Constraint Kalman Filter)
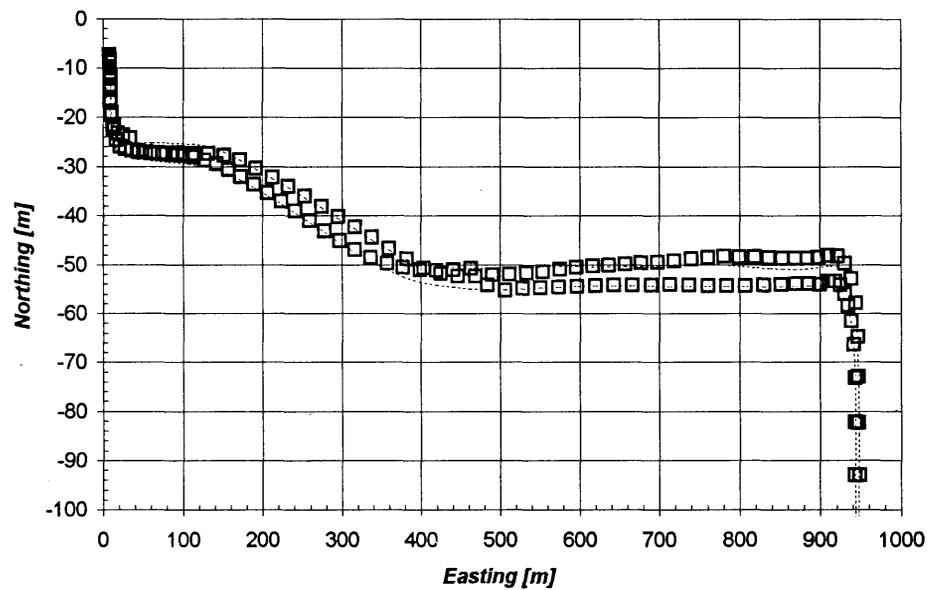
Figure 7.19. 2D Position, Section A, Springbank, June 29, 1996.
**(30° Cross-Track Cutoff Angle, Height and Heading Constraint Kalman Filter)**
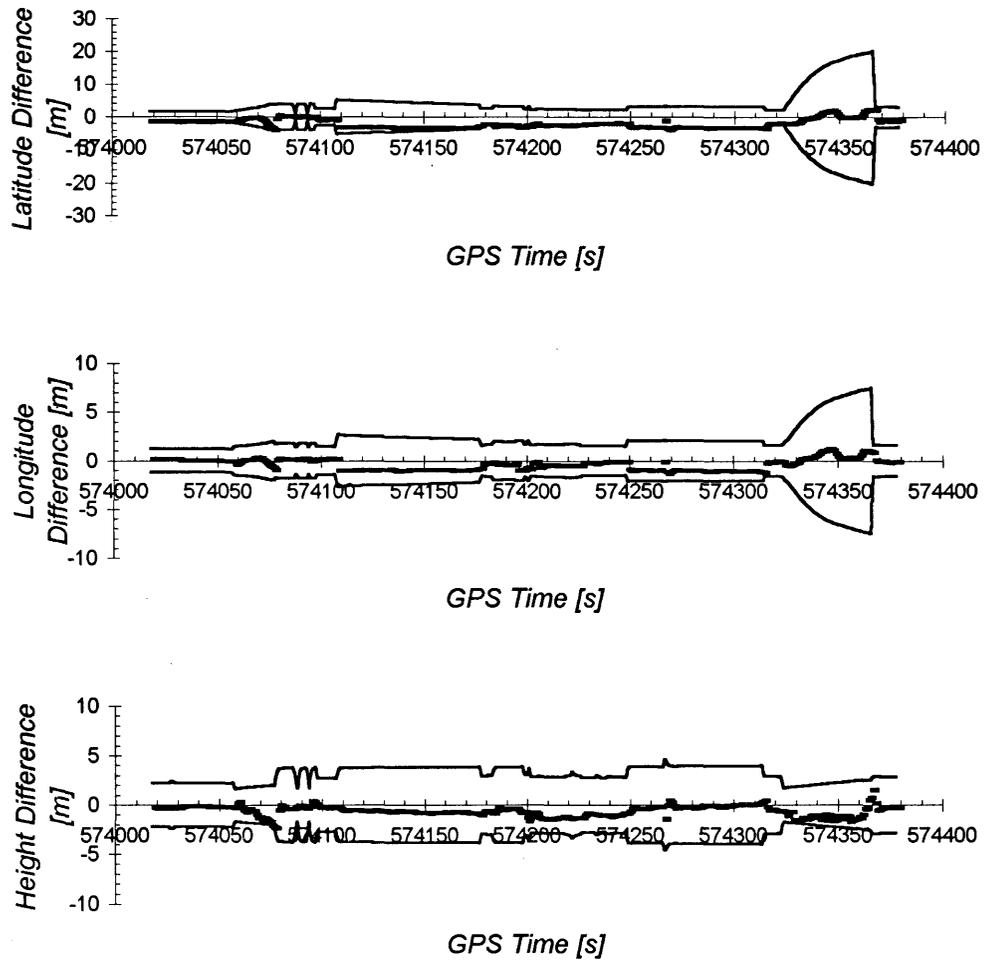
Figure 7.20. Height and Heading Constraint Kalman Filter Position Errors, Springbank, June 29, 1996. (30° Cross-Track Cutoff Angle)

### 7.1.3.2 Cross-Track Cutoff Angle of 45 Degrees

At the cross-track cutoff angle of 45 degrees, the receiver no longer observe a sufficient number of satellites for the entire operation. During two periods, the number of observed satellites drops to three for about 40 to 50 seconds as seen in Figure 7.21. The visible satellites during this outage period are PRN 2, 7 and 9. There are also short outage periods in the middle of the session. The DOPs during these outage periods become infinite as seen in Figure 7.22. Note that Figure 7.22 and the following DOP plots use a logarithmic vertical scale. Figures 7.23 and 7.24 show that the outage periods cause blanks in position estimates. Figure 25, position difference plot with 2σ error envelopes, shows that the position displacements stay within the envelopes when solutions are available. The standard deviations are 0.35 to 0.78 metres and the maximum errors are 1.12 to 3.44 metres as shown in Table 7.12. The DRMS is about 2.9m. Note that although the standard deviations in Table 7.12 are small, position availability is reduced to 73.9% of time or 263 out of 356 epochs.

Table 7.12. Position Estimate Difference Between Reference Trajectory and Unaided Least Squares Solutions, Springbank, June 29, 1996. (45° Cross-Track Cutoff Angle)

|	Latitude	Longitude	Height
Mean [m]	-2.65	-0.64	-0.55
Standard Deviation [m]	0.78	0.46	0.35
Max. Difference [m]	3.44	1.12	1.51
Min. Difference [m]	0.30	0.00	0.00
Position Availability	73.9 % / 263 epochs		
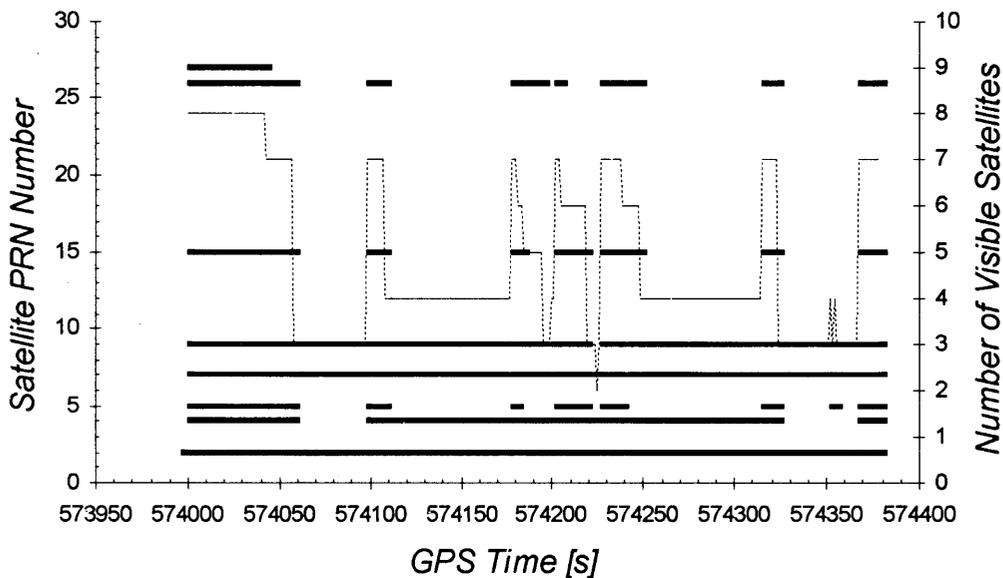
Figure 7.21. Visible Satellites, Springbank, June 29, 1996.
(45° Cross-Track Cutoff Angle)
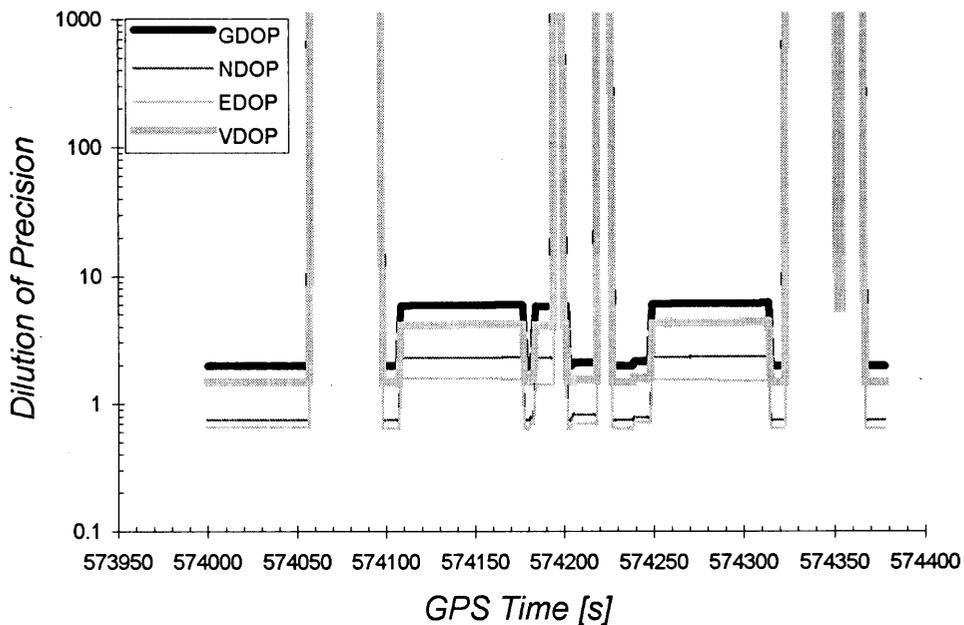
Figure 7.22. DOPs, Springbank, June 29, 1996.
**(45° Cross-Track Cutoff Angle, Unaided Least Squares)**
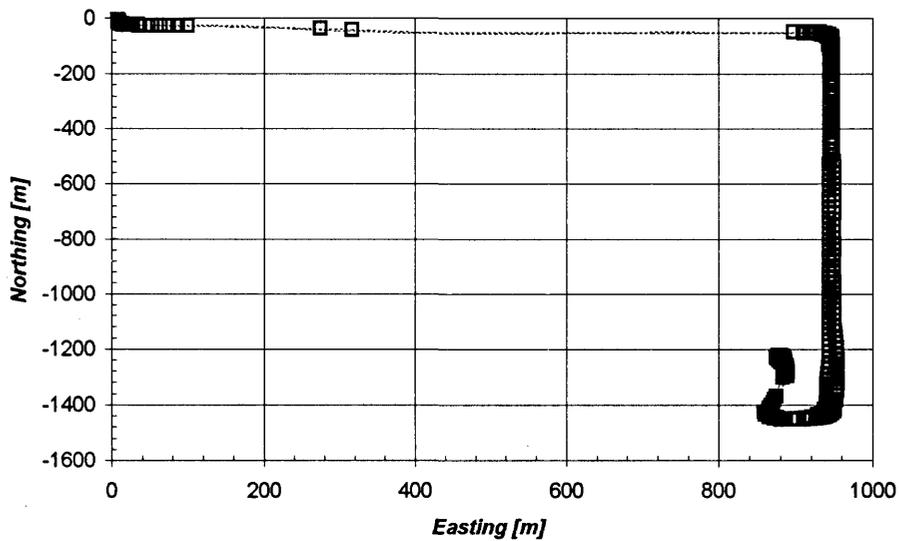
Figure 7.23. 2D Position, Springbank, June 29, 1996.
**(45° Cross-Track Cutoff Angle, Unaided Least Squares)**
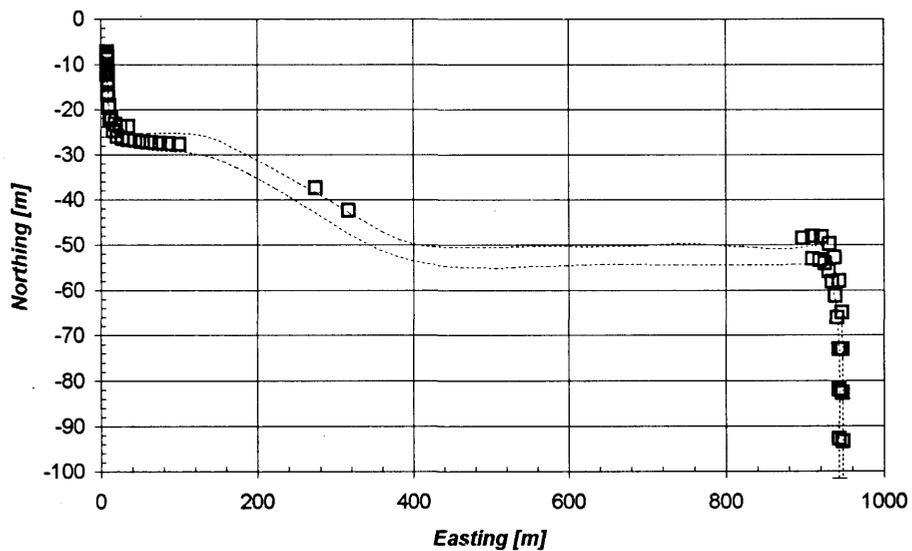
Figure 7.24. 2D Position, Section A, Springbank, June 29, 1996.
(45° Cross-Track Cutoff Angle, Unaided Least Squares)
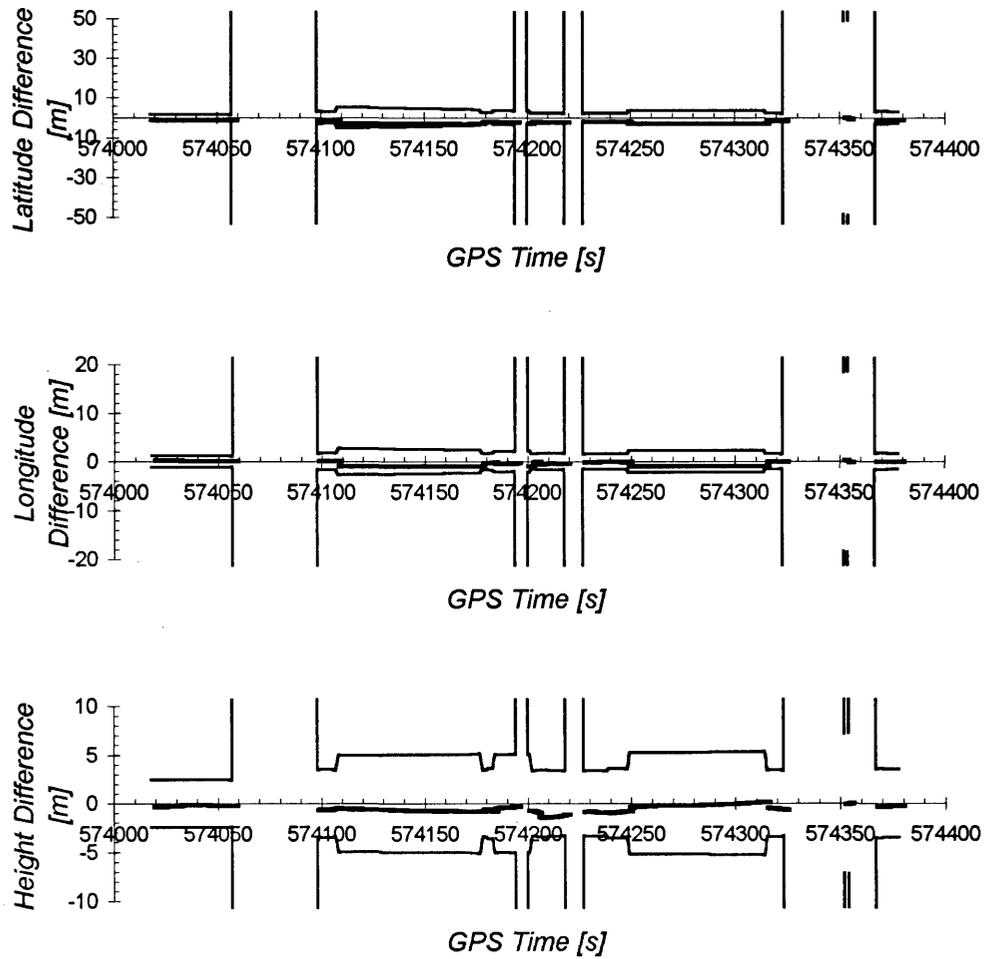
Figure 7.25. Unaided Least Squares Position Errors, Springbank, June 29, 1996. (45° Cross-Track Cutoff Angle)

Next, height constraint least squares is used for computation. Satellites PRN 2,7 and 9 form a weak geometry at the beginning and end of the session. Consequently, very large DOPs are observed as seen in Figure 7.26. The DOPs during the two long outage periods which correspond to Section A grow at a very rapid rate. NDOP is larger than EDOP during these periods since the satellites are aligned roughly in an east-west direction. This satellite constellation is typically seen in urban environments due to buildings along the road (Hayashi 1996). NDOP and GDOP exceed 100.

Figures 7.27 and 7.28 are the 2D position plots. Poor satellite geometry is reflected in the horizontal position errors seen in these figures. The differences between the reference trajectory and height constraint solutions with 2σ error envelopes are shown in Figure 7.29. The envelopes of latitude and longitude are very large during the constraint positioning period suggesting a poor geometry which results in a poor horizontal positioning accuracy. The maximum position error reaches 41.1 metres in latitude and 16.7 metres in longitude as shown in Table 7.13. The DRMS is approximately 9.6 metres. Latitude and longitude solutions oscillate at larger magnitudes than those with a cross-track cutoff angle of 30° as seen in Figure 7.29. This is probably caused by a poorer horizontal satellite geometry. The height error is within a reasonable level. The maximum height error is 2.7 metres and the VDOP is approximately 1.0. The height constraint maintains the height error within an acceptable level, however, it may not improve the horizontal position accuracy significantly. There is one epoch when the solution did not converge. The position availability is 99.7% of time or 355 out of 356 epochs.
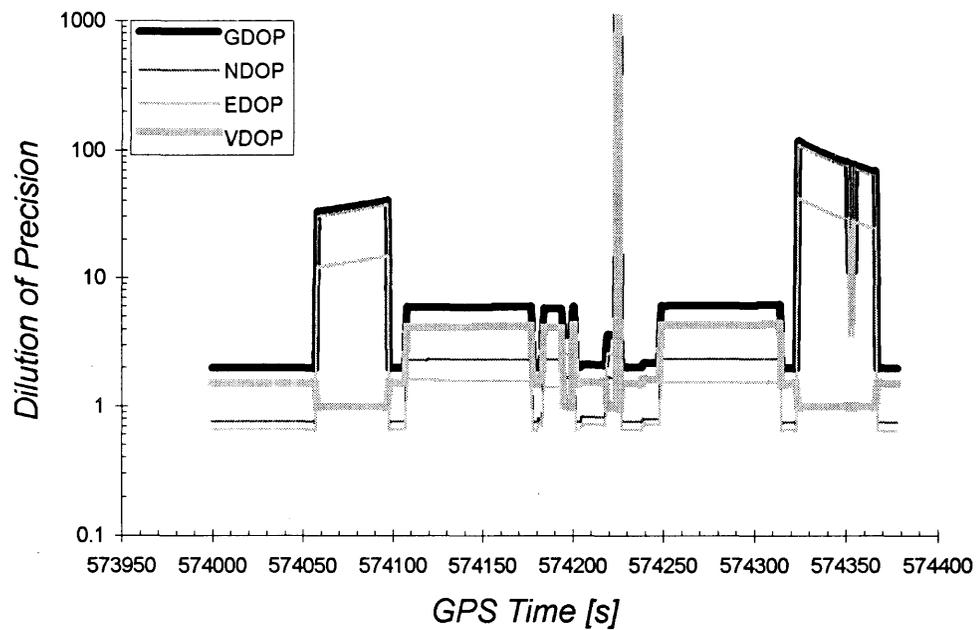
Figure 7.26. DOPs, Springbank, June 29, 1996.
(45° Cross-Track Cutoff Angle, Height Constraint Least Squares)

Table 7.13. Position Estimate Difference Between Reference Trajectory and
Height Constraint Least Squares Solutions, Springbank, June 29, 1996.
(45° Cross-Track Cutoff Angle)

	Latitude	Longitude	Height
Mean [m]	-1.20	-0.11	-0.68
Standard Deviation [m]	8.85	3.63	0.65
Max. Difference [m]	41.12	16.67	2.69
Min. Difference [m]	0.09	0.00	0.00
Position Availability	99.7 % / 355 epochs		
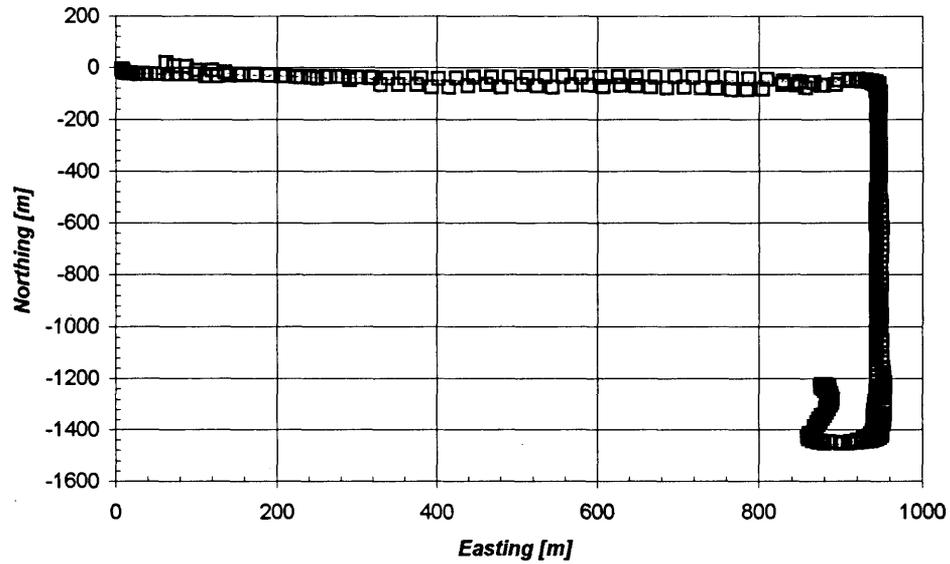
Figure 7.27. 2D Position, Springbank, June 29, 1996.
(45° Cross-Track Cutoff Angle, Height Constraint Least Squares)
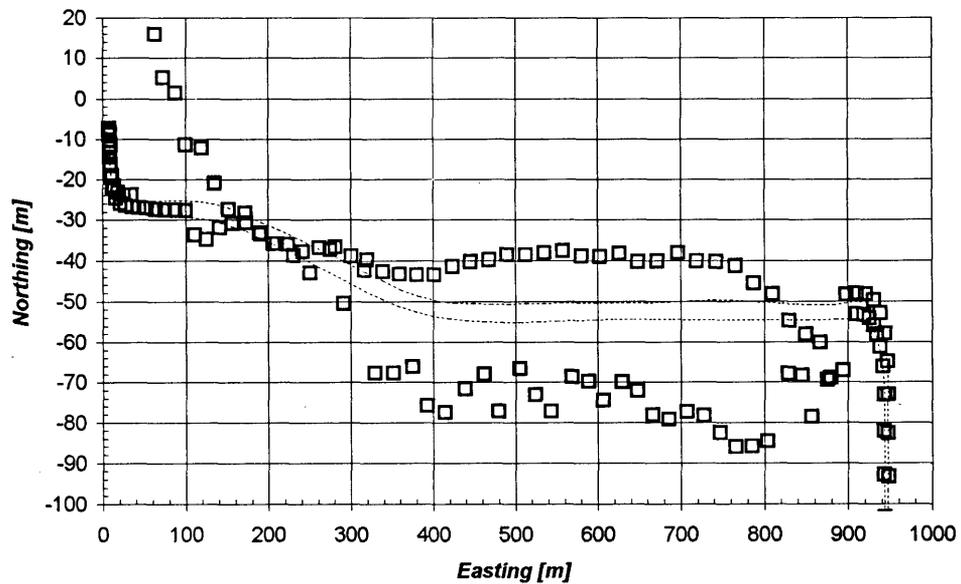
Figure 7.28. 2D Position, Section A, Springbank, June 29, 1996.
(45° Cross-Track Cutoff Angle, Height Constraint Least Squares)
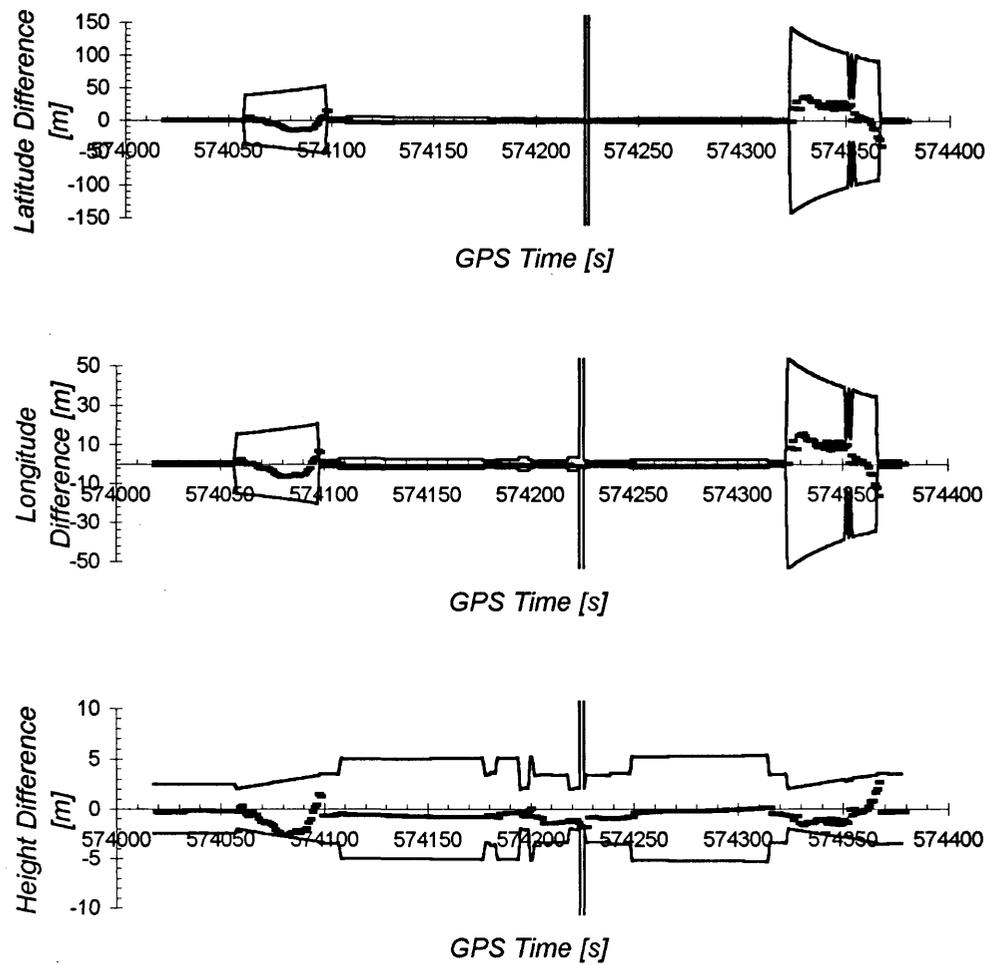
Figure 7.29. Height Constraint Least Squares Position Errors, Springbank, June 29, 1996. (45° Cross-Track Cutoff Angle)

Heading constraint is then applied in addition to height constraint. Both the least squares and Kalman filter solutions are examined. Figure 7.30 shows the effectiveness of adding the heading constraint. The NDOP and GDOP are now reduced to approximately 10. Comparing Figure 7.30 with Figure 7.26, the heading constraint improves the NDOP as well as EDOP. The heading constraint effectively improves the horizontal satellite geometry.

The position accuracy is also improved. Figures 7.31 and 7.32 are 2D position plots with height and heading constraint least squares. The solutions are consistent. The standard deviations have improved to 1.79 metres in latitude and 0.84 metres in longitude as seen in Table 7.14. The DRMS is approximately 3.2 metres. A longitude error of 4.86 metres in the middle of the session is seen in Figure 7.33. This error exceeds the 2σ error envelope and may be caused by the GPS range errors which is not modeled. Since there is less redundancy in solutions in urban environments, these solutions become vulnerable to range errors. There is one epoch when the solution did not converge. Consequently, the position availability with height and heading constraint least squares is 99.7% of time or 355 out of 356 epochs.

Table 7.14. Position Estimate Difference Between Reference Trajectory and Height and Heading Constraint Least Squares Solutions, Springbank, June 29, 1996. (45° Cross-Track Cutoff Angle)

	Latitude	Longitude	Height
Mean [m]	-2.39	-0.61	-0.68
Standard Deviation [m]	1.79	0.84	0.64
Max. Difference [m]	6.88	4.86	2.67
Min. Difference [m]	0.08	0.00	0.00
Position Availability	99.7 % / 355 epochs		
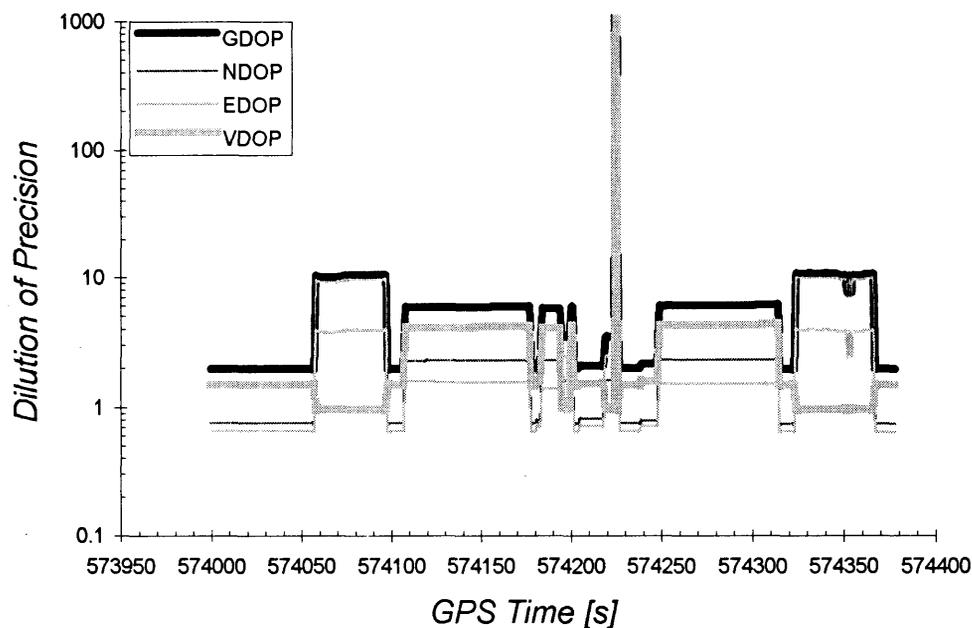
Figure 7.30. DOPs, Springbank, June 29, 1996.
(45° Cross-Track Cutoff Angle,
Height and Heading Constraint Least Squares and Kalman Filter)

Figures 7.34 and 7.35 show 2D position plots of height and heading constraint Kalman filter solutions. Kalman filter solutions are smoother than least squares solutions due to the filtering process. The differences between the reference trajectory and height and heading constraint solutions with 2σ error envelopes are shown in Figure 7.36. Errors are within the envelopes except for the longitude error in the middle of the session. The error envelopes produced by the least squares and Kalman solutions are comparable. Table 7.15 shows larger position displacements compared to Table 7.14. The latitude and longitude maximum position displacements of Kalman filter solutions are 7.31 and 11.11 metres, respectively, while those of least squares solutions are 6.88 and 4.86 metres. This may be caused by the Kalman filter mechanism, which does not have a divergence state as

discussed in Chapter Six. It appears that the Kalman filter produces solutions even with extremely poor measurements. The range residual checking algorithm did not warn of contaminated range measurements. More stringent error detection routines may be required. Position availability for height and heading constraint Kalman filter positioning is 100%. The DRMS is approximately 3.2 metres. Position availability at a 45° cross-track cutoff angle is summarized in Table 7.16.

Table 7.15. Position Estimate Difference Between Reference Trajectory and Height and Heading Constraint Kalman Filter Solutions, Springbank, June 29, 1996.
**(45° Cross-Track Cutoff Angle)**

	Latitude	Longitude	Height
Mean [m]	-2.47	-0.68	-0.70
Standard Deviation [m]	1.63	1.05	0.63
Max. Difference [m]	7.31	11.11	2.67
Min. Difference [m]	0.00	0.00	0.00
Position Availability	100 % / 356 epochs		

Table 7.16. Position Estimate Availability, Springbank, June 29, 1996.
(45° Cross-Track Cutoff Angle)

Estimation Mode	Position Estimate Availability	DRMS
Unaided Least Squares	263 epochs / 73.9%	2.9m
Height Constraint Least Squares	355 epochs / 99.7%	9.6m
Sensor Constraint Least Squares	355 epochs / 99.7%	3.2m
Sensor Constraint Kalman	356 epochs / 100%	3.2m
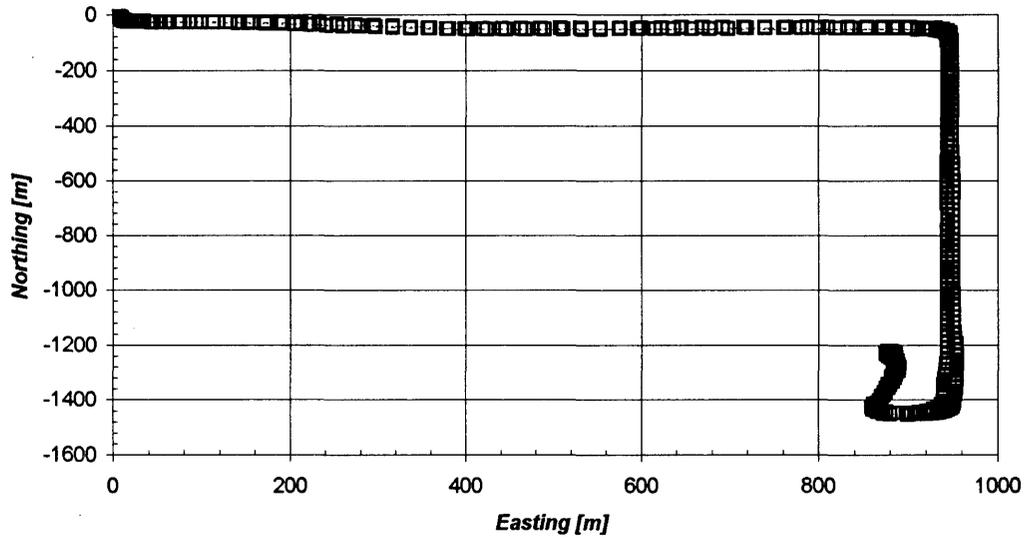
Figure 7.31. 2D Position, Springbank, June 29, 1996.
(45° Cross-Track Cutoff Angle, Height and Heading Constraint Least Squares)
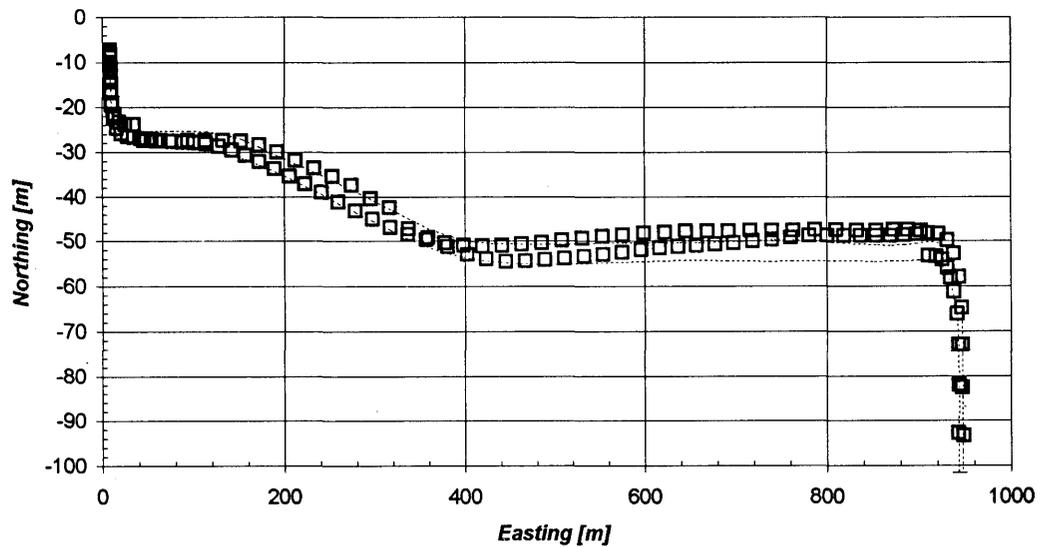
Figure 7.32. 2D Position, Section A, Springbank, June 29, 1996.
(45° Cross-Track Cutoff Angle, Height and Heading Constraint Least Squares)
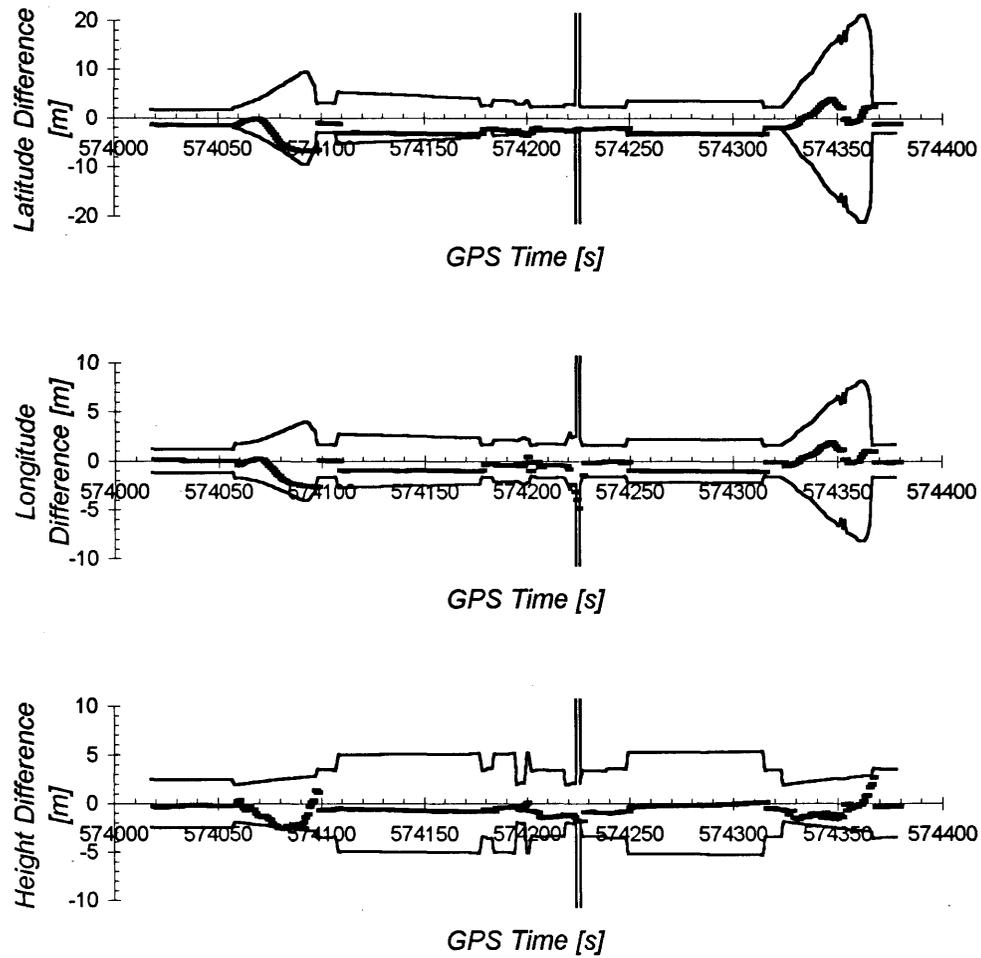
Figure 7.33. Height and Heading Constraint Least Squares Position Errors, Springbank, June 29, 1996.
**(45° Cross-Track Cutoff Angle)**
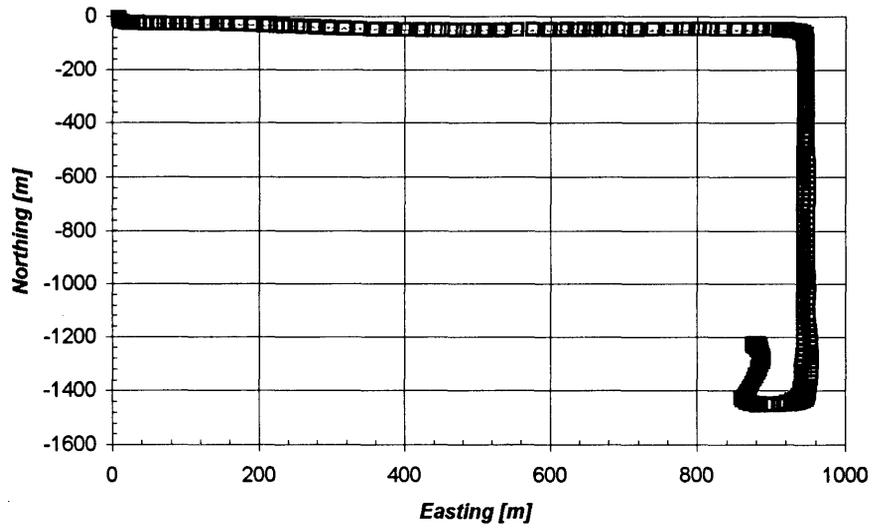
Figure 7.34. 2D Position, Springbank, June 29, 1996.
(45° Cross-Track Cutoff Angle, Height and Heading Constraint Kalman Filter)
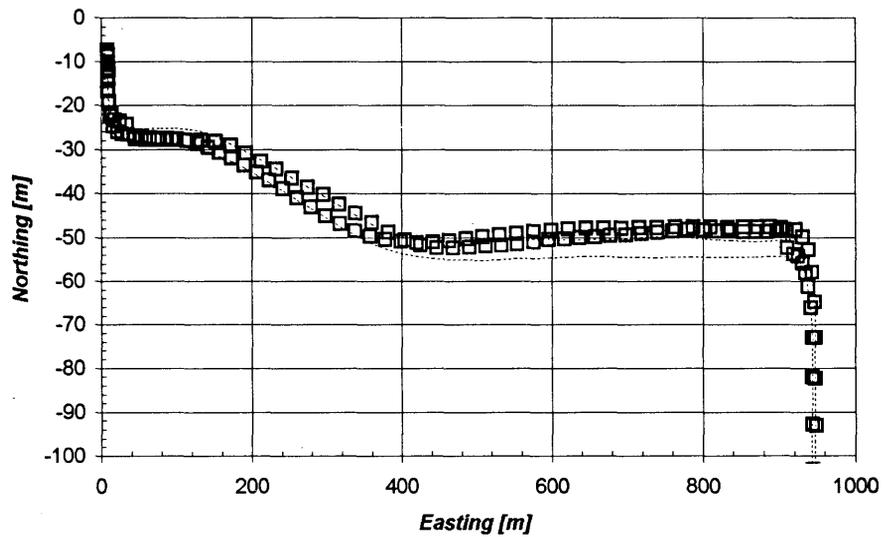

Figure 7.35. 2D Position, Section A, Springbank, June 29, 1996.
(45° Cross-Track Cutoff Angle, Height and Heading Constraint Kalman Filter)
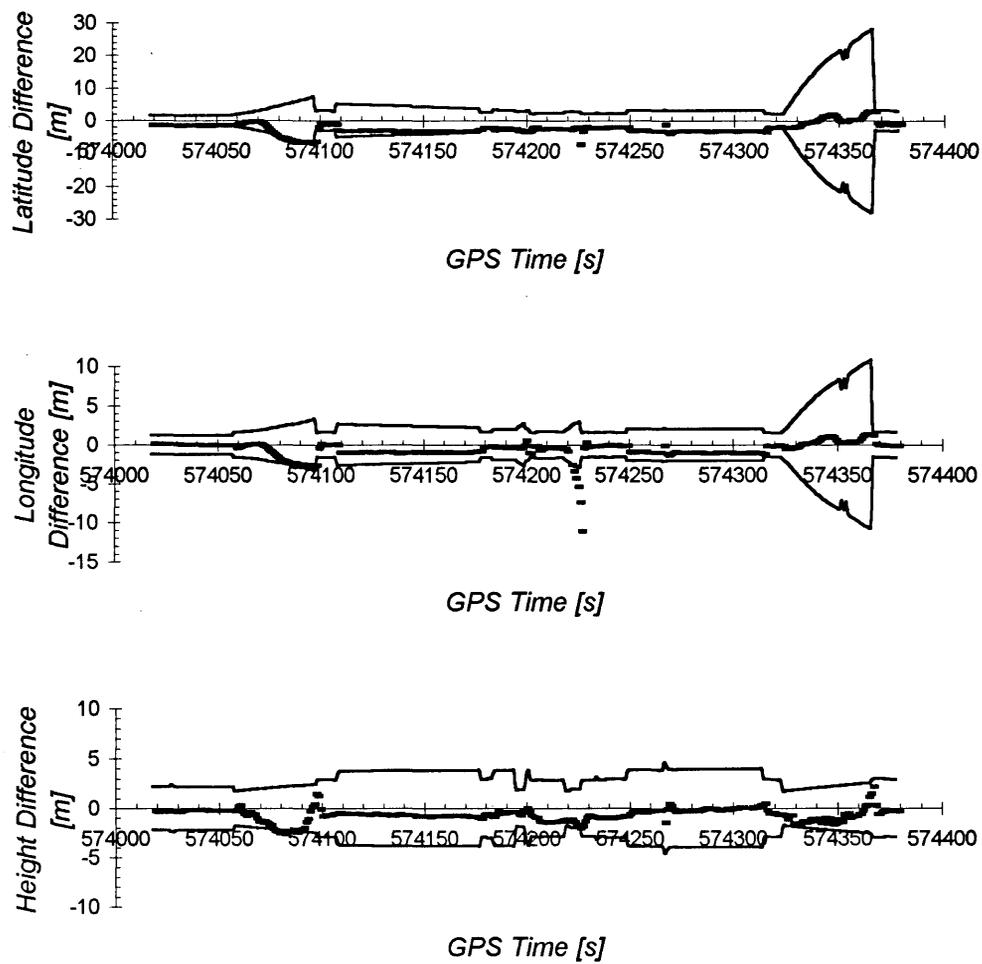
Figure 7.36. Height and Heading Constraint Kalman Filter Position Errors, Springbank, June 29, 1996.
(45° Cross-Track Cutoff Angle)

7.1.3.3 Cross-Track Cutoff Angle of 60 Degrees

Many satellites are rejected at a 60° cross-track cutoff angle. Figure 7.37 shows the visible satellites at a 60° cross-track cutoff angle. The number of visible satellites is three in Section A and one to two in Section B. Unaided least squares barely works in this case. Figure 7.38 shows the DOPs and Figures 7.39 and 7.40 show the 2D position plots for the unaided least squares solutions. Position determination is nearly impossible at a 60° cross-track cutoff angle. Figure 7.41 shows the differences between the reference trajectory and the unaided solutions with 2σ error envelopes. When solutions are available, they seem good as seen in Table 7.17 and Figure 7.41. The DRMS is about 2.0m. However, the position availability is only 34.8% of time or 124 of 356 epochs.
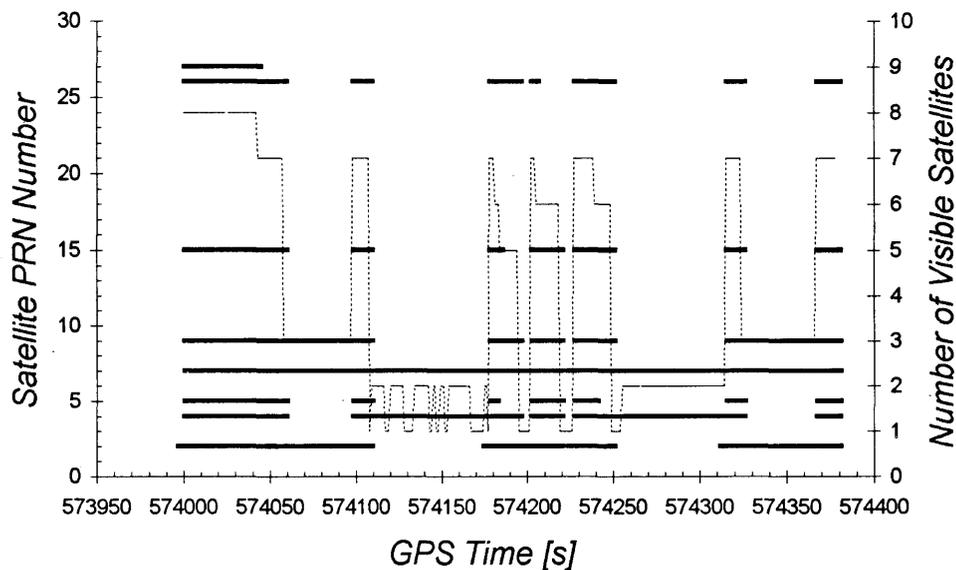
Figure 7.37. Visible Satellites, Springbank, June 29, 1996.
(60° Cross-Track Cutoff Angle)

Table 7.17. Position Estimate Difference Between Reference Trajectory and Unaided Least Squares Solutions, Springbank, June 29, 1996.
(60° Cross-Track Cutoff Angle)

	Latitude	Longitude	Height
Mean [m]	-1.86	0.04	-0.59
Standard Deviation [m]	0.52	0.33	0.54
Max. Difference [m]	1.28	0.84	1.17
Min. Difference [m]	0.02	0.00	0.00
Position Availability	34.8 % / 124 epochs		
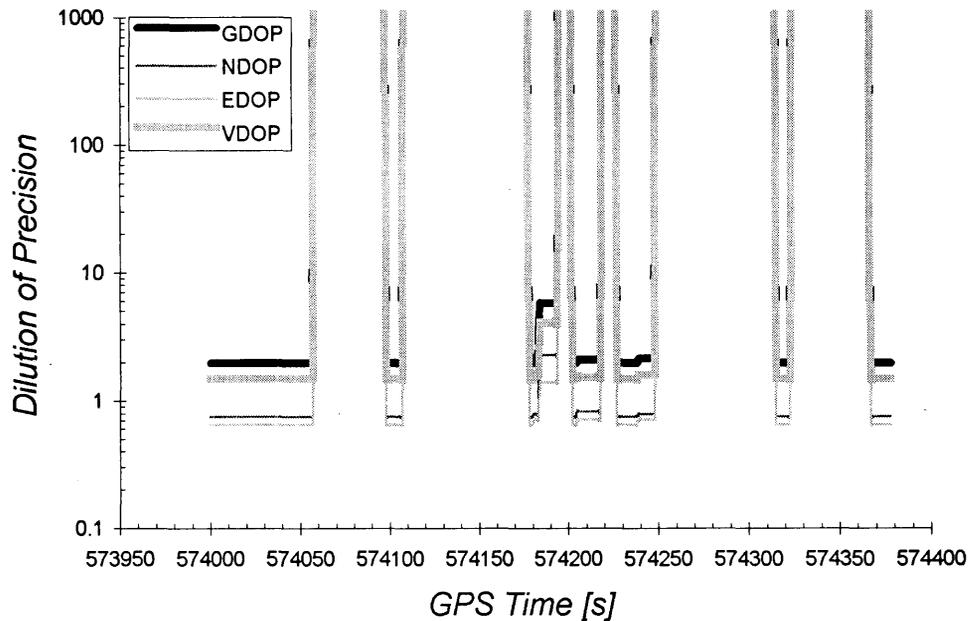
Figure 7.38. DOPs, Springbank, June 29, 1996.
(60° Cross-Track Cutoff Angle, Unaided Least Squares)
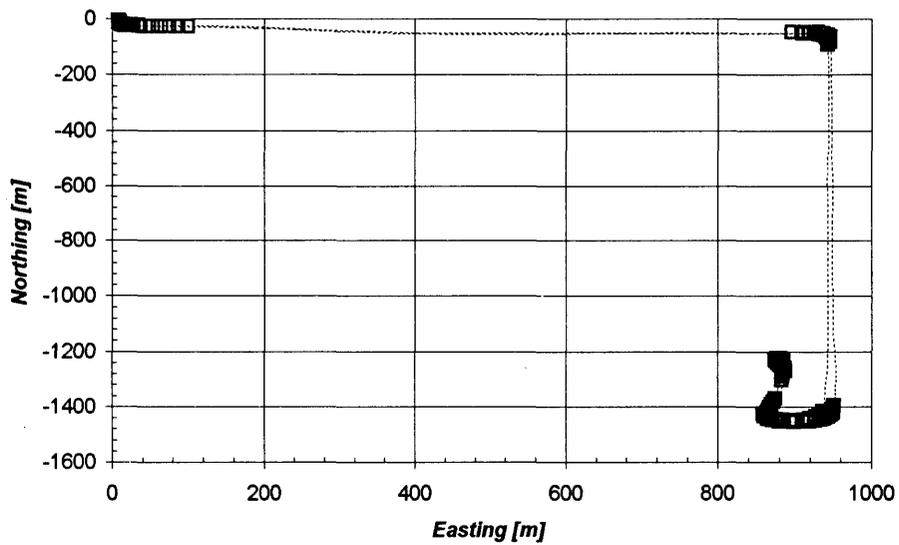
Figure 7.39. 2D Position, Springbank, June 29, 1996.
(60° Cross-Track Cutoff Angle, Unaided Least Squares)
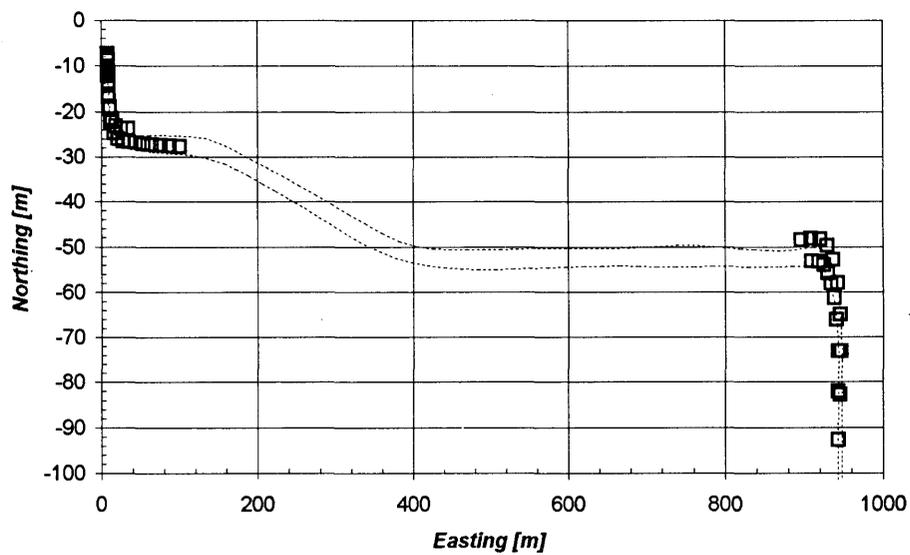
Figure 7.40. 2D Position, Section A, Springbank, June 29, 1996.
(60° Cross-Track Cutoff Angle, Unaided Least Squares)
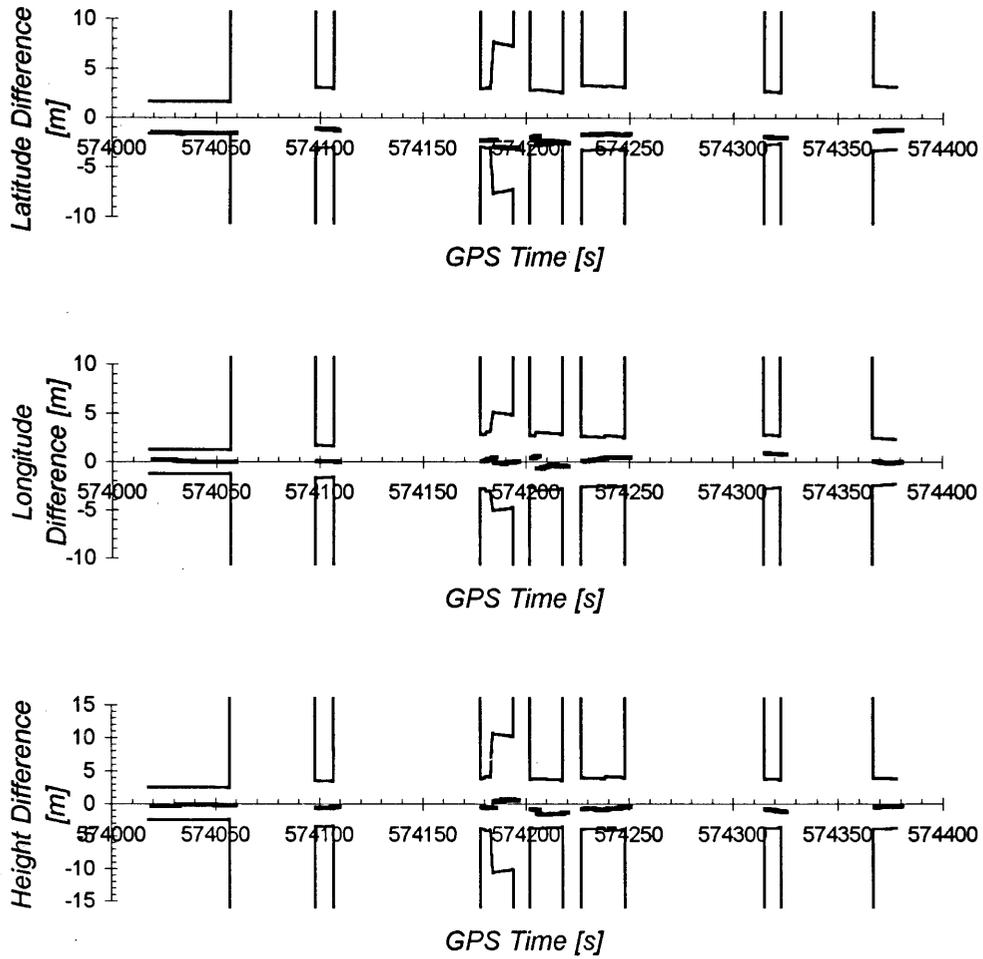
Figure 7.41. Unaided Least Squares Position Errors, Springbank, June 29, 1996. (60° Cross-Track Cutoff Angle)

Height constraint least squares positioning is evaluated next. Figure 7.42 is the DOP plot for height constraint least squares. Since the visible satellites in Section A are identical to those for a 45° cross-track cutoff angle, we see the DOPs growing rapidly as seen in Figure 7.26. NDOP and GDOP occasionally exceed 100. One may notice two outage periods caused by insufficient GPS observations.

Figures 7.43 and 7.44 are 2D position plots. Height constraint least squares solutions for a 60° cross-track cutoff angle behave similar to those for a 45° cross-track cutoff angle except in Section B. There, no position is obtained. Figure 7.45 shows the differences between the reference trajectory and the height constraint solutions with 2σ error envelopes. The algorithm expects a large horizontal position error when the height constraint is activated and widen the error envelopes accordingly. This error is largely due to a very poor horizontal satellite geometry. The horizontal position accuracy of height constraint least squares is poor as seen in Table 7.18 and Figure 7.45. The standard deviations of latitude and longitude are 15.73 and 6.06 metres, while maximum errors are 42.35 and 16.62 metres, respectively. The DRMS is approximately 17.5 metres. One may notice larger latitude and longitude standard deviations in Table 7.18 compared to Table 7.13. This is due to a poor GPS coverage. Position availability is 58.2% of time or 207 out of 356 epochs. Therefore, height constraint improves position availability by 23.4%, from 34.8% to 58.2%, although the accuracy is not satisfactory.
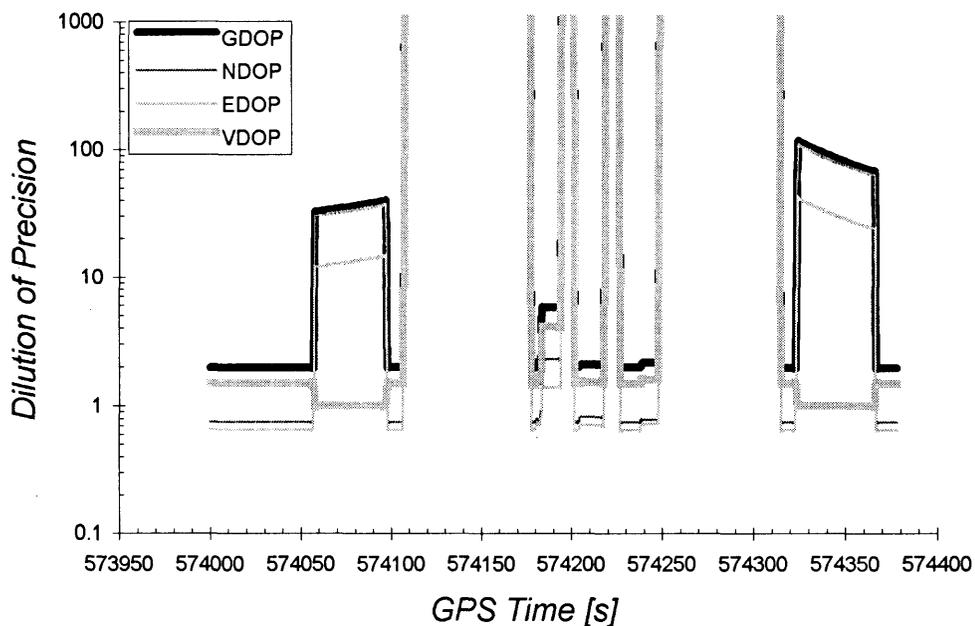
Figure 7.42. DOPs, Springbank, June 29, 1996.
(60° Cross-Track Cutoff Angle, Height Constraint Least Squares)

Table 7.18. Position Estimate Difference Between Reference Trajectory and
Height Constraint Least Squares Solutions, Springbank, June 29, 1996.
**(60° Cross-Track Cutoff Angle)**

	Latitude	Longitude	Height
Mean [m]	4.13	2.11	-0.93
Standard Deviation [m]	15.73	6.06	0.82
Max. Difference [m]	42.35	16.62	2.38
Min. Difference [m]	0.07	0.13	0.00
Position Availability	58.2 % / 207 epochs		
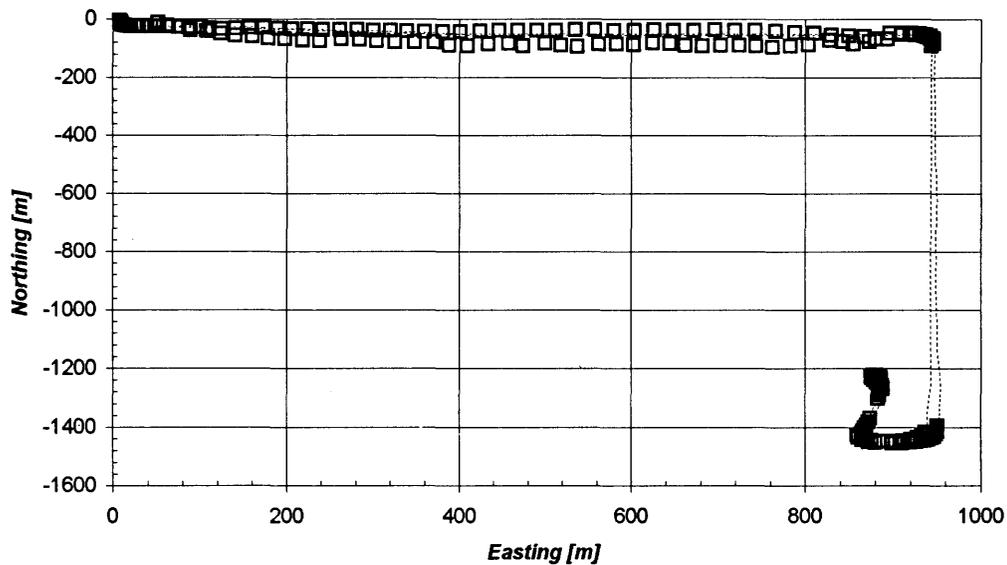
Figure 7.43. 2D Position, Springbank, June 29, 1996.
(60° Cross-Track Cutoff Angle, Height Constraint Least Squares)
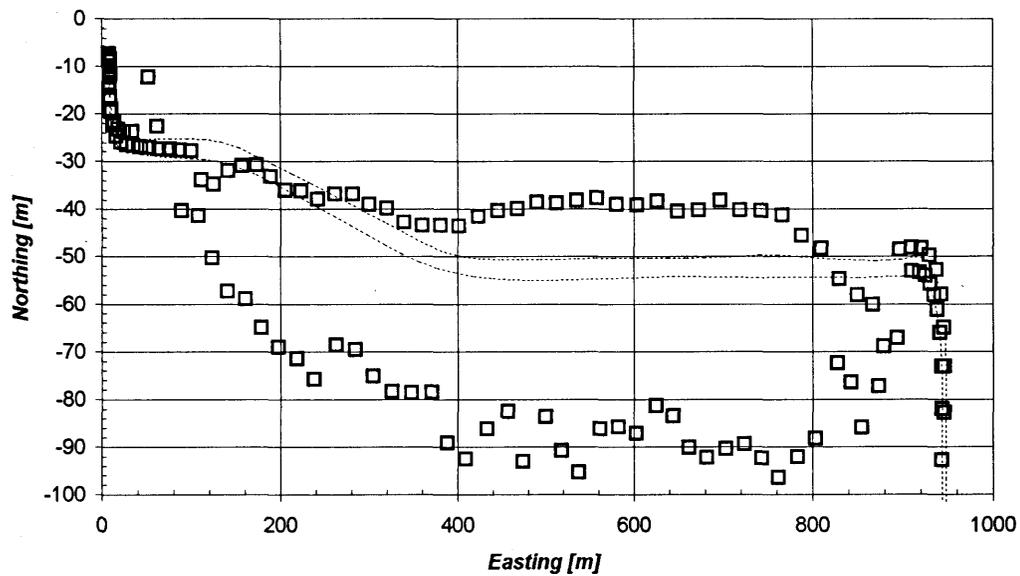
Figure 7.44. 2D Position, Section A, Springbank, June 29, 1996.
(60° Cross-Track Cutoff Angle, Height Constraint Least Squares)
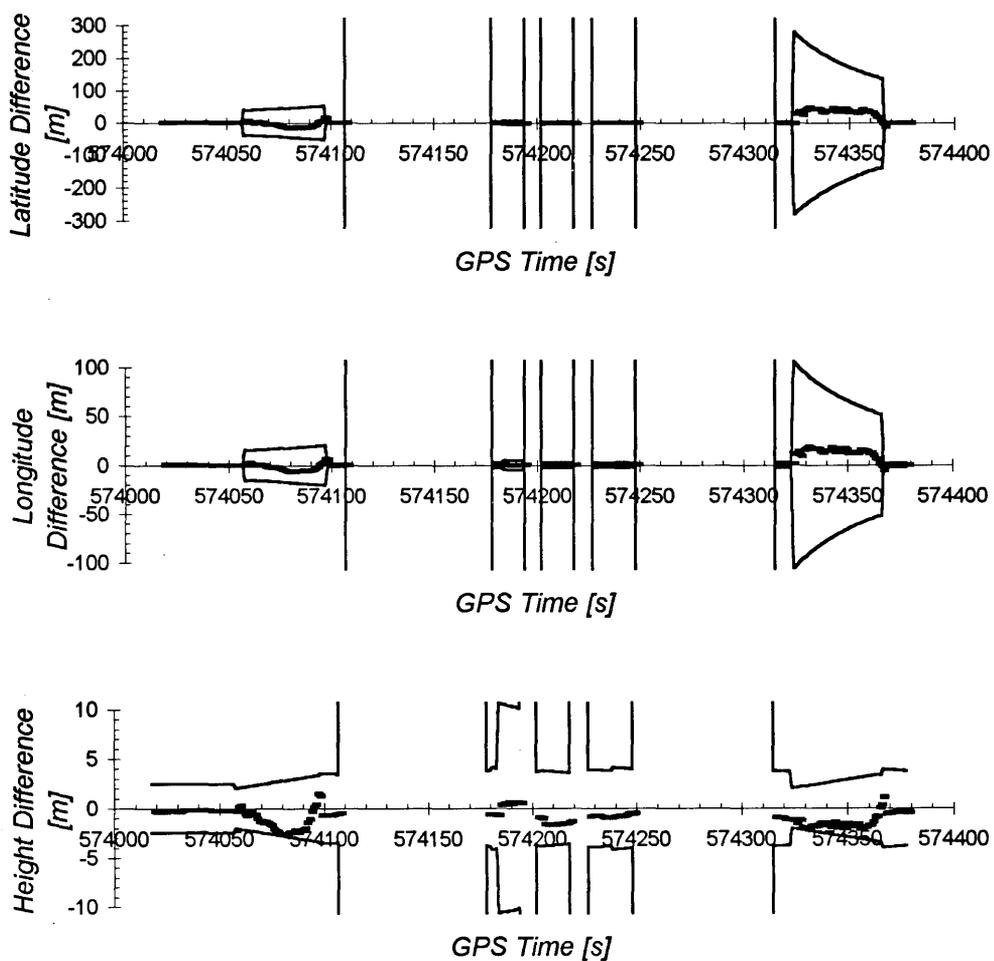
**Figure 7.45. Height Constraint Least Squares Position Errors,
Springbank, June 29, 1996.
(60° Cross-Track Cutoff Angle)**

Height and heading constraint positioning could not provide position estimates in Section B. Heading constraint requires a previous position to compute $d\phi$ and $d\lambda$. The previous position is treated as a constant, and the heading is evaluated from this point. If the vehicle turns during an outage period, as shown in Figure 7.46, the sensor heading may give a false constraint to the current position estimate. Therefore, the algorithm must include logic which shuts down the heading constraint if the previous position is missed. This logic is implemented to avoid a false heading constraint after an outage period. One may notice from Figure 7.37 that the number of visible satellites drops to one at some locations. The heading constraint is then shut down and is not used until good GPS coverage is obtained.

The position propagation using the last vehicle velocity and gyro heading during the outage period was examined but was not accurate enough to meet the requirement.
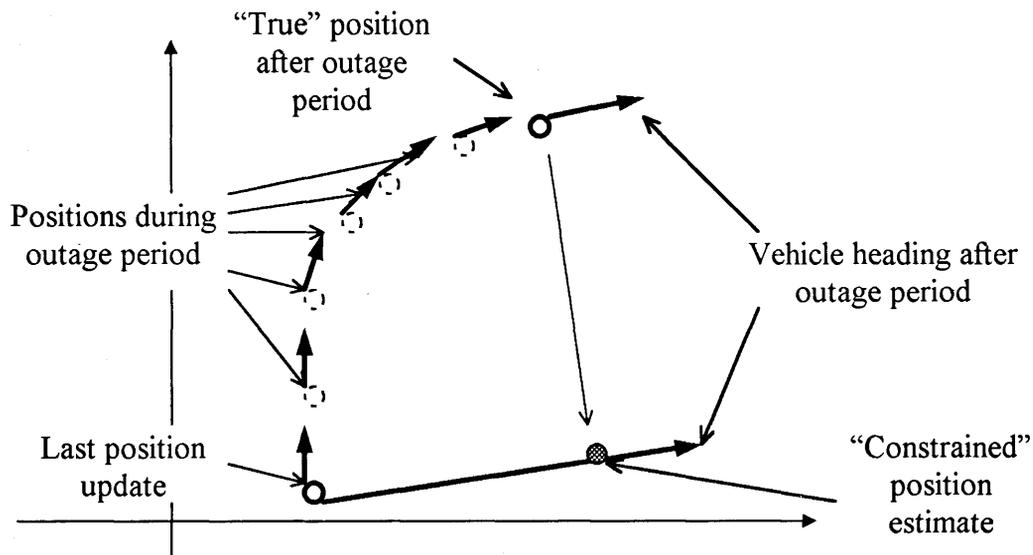
Figure 7.46. False Heading Constraint

This is due to the vehicle accelerations and decelerations for a relatively short period in urban areas.

DOPs of height and heading constraint least squares and Kalman filtering are shown in Figure 7.47. GDOP and NDOP are reduced to approximately 10 during the constraint period. Figures 7.48 and 7.49 are 2D position plots of height and heading constraint least squares solutions. There are outage periods in Section B. The differences between the reference trajectory and the height and heading constraint least squares solutions with 2σ error envelopes are shown in Figure 7.50. The standard deviations of latitude and longitude are 2.21 and 0.83 metres and the maximum errors are 5.83 and 2.51 metres, respectively, as shown in Table 7.19. The DRMS is approximately 2.9 metres. Position availability is 58.2% of time or 207 out of 356 epochs.
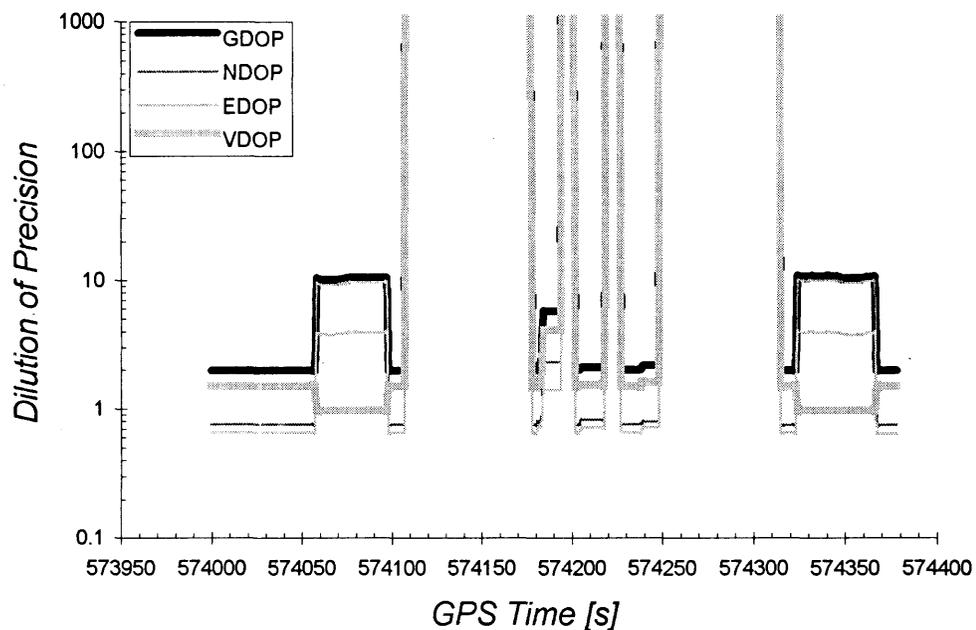
Figure 7.47. DOPs, Springbank, June 29, 1996.
(60° Cross-Track Cutoff Angle,
Height and Heading Constraint Least Squares and Kalman Filter)
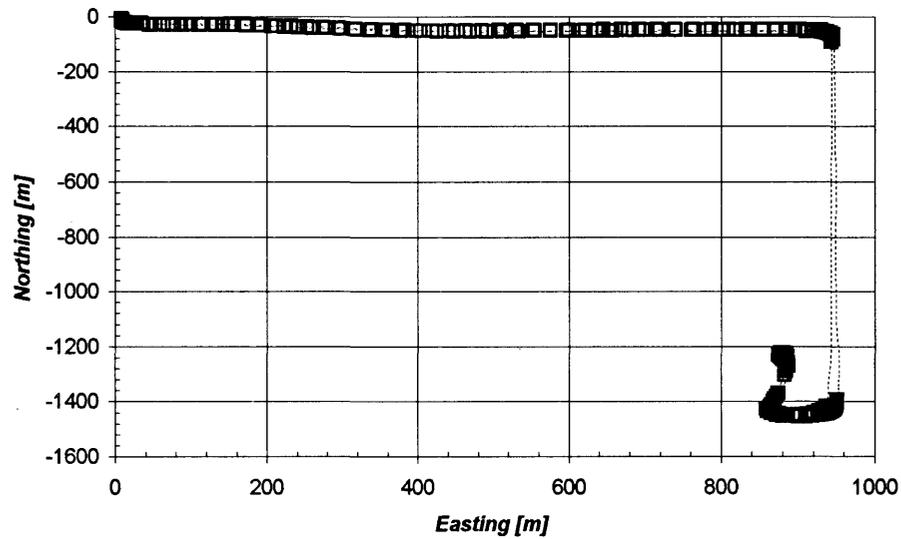
Figure 7.48. 2D Position, Springbank, June 29, 1996.
(60° Cross-Track Cutoff Angle, Height and Heading Constraint Least Squares)
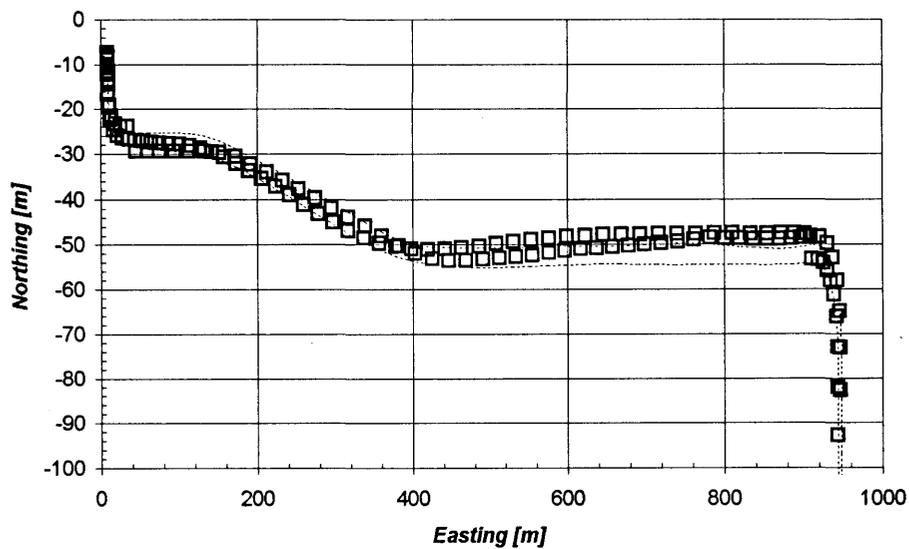

Figure 7.49. 2D Position, Section A, Springbank, June 29, 1996.
(60° Cross-Track Cutoff Angle, Height and Heading Constraint Least Squares)
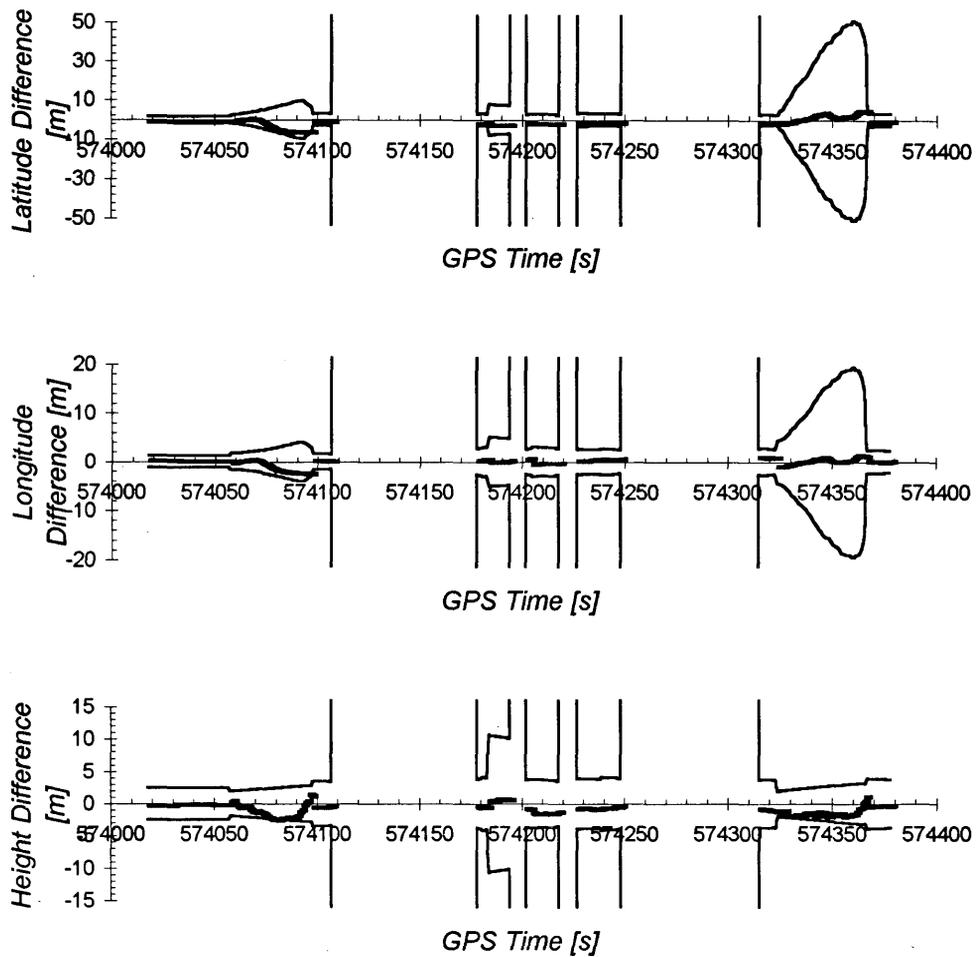
Figure 7.50. Height and Heading Constraint Least Squares Position Errors, Springbank, June 29, 1996. (60° Cross-Track Cutoff Angle)

Table 7.19. Position Estimate Difference Between Reference Trajectory and Height and Heading Constraint Least Squares Solutions, Springbank, June 29, 1996.
(60° Cross-Track Cutoff Angle)

	Latitude	Longitude	Height
Mean [m]	-1.62	-0.22	-0.93
Standard Deviation [m]	2.21	0.83	0.81
Max. Difference [m]	5.83	2.51	2.23
Min. Difference [m]	0.00	0.01	0.00
Position Availability	58.2 % / 207 epochs		

Figures 7.51 and 7.52 are 2D position plots of height and heading constraint Kalman filter solutions. As seen in Table 7.20, the standard deviations of latitude and longitude are 1.85 and 0.82 metres and the maximum errors are 6.75 and 2.82 metres, respectively. The DRMS is approximately 2.7 metres. Figure 7.53 shows the differences between the reference trajectory and the height and heading constraint Kalman filter solutions with 2σ error envelopes. Position displacements are mostly within the envelopes. In general, the solutions at a 60° cross-track cutoff angle are similar to those at a 45° cross-track cutoff angle but the availability is significantly reduced. Position availability is the same as that of height and heading constraint least squares solutions, 58.2% or 207 out of 356 epochs. A summary of position availability is given in Table 7.21.
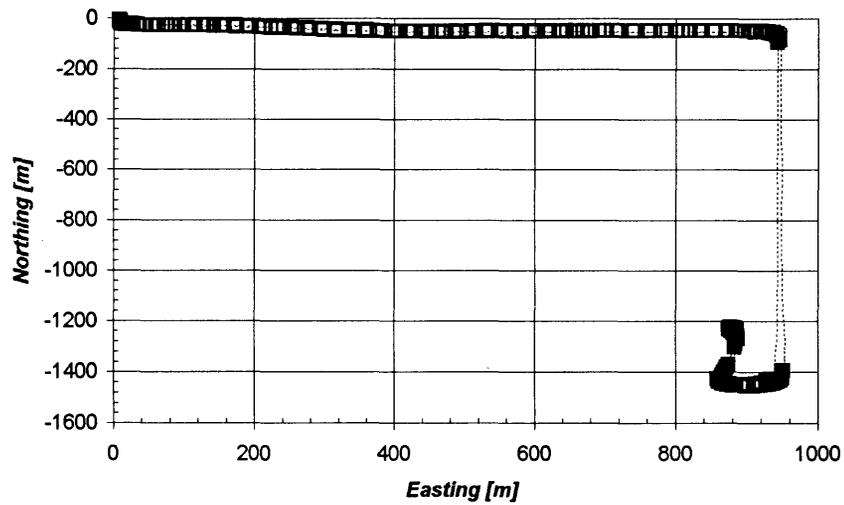
Figure 7.51. 2D Position, Springbank, June 29, 1996.
(60° Cross-Track Cutoff Angle, Height and Heading Constraint Kalman Filter)
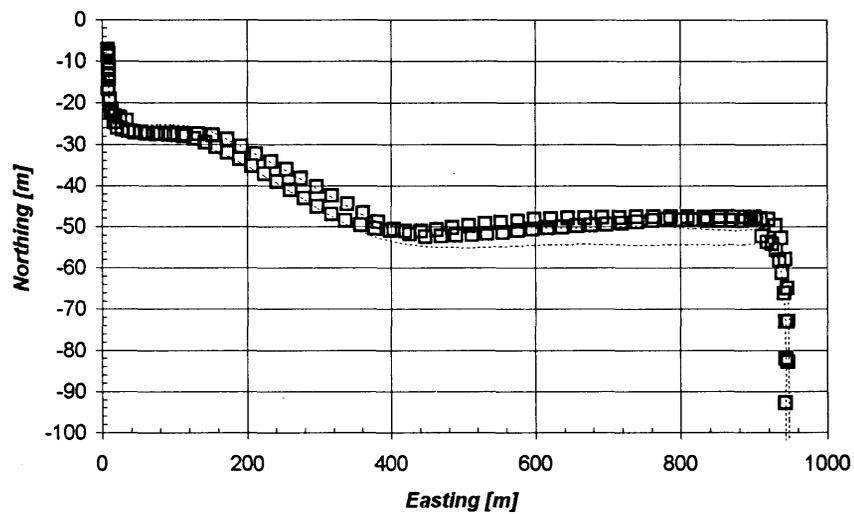
Figure 7.52. 2D Position, Section A, Springbank, June 29, 1996.
**(60° Cross-Track Cutoff Angle, Height and Heading Constraint Kalman Filter)**
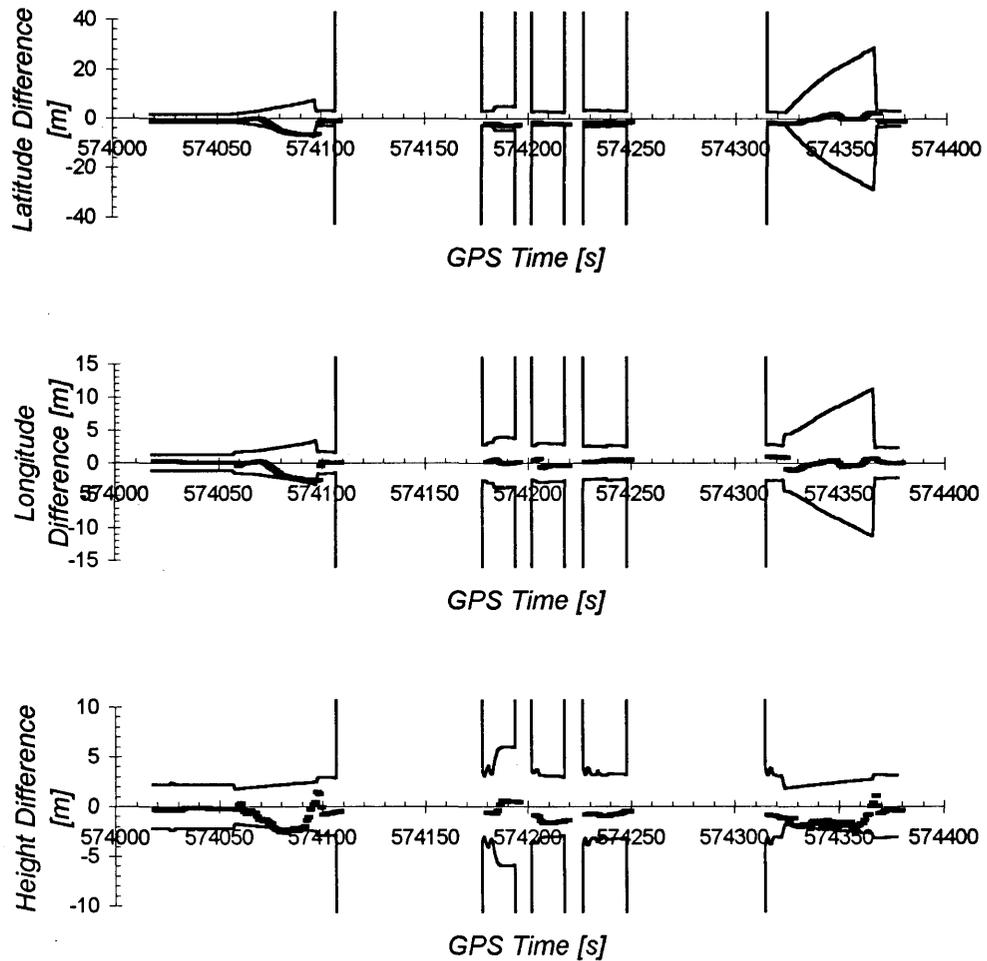
Figure 7.53. Height and Heading Constraint Kalman Filter Position Errors, Springbank, June 29, 1996. (60° Cross-Track Cutoff Angle)

Table 7.20. Position Estimate Difference Between Reference Trajectory and Height and Heading Constraint Kalman Filter Solutions, Springbank, June 29, 1996. (60° Cross-Track Cutoff Angle)

	Latitude	Longitude	Height
Mean [m]	-1.83	-0.30	-0.94
Standard Deviation [m]	1.85	0.82	0.81
Max. Difference [m]	6.75	2.82	2.67
Min. Difference [m]	0.07	0.00	0.01
Position Availability	58.2 % / 207 epochs		

Table 7.21. Position Estimate Availability, Springbank, June 29, 1996. (60° Cross-Track Cutoff Angle)

Estimation Mode	Position Estimate Availability	DRMS
Unaided Least Squares	124 epochs / 34.8%	2.0m
Height Constraint Least Squares	207 epochs / 58.2%	17.5m
Sensor Constraint Least Squares	207 epochs / 58.2%	2.9m
Sensor Constraint Kalman	207 epochs / 58.2%	2.7m

7.2 Downtown Calgary Field Test

7.2.1 Objectives and Strategies

The objective of the downtown testing is to observe system behavior in an actual and signal masking environment. Major weaknesses of the system are that it requires a minimum of two satellites in an appropriate geometry for computation and a previous position is always required for the heading constraint. Since Calgary has a skywalk network called +15, there are occasions when all satellite signals are temporarily blocked by a skywalk. Although the ideal solution would be to integrate a DR positioning device in the absence of GPS, it was not allowed for this project since portability was a primary requirement. Instead, the algorithm was modified to compensate for this weakness. This revised logic is based on an assumption that the vehicle does not turn during an outage period. Although this assumption initially sounds unreasonable, we can expect better GPS coverage at intersections and intersections are mostly connected by straight roads in downtown Calgary. By making such an assumption, we can still activate the heading constraint with a position estimate before the outage period and provide more positioning solutions. Note that this kind of assumption should only be made for relatively short periods since the program may become unstable and solutions may diverge. This testing is only intended to show the potential of the system in a harsh environment.

Bullock (1995) examined the GPS signal availability in downtown Calgary and the position availability was between 58 % and 83 % (Bullock 1995). Thus, the GPS signal availability in downtown Calgary varies depending on the route selected, time of

operation, etc. The range error detection logic is critical to the sensor constraint navigation system since it relies on "good" GPS update to calibrate and initialize the sensor measurements. Two detection routines are implemented in the system. First, the solution without constraints is computed each time and the range residuals are compared to a predetermined threshold value. The residual threshold is optimized for best results. Second, the horizontal and vertical accelerations are monitored and a warning is given if the acceleration exceeds an expected number determined from the vehicle dynamics. These threshold values are given in the following sections.

7.2.2 Route Description

The field test was conducted in downtown Calgary on August 17, 1996. The test route is shown in Figure 7.54. The system was mounted in a 1996 Pontiac Sunfire. The reference station was located on the roof of the Engineering Complex building at The University of Calgary. Data was collected every second. The distance between the reference station and the rover vehicle ranged between 4 and 7 km. The location is far from ideal for GPS positioning since there are numerous multi-storey buildings, +15 skywalks, reflective glass surfaces and heavy traffic. There were also several occasions when the test vehicle was surrounded by large busses and trucks, blocking additional satellite signals.

There is a railroad between 9th and 10th avenues and the satellite visibility is fairly good on 9th avenue. However, 10-storey or higher hotels and buildings along 9th avenue could be major multipath sources. Such is the case around 3rd avenue and 5th street as
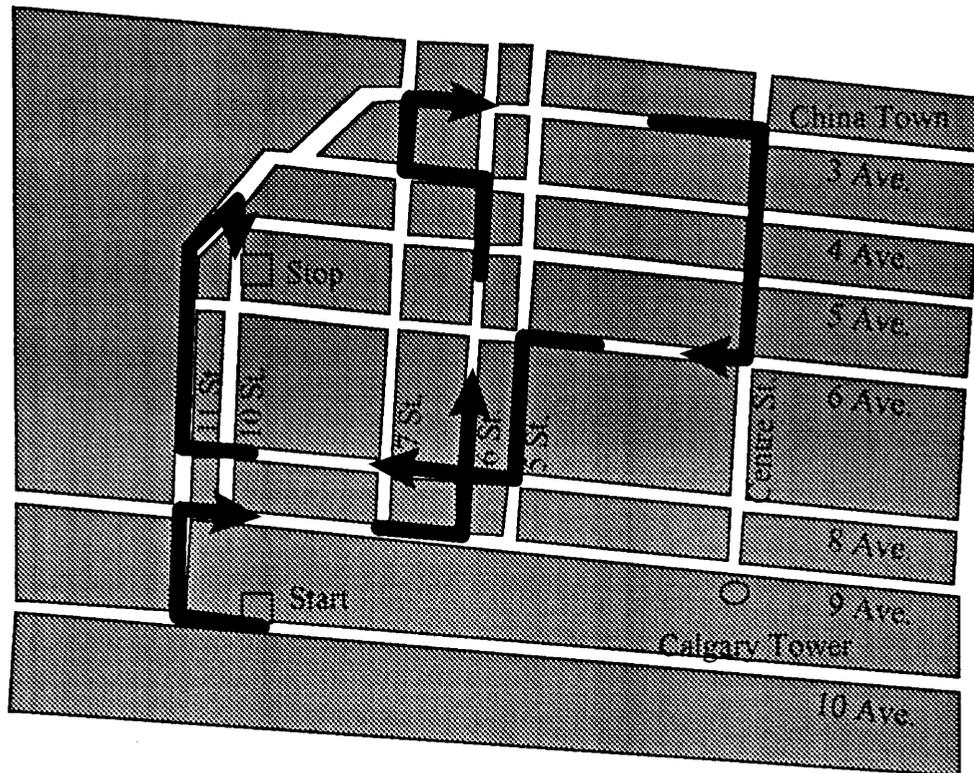
Figure 7.54. Test Route, Downtown Calgary, August 17, 1996

well. The buildings there use mirrored windows to reflect sunlight. These windows also reflect GPS signals quite efficiently. 4th and 8th avenues are in the downtown core where satellite visibility is extremely poor. Road width ranges from approximately 10 to 15 metres. Most roads have four lanes.

The satellite visibility plot is given in Figure 7.55. The number of visible satellites changes rapidly because of the dynamic environment and temporary satellite blockage. One may notice from Figure 7.55 that there are two sections when the number of satellites is always less than four. There is also a number of instances when only one signal is
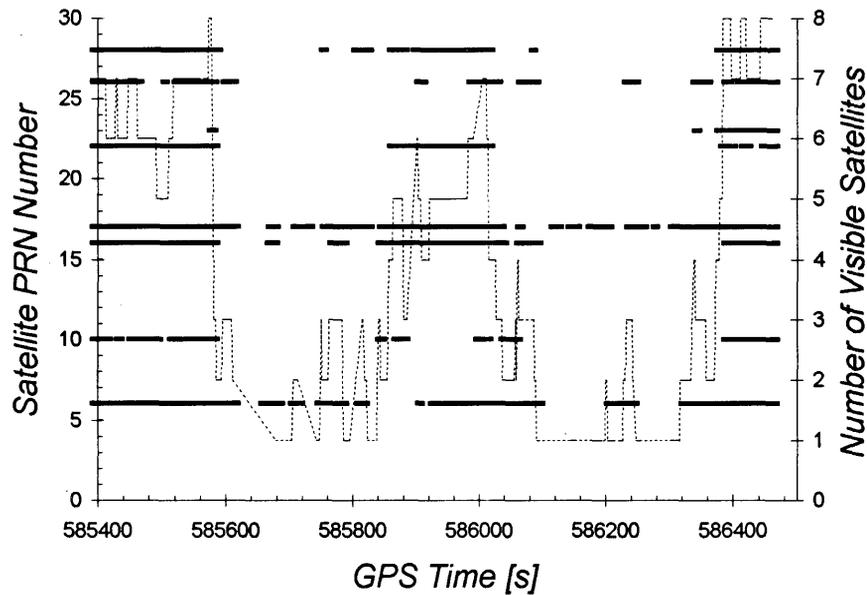
Figure 7.55. Visible Satellites, Downtown Calgary, August 17, 1996

available. Therefore, it is unlikely that one would receive continuous solutions from the sensor constraint GPS navigation system, which requires two signals for computation.

7.2.3 Test Results

7.2.3.1 Unaided GPS Results

Figure 7.56 shows DOPs for the unaided least squares solutions. The GDOP ranges between 15 and 30 when available. For reference, the 2D positions are plotted on the route map as shown in Figure 7.57. Note that this route map is neither accurate nor precise. The route map is used here to measure the consistency of the positioning solutions. One may conclude from Figure 7.57 that unaided GPS positioning is simply not

sufficient for urban land navigation applications. Solutions are obtained only on the edge

of downtown. This result agrees with the satellite visibility plot, Figure 7.55, in which

there are two long GPS signal outage periods. The first outage period starts near 9th

avenue and 7th street and ends at 3rd avenue. The second one starts at 3rd avenue and

centre street and ends at 11th street. Position availability is 35.1% or 351 out of 1001

epochs.
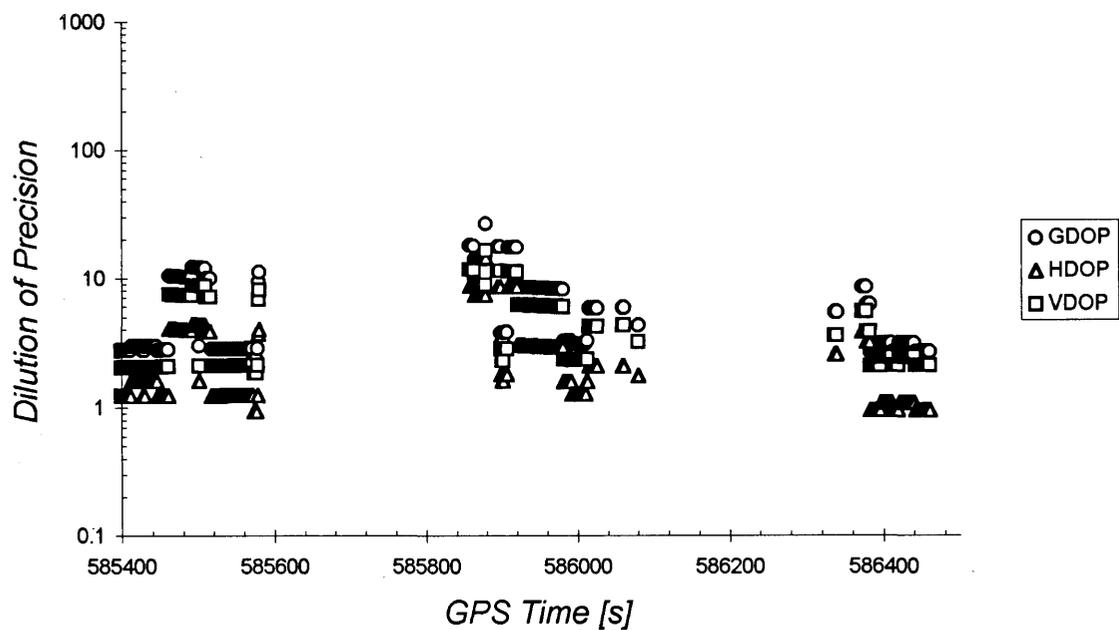
Figure 7.56. DOPs, Downtown Calgary, August 17, 1996.
(Unaided Least Squares)

Figure 7.57. 2D Position, Downtown Calgary, August 17, 1996.
(Unaided Least Squares)

7.2.3.2 Height and Heading Constraint GPS Results

The DOPs for height and heading constraint positioning are shown in Figure 7.58. Compared to the DOP plot of unaided least squares, Figure 7.56, an improvement is immediately seen. The DOPs for the least squares and Kalman filter are identical since they share the same algorithm and data set. When the height constraint is applied, the VDOP is always approximately 1.0. The satellite geometry is sufficiently enhanced in that we do not see any DOP outliers in Figure 7.58.

Figure 7.58. DOPs, Downtown Calgary, August 17, 1996.
(Height and Heading Constraint Least Squares and Kalman Filter)

The least squares positioning mode is first examined. Threshold values used for computation are summarized in Table 7.22. The horizontal acceleration is taken from the maximum acceleration of 0-60 mph of the test vehicle, a Pontiac Sunfire. Since the test vehicle was driven gently, the acceleration should not exceed the threshold without GPS range errors. The vertical acceleration is less than the horizontal considering the vehicle's dynamics. The NovAtel GPSCard™ gives good range measurements and the range threshold used is therefore very tight. The threshold of 1.5 metres, which provided the best result, is respectable considering a noisy range measurement, frequent satellite constellation changes and the harsh multipath environment. If the threshold is larger than this number, it is more likely that the algorithm will introduce range errors into the

solution. If it is smaller, the algorithm will keep activating sensor constraints without adequate initializations and calibrations. For the best performance, both extremes should be avoided.

Table 7.22. GPS Range Error Detection Thresholds, Downtown Calgary, August 17, 1996. (Height and Heading Constraint Least Squares)

Target	Threshold
Horizontal Acceleration	4 m/s^2
Vertical Acceleration	1.5 m/s^2
Range Residual	1.5 m
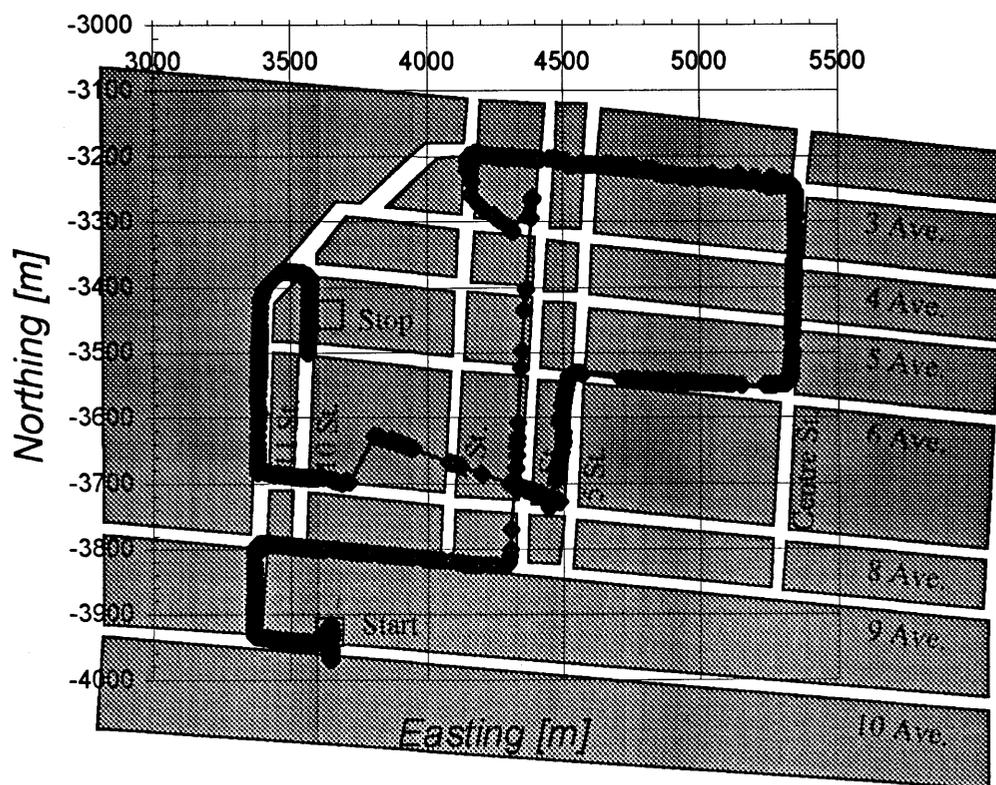
Figure 7.59. 2D Position, Downtown Calgary, August 17, 1996. (Height and Heading Constraint Least Squares)

Figure 7.59 shows the effect of height and heading constraint. We have a good number of positioning solutions throughout the session. It is expected that we would not obtain continuous solutions because of the limitation of two-satellite positioning. Indeed, solutions in the downtown are not continuous. There are numerous blanks between estimates. Due to the revised algorithm, we are still able to maintain the heading constraint after an outage period. Position availability is 69.4% or 695 out of 1001 epochs. There is one section on 8th avenue where heading constraint provides false information. This is likely due to heading initialization with a GPS solution which contains an undetectable multipath magnitude. The implemented error detection routine was not sufficient enough to find all range errors. The range residuals may not be suitable for the error threshold since there are not redundant solutions in urban environments due to fewer observations. Another multipath error detection strategy may be desirable for the superior performance.

The Kalman filter positioning mode is then employed. This 8-state Kalman position filter uses GPS range measurements and sensor measurements for update. An advantage of the Kalman filter is that it gives a smooth trajectory. This property greatly helps when the satellite constellation changes. However, a Kalman filter solution contains a response delay due to the filtering process. The range residual threshold must be increased, otherwise the algorithm would keep activating the sensor constraint without proper initialization. The threshold number of 3 metres gave the best performance for this particular data set with the Kalman filter. This compromise will increase the possibility that undetectable multipath may degrade the position accuracy. Threshold values are summarized in Table 7.23.

**Table 7.23. GPS Range Error Detection Thresholds,
Downtown Calgary, August 17, 1996.
(Height and Heading Constraint Kalman Filter)**

Target	Threshold
Horizontal Acceleration	4 m/s^2
Vertical Acceleration	1.5 m/s^2
Range Residual	3.0 m

**Figure 7.60. 2D Position, Downtown Calgary, August 17, 1996.
(Height and Heading Constraint Kalman Filter)**

Figure 7.60 shows the 2D position plot of height and heading constraint Kalman filter solutions. The result is not as good as Figure 7.59 due to a less stringent range residual threshold and thus inferior error control. The Kalman filter tends to break down when a false constraint is introduced (i.e. when the initialization and calibration is not done properly). Note that this filter already has a huge horizontal spectral density of 400 m^2/s^3 plus adaptive logic which only increases this number. The filter would break down if a larger spectral density is used. As expected, the multipath-induced heading error is larger than that of least squares on 8th avenue. In addition, the solutions on 3rd, 6th and 9th avenues are not as consistent as those in Figure 7.59. Another multipath detection logic, which does not rely on the range residuals, would be necessary to improve the accuracy of the Kalman filter solutions. The Kalman filter produces slightly more position solutions than the least squares does, 70.4% or 705 out of 1001 epochs. This may be due to the lack of divergence state in the Kalman filter as discussed in the simulation section. Position availability is summarized in Table 7.24.

Table 7.24. Position Estimate Availability, Downtown Calgary, August 17, 1996

Positioning Mode	Position Availability (total 1001 epochs)
Unaided Least Squares	351 epochs / 35.1%
Height and Heading Constraint Least Squares	695 epochs / 69.4%
Height and Heading Constraint Kalman Filter	705 epochs / 70.4%

Figure 7.61 gives a vertical view of the position solutions. The unaided least squares solutions apparently contain errors. These errors may be due to multipath. Although the height and heading constraint least squares solutions are much more consistent, they also have spike-like errors. These spikes may be caused by in-vehicle pressure disturbances, which occur during acceleration and deceleration. This effect is inevitable since a vehicle repeats the stop-and-go maneuver in an urban area. Height and heading constraint Kalman filter solutions are less consistent than those of least squares because of the inferior error detection threshold.
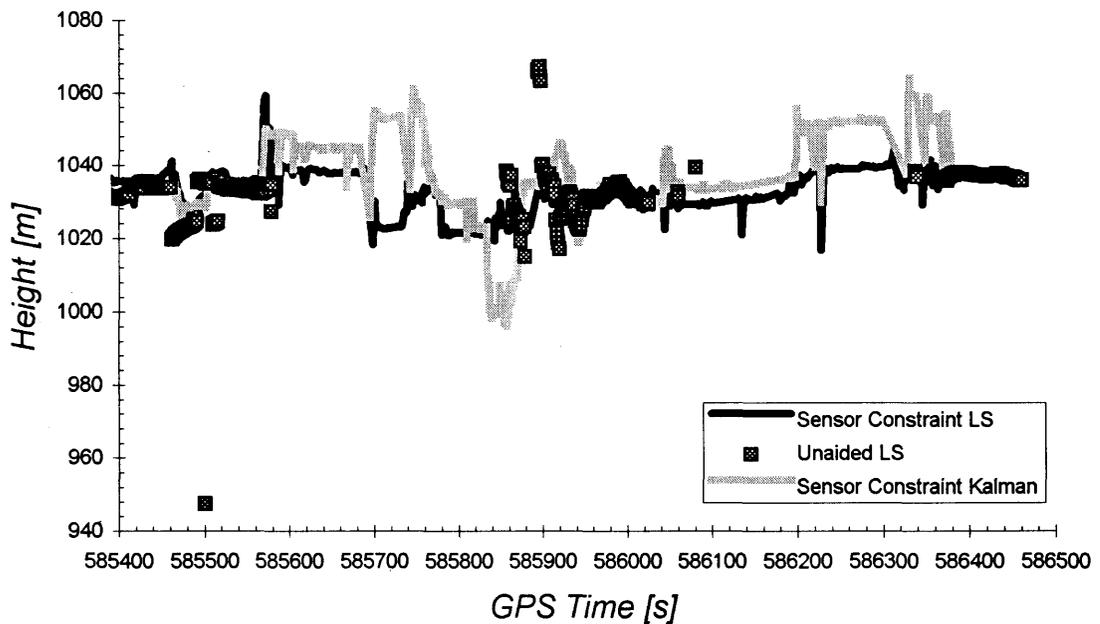
Figure 7.61. Vertical Position, Downtown Calgary, August 17, 1996

CHAPTER EIGHT

CONCLUSIONS AND RECOMMENDATIONS

8.1 Conclusions

The height and heading constraint navigation system developed herein significantly improves the possibility of GPS navigation in urban environments. For the cases tested, it improves the positioning availability by 24 to 35% while mostly maintaining the positioning accuracy within 10 metres DRMS. The barometer and gyro information enhance the satellite geometry. In the process, they can also constrain the vertical and horizontal positioning estimates to minimize the error caused by poor GPS signal quality. Since the accuracy of the sensor constraint solution degrades with time, the system requires periodical sensor data initialization and calibration with good GPS data for the best results.

The urban canyon simulations using the virtual wall concept are examined to evaluate the performance of the height and heading constraint navigation system. The virtual wall concept is proven to be useful to simulate the urban environment. The concept successfully creates the weak satellite geometry which is often seen in the urban areas (Hayashi 1996). The full availability of GPS signals provides a precise reference trajectory which is used to assess the accuracy of the constrained solutions. It is shown that the sensor measurements improve the DOPs significantly. The height constraint navigation method alone may not be suitable for urban land navigation. This technique enables a three-satellite positioning, however, three satellites form poor horizontal satellite geometry

more likely and it degrades position accuracy. The poor horizontal geometry is caused by obstructions which mask satellite signals on each side of the vehicle. The heading constraint introduces an additional horizontal constraint to the solution. This enhances the horizontal geometrical strength. For these simulations, height and heading constraint navigation improves position availability by 26% for a cross-track cutoff angle of 45 degrees and 24% for 60 degrees. In this test, errors induced by employing height and heading constraints do not degrade accuracy beyond the 10 metres DRMS which is the requirement for this project.

The least squares solutions become discontinuous when the satellite constellation changes as well as during transitions between the sensor constraint and the unaided solutions. The Kalman filter solutions are smooth and more consistent due to the filtering process. The overall performance of least squares and the Kalman filter are comparable. However, the error detection logic used herein for Kalman filter could not detect the range error as effectively as that for least squares. This was caused by larger range residuals of Kalman filter which forced to use a larger error detection threshold. As a consequence, the Kalman filter solutions seem more affected by range errors than the least squares solutions.

Actual downtown testing revealed some limitations. The position availability of the unaided least squares is 35.1% of time in this test, which may be worse than the position availability in downtown Calgary conducted by others (Bullock 1995). This poor result may be caused by the harsh test route environment. This is far from sufficient for urban navigation applications. The position availability is improved to approximately 70% of

time with height and heading constraints. Stringent GPS range error detection logic is needed since GPS signals may be contaminated by multipath. The error detection logic implemented is not sufficient. Thus, there are still some undetectable GPS range errors which give a false initial heading determination. The height and heading constraint positioning solutions are consistent but including vertical position "spikes". They are likely due to in-vehicle pressure disturbances.

The Kalman filter solution has a delay because of the filtering process. The delay appears as a larger GPS range residual. This forces the error detection logic to be less stringent than that of least squares in order to adequately calibrate the sensor information. Consequently, the Kalman filter positioning solutions are not as good as those of least squares. However, they still track the test route fairly well, considering the extremely poor GPS signal reception and harsh multipath environment in downtown.

8.2 Recommendations

Some weaknesses of the system have been pointed out. Probably, the biggest is that the system requires a minimum of two visible satellites to update the solution. This is a major drawback since all satellites are frequently blocked in downtown Calgary by the +15 skywalk network. Ideally, continuous positioning is desirable for the heading constraint which utilizes a previous position as a starting point. The revised algorithm, which is based on the assumption that intersections are connected by straight roads, would not work well in a city where intersections are connected by curves. The author strongly recommends that the system be combined with a distance sensor such as an odometer or

accelerometer. The distance sensor can be incorporated into the constraint algorithm as a distance constraint or used to complete DR positioning with a gyro. Another possibility is to use an on-board precise clock. If the clock is stable enough, the receiver clock offset may be estimated for a certain period. This will enable one-satellite positioning.

Another weakness of the system is that it requires periodical sensor data initialization and calibration. This should be performed with healthy GPS solutions. However, the determination of the quality of GPS solutions is extremely difficult in a less-than-perfect environment since there is far less redundancy. The error detection logic implemented, which relies on the range residual, DOP and vehicle dynamics, may not be sufficient. There are still undetected range errors causing sensor initialization and calibration errors. Another error detection strategy, which detects range errors more effectively, is highly recommended.

The concept of sensor constraint may be utilized in numerous applications and its algorithm is quite simple. However, one should give great attention to the sensor characteristics. The accuracy of sensor constraint positioning is directly proportional to the accuracy of the sensors. Therefore, quality monitoring and control of sensor data may be required. The sensors used in this project have been tested in a controlled environment (factory laboratory) before shipment. The specifications of the sensors are given by the manufacturer. Other tests are needed on-site to determine the short and long term stability, relation between the unit temperature and output, etc. Some of these properties may change as the unit ages. It is therefore highly recommended that these properties be routinely checked to ensure optimal performance.

This system has been developed using NovAtel GPSCard^{TM} receivers but the algorithm itself is totally independent of the GPS receiver used. Although the data logging program is tightly integrated with NovAtel commands, adaptation to any other receiver would not be difficult. The navigation program is designed to accept any C^{3}NAV^{TM}/FLYKIN^{TM} format GPS raw data, barometer and gyro files. The adjustment may be done by changing filtering parameters and error detection thresholds.

REFERENCES

Abbott, E. and D. Powell (1995). "An Examination of the Relative Merits of Various Sensors for Vehicle Navigation," Proceedings of ION GPS-95 (Palm Springs, California, September 12-15, 1995), The Institute of Navigation, Alexandria, VA, pp. 1269-1284.

Abousalem, M. A. (1993). Development of a Robust GPS Kinematic Positioning Module for Automatic Vehicle Location and Navigation Systems, UCGE Reports Number 20077, The University of Calgary, Calgary, Canada.

Allen, D., S. M. Bennett, J. Brunner and R. B. Dyott (1994). "A Low Cost Fiber Optic Gyro for Land Navigation," SPIE Vol. 2292 Fiber Optic and Laser Sensors XII, 25-27 July 1994, San Diego, California, pp.203-217.

Andrew Corporation (1994). AUTOGYRO™ Installation Manual, Document No. 237318, Rev. A, P/N 224894, St. Petersburg, FL.

Bennett, S. and S. R. Enge (1994). "Fiber Optic Rate Gyro for Land Navigation and Platform Stabilization," Sensors Expo '94, Cleveland, OH.

Bullock, J. B. (1995). A Prototype Portable Vehicle Navigation System Utilizing Map Aided GPS, UCGE Reports Number 20081, Department of Geomatics Engineering, The University of Calgary, Calgary, Canada.

Braasch, M. S. (1996). GPS and DGPS Multipath Effects and Modeling, Lecture Note of the ION GPS-96 Tutorial Course 455 (Kansas City, MO, September 16, 1996), Navtech Seminars Inc., Arlington, VA.

Brown, A. (1992). "A Low Cost Vehicle Location and Tracking System," IEEE PLANS '92, pp.516-523.

Brown, R. G. and P. Y. C. Hwang (1992). Introduction to Random Signals And Applied Kalman Filtering, Second Edition, John Wiley & Sons Inc., New York.

Cannon, M. E. (1991). Airborne GPS/INS with an Application to Aerotriangulation, Ph.D. Dissertation, Department of Geomatics Engineering, The University of Calgary, Calgary, Canada.

Cannon, M. E. and G. Lachapelle (1992). "Analysis of a High Performance C/A Code GPS Receiver in Kinematic Mode," Navigation, Vol. 39, No. 3, The Institute of Navigation, Alexandria, VA, pp. 285-299.

Carlson, N. A. (1987). "Federated Square Root Filter For Decentralized Parallel Processing," Proceedings of The National Aerospace Electronics Conference, Naecon, Ohio.

Chadwick, D. J. (1994). "Projected Navigation System Requirements for Intelligent Vehicle Highway System (IVHS)," Proceedings of ION GPS-94 (Salt Lake City, 21-23 September 1994), The Institute of Navigation, Alexandria, VA.

Copley, D. W. (1994). The Application of Vibrating Cylinder Pressure Transducers to Non-Military Applications, Weston Aerospace Limited, Farnborough, Hampshire, UK.

Da, R. and G. Dedes (1995). "Nonlinear Smoothing of Dead Reckoning Data With GPS Measurements," Proceedings of ION GPS-95 (Palm Springs, California, September 12-15, 1995), The Institute of Navigation, Alexandria, VA, pp. 1285-1294.

Gao, Y. (1992). A Robust Quality Control System For GPS Navigation and Kinematic Positioning, Master's Thesis, Department of Geomatics Engineering, The University of Calgary, Calgary, Canada.

Geier, G. J., A. Heshmati, P. McLain, K. Johnson and M. Murphy (1993). "Integration of GPS with Dead Reckoning for Vehicle Tracking Applications," Proceedings of the 49th Annual Meeting, June 21-23, The Institute of Navigation, Alexandria, VA, pp. 75-81.

Gelb, A., J. F. Kasper Jr., R. A. Nash, C. F. Price and A. A. Sutherland Jr. (1974). Applied Optimal Estimation, The M.I.T. Press, Massachusetts.

Harris, C. B. (1989). "Prototype For a Land Based Automatic Vehicle Location and Navigation System," UCSE Reports Number 20033, Department of Geomatics Engineering, The University of Calgary, Calgary, Canada.

Hayashi, N. (1996). "Low-Cost Sensor Constraint GPS Land Navigation System in an Urban Environment," Proceedings of ION GPS-96 (Kansas City, MO, September 17-20, 1996), The Institute of Navigation, Alexandria, VA.

Ishikawa, S., H. Maeda, A. Shibata and F. Morisue (1995). "Hybrid GPS for Land Vehicle," Proceedings of ION GPS-95 (Palm Springs, California, September 12-15, 1995), The Institute of Navigation, Alexandria, VA, pp. 1301-1306.

Kao, W. W. (1991). "Integration of GPS and Dead-Reckoning Navigation Systems," In Vehicle Navigation Systems (VNIS) Conference, October 20-23, Dearborn, Michigan, pp. 635-643.

KVH (1994). The C100 Compass Engine, Technical Specifications, KVH Industries, Inc., Middletown, RI.

Krakiwsky, E. J. (1990). The Method of Least Squares: A Synthesis of Advances, UCGE Reports Number 10003, The University of Calgary, Calgary, Canada.

Lachapelle, G. (1995). ENGO 625 GPS Theory and Applications, Lecture Note, Department of Geomatics Engineering, The University of Calgary, Calgary, Canada.

Lachapelle, G., M. E. Cannon, C. Tang, H. Lan, S. Wee, S. Ryan and F. Forbes (1996). "Shipborne and Airborne DGPS Positioning Using Various Receiver Technologies and RTCM Message Types 1/9 and 18-21," *Canadian Aeronautics and Space Journal*, Vol. 42, No. 1, March 1996, pp.37-44.

Lachapelle, G., J. Henriksen and T. Melgård (1994). "Seasonal Effect of Tree Foliage on GPS Signal Availability and Accuracy for Vehicular Navigation," Proceedings of ION GPS-94 (Salt Lake City, 21-23 September 1994), The Institute of Navigation, Alexandria, VA.

Lawrence, A. (1993). Modern Inertial Technology - Navigation, Guidance, and Control, Springer-Verlag New York, Inc.

Liu, R. Y. and G. W. Adams (1990). "Interferometric Fiber-Optic Gyroscopes: A Summary of Progress," IEEE Position, Location and Navigation Symposium (PLANS 1990), 1990.

Lutgens, F. K. and E. J. Tarbuck (1982). The Atmosphere – An Introduction to Meteorology, Second Edition, Prentice-Hall Inc., Englewood Cliffs, NJ.

Martin, E. H. (1980). "GPS User Equipment Error Models," *Special Issue of Navigation on the Global Positioning System*, Volume 1, The Institute of Navigation, Alexandria, VA.

Martinelli, V. and R. Ikeda (1995). "Next Generation Fiber Optic Gyroscopes for Use with GPS in Vehicle Navigation and Location Systems," Proceedings of ION GPS-95 (Palm Springs, California, September 12-15, 1995), The Institute of Navigation, Alexandria, VA.

Nakamura, T. (1990). "Vibration Gyroscope Employs Piezoelectric Vibrator," Journal of Electrical Engineering, Hi-Tech Report, September, pp. 99-104.

Navtech Seminars, Inc. (1996). Basic Glossary of GPS Terms, 2775 S. Quincy Street, Suite 610, Arlington, VA 22206-2204.

Perlmutter, M. (1993). "A Tactical Fiber Optic Gyro with All-Digital Signal Processing," Proceedings of the 49th Annual Meeting, June 21-23, The Institute of Navigation, Alexandria, VA, pp. 603-616.

Phillips, A. C. (1993). "Low Cost Dead Reckoning Sensors," Proceedings of the 1993 National Technical Meeting, The Institute of Navigation (San Francisco, CA, January 20-22), The Institute of Navigation, Alexandria, VA, pp. 145-149.

Sakata, R. (1996). What is VICS? -- Vehicle Information and Communication System, Nikkan-Kougyou Inc., Tokyo, Japan (in Japanese).

Spilker, J. J. Jr. (1980). "GPS Signal Structure and Performance Characteristics," *Global Navigation System – Papers Published in Navigation*, Volume 1, The Institute of Navigation, Alexandria, VA.

Sushko, M. S. K. (1993). "Dead Reckoning Navigation (DRN) Assistance for GPS Based AVL Systems," Proceedings of the 1993 National Technical Meeting of The Institute of Navigation, January, 1993, pp. 161-169.

Tang, C. (1996). Accuracy and Reliability of Various DGPS Approaches, UCGE Reports Number 20095, Department of Geomatics Engineering, The University of Calgary, Calgary, Canada.

US Department of Transportation and Defense (1990). Federal Radionavigation Plan, DOD-4650.4/DOT-VNTSC-RSPA-90-3, National Technical Information Service, Springfield, Virginia. Viatran Corporation (1995). X45/X46 Series Pressure Transducers Installation Data, Grand Island, NY.

Van Nee, R. and J. Siereveld (1994). "The Multipath Estimating Delay Lock Loop: Approaching Theoretical Accuracy Limits," PLANS '94, Las Vegas, April 1994.

Viatran Corporation (1996). Pressure Transducers – Model # 246 / 346 Electronic Barometer Information Sheet, Grand Island, NY.